DOCTORAL THESIS

Study on the Topological, Electrical and Optical Properties

and Carrier Dynamics of 2D Materials

Fujun Liu

Brasília, Março de 2023

UNIVERSIDADE DE BRASÍLIA

INSTITUTO DE FÍSICA

UNIVERSIDADE DE BRASILIA

INSTITUTO DE FÍSICA

DOCTORAL THESIS

Study on the Topological, Electrical and Optical Properties

and Carrier Dynamics of 2D Materials

Fujun Liu

Relatório submetido ao Instituto de Física

Elétrica como requisito parcial para obtenção

do grau de Doutor em Física

Banca Examinadora

Prof. Fanyao Qu, IF/UnB
Orientador

Prof. Alexandre Cavalheiro Dias, IF/UnB
presidente

Prof. Diego Rabelo, UFC
Examinador externo

Prof. Mariana Malard, FUP/UnB
Examinador interno

Dedicatória

Fujun Liu

RESUMO

Primeiro, propomos um método simples e geral para criar um semimetal robusto topológico de linha nodal, introduzindo vacâncias periódicas na rede. Normalmente as linhas nodais são suprimidas na presença de acoplamento spin-órbita, a menos que sejam protegidas por algumas simetrias topológicas. Transformamos um material bidimensional (2D) em uma rede com simetria não simórfica, removendo periodicamente átomos selecionados. Como estudo de caso, investigamos o borofeno (uma folha de boro semelhante a um favo de mel). O borofeno puro é empregado como referência. Enquanto os cones de Dirac do borofeno puro são separados por acoplamento spin-órbita e troca magnética, linhas nodais robustas emergem no espectro de energia do borofeno com simetria não simórfica. Propomos um modelo 2D eficaz e uma análise de simetria para demonstrar que essas linhas nodais são topológicas e protegidas por um plano de deslizamento não simórfico. Nossas descobertas oferecem uma mudança de paradigma para o projeto de semimetais de linha nodal: em vez de procurar por materiais não simórficos, semimetais robustos de linha nodal podem ser obtidos simplesmente removendo átomos de cristais simmórficos comuns.

Em seguida, estudamos o espectro excitônico do material 2D e os derivados da heteroestrutura. Nossa abordagem leva em consideração a triagem anômala em duas dimensões e a presença de um substrato magnético. A equação de Bethe-Salpeter é resolvida para uma descrição de ligação de partícula independente baseado num DFT cálculo. Obtemos as principais características do espectro óptico analisando a localização na zona de luz dos picos excitônicos. Estudamos o efeito de diferentes formas de empilhamento nas principais características ópticas de heteroestruturas, nomeadamente, as contribuições da interação entre camadas e a validade das polorizações. Comparamos a magnitude absoluta da condutividade óptica linear.

Finalmente, investigamos o espalhamento inter/intra vale de portadores em monocamadas de dicalcogenetos de metais de transição 2D. Uma análise detalhada do espalhamento inter-/intra vale elétron-fônon e exciton-fônon é descrita. O espalhamento de elétrons em bandas de condução é estudado por várias equipes, mas o espalhamento de lacunas em bandas de valência nunca foi relatado, devido à grande diferença de energia induzida pelo acoplamento spin-órbita. Para resolver este problema, estudamos a possibilidade de espalhamento por efeito de troca de excitons entre diferentes vales.

ABSTRACT

First, we propose an simple and general method to create robust topological nodal line semimetal, by introducing periodic vacancies into the lattice. Normally the nodal lines are suppressed in the presence of spinorbit coupling, unless they are protected by some topological symetries. We turn a two-dimensional (2D) material into a lattice with nonsymmorphic symmetry, by periotically removing selected atoms. As a case study, we investigate borophene (a honeycomb-like boron sheet). Pristine borophene is employed as the reference. While the Dirac cones of pristine borophene are gapped out by spinorbit coupling and magnetic exchange, robust nodal lines emerge in the energy spectrum of borophene with nonsymmorphic symmetry. We propose an effective 2D model and a symmetry analysis to demonstrate that these nodal lines are topological and protected by a nonsymmorphic glide plane. Our findings offer a paradigm shift to the design of nodal line semimetals: instead of searching for nonsymmorphic materials, robust nodal line semi-metals may be realized simply by removing atoms from ordinary symmorphic crystals.

Next, we study the the excitonic spectrum of 2D material and the heterostructure derivatives. Our approach takes into account the anomalous screening in two dimensions and the presence of a magnetic substrate. The Bethe-Salpeter equation is solved for a DFT-based tight-binding description of the single particle spectrum. We obtain the main features of the optical spectrum analyzing the localization in light zone of the excitonic peaks. We study the effect of different stacking forms on the main optical features of heterostructures, namely, the contributions of interlayer interaction, and the validity of valley polorizations. We compare the absolute magnitude of the linear optical conductivity.

Finally, we investigate the inter-/intra- valley scattering of carriers in 2D transition metal dichalcogenide monolayers. A detailed analysis of the electron-phonon and exciton-phonon inter-/intra- valley scattering is described. The scattering of electrons at conduction bands are studied by several teams, but the scattering of holes at valence bands is never reported yet, due to the big energy difference induced by spin-orbit coupling. To solve this issue, we study the scattering possibility by exciton exchange effect between different valleys.

Contents

LIST OF FIGURES

LIST OF TABLES

Chapter 1

Motivation and Purpose

"If at first the idea is not absurd, then there will be no hope for it."- Albert Einstein

1.1   Motivation

In 2004, the discovery of graphene with a honeycomb-like lattice structure aroused the enthusiasm of mankind to explore two-dimensional (2D) materials. Graphene is a 2D crystal structure formed by the arrangement of single-layer carbon atoms, and can exist stably in the natural environment, which opens up new explorations in the world of 2D materials, and a series of new knowledge is waiting for people to study and discover. The upsurge of 2D materials due to chemical research and development is coming quickly. At the beginning, people studied graphene and found that it has many excellent physical properties, such as ultra-high carrier mobility (up to more than $10^4 cm^2 V^{-1} s^{-1}$), linear dispersion relation of massless Dirac fermions, anomalous quantum Hall effect and even room temperature quantum Hall effect [11, 12, 13]. The absorption of light on graphene reaches 2.3% [14, 15]. Combined with that, it can withstand ultra-high current density (more than a million times that of copper). It has wide application prospects in transparent-conductive flexible electronics. However, the single-layer graphene itself is a Dirac semimetal without a bandgap, which limits its application in electronic devices. As an alternative route, isolated atomic planes can be reassembled into design heterostructures with a layer-by-layer strategy in a precisely chosen sequence using different materials, like a 'Lego game'. The ability to prepare isolated single atomic layers and reassemble them to form heterostructures layer-by-layer in a precise sequence, opens enormous possibilities for applications.

1.2   Summary of the following chapters

First, for 2D materials without bandgap, like semimetals or metals, the study on topological structure related nodal lines have attracted tremendous research interest recently, defined as topological nodal-line semimetals/metals (TNLSMs/TNLMs) [16, 17, 18]. Nodal lines can have different forms of band crossings: the band crossings of nodal lines can show both fourfold degeneracy and double degeneracy, which are known as Dirac and Weyl nodal lines, respectively. The

Dirac nodal lines are not much studies, therefore we will focus on the properties of Dirac nodal lines related with the topological properties of the crystals. Recently, nonsymmorphic symmetries [19], including slide mirror or screw axis operations, were discovered to guarantee the so-called symmetry-enforced semimetal with certain integer electron filling, which is unavoidably formed because of the unique band connectivity. For instance, we will specially study the protection of nonsymmorphic symmetries on Dirac nodal lines.

Next, we focus on the carrier dynamics of 2D materials, where the excitons will be well investigated. Many-body perturbation theory can calculate with a good precision neutral excitations (e.g. optical and energy-loss spectra), which is well described by the solution of the Bethe-Salpeter equation (BSE). The BSE is an approximate equation for two interacting particles that in our case couples the electron and the hole. It has been very successful in describing the absorption spectra of a large variety of systems: insulators, semiconductors, atoms, clusters, surfaces or polymers [20, 21]. There are some calculation package combining first principle methods with BSE, however, the computation cost is very expensive due to the bottleneck step of the 'all-band' calculation, which results in optical spectra based on modest reciprocal space sampling with poor resolution. Therefore we will work on a simplified code for BSE based on the wavefunctions from first principle calculation results.

As another important property of carrier dynamics of 2D materials, scattering of the exciton, especially the intervalley one, is predicted to play an important role in spin and valley pseudospin relaxation. Therefore, we will study the phonon-assisted scattering of excitons. Significant progress has been made in the understanding of the lattice dynamics in 2D materials as emphab initio simulations have enabled accurate computation of phonon spectra and the Gruneisen parameters [22]. Information about the relaxation of phonons, however, remains incomplete. This is due partly to the fact that the high-frequency transverse acoustic (TA) phonons are highly dispersive. Previous theoretical studies demonstrated that consideration of the phonon dispersion is critical in modeling the thermal conductivity, where phonons with low group velocities become fully excited. There exists significant discrepancy among phonon mean-free paths depending on which phonon branch was taken to dominate carrier transport.

Chapter 2

Introduction

2.1 Introduction to Density Functional Theory

At the beginning of the last century, the theory of quantum mechanics was initially established [23, 24, 25, 26, 27, 28]. Afterwards, with the joint efforts of many scientists, it has been developed and the theoretical framework has increasingly become complete, with more and more systems been handled. On the other hand, the appearance of the first computer in the 1840s heralded the beginning of human beings in the computer age, and post-modern computer technology, like other sciences, has also been rapidly improved, making it possible for researchers to use computers to solve some fundamental equations of quantum mechanics for a specific system. However, this is only a possible development trend, as it is very difficult to accurately solve a Schrödinger equation, and we still have a lot of preparatory work to do before this. The most important fixed interpretation equation is simplified. Because we can only solve the Schrödinger pendulum equation of chlorine atoms or ammonia-like atoms, we cannot directly solve the Schrödinger equation of complex systems, but can only use numerical methods to solve them. Therefore, if we want to obtain the physical and chemical properties of a system by solving the Schrödinger equation, we must perform some early simplifications on the Schrödinger equation. In this process, many methods have been proposed, but the most effective and most utilized are Born-Oppenheimer (BO) approximation and one-electron approximation. These two approximations make the Schrödinger equation truly become a form that can be processed based on Hartree-Fock (HF) equation or Kohn-Sham (KS) equation. If we consider this problem in terms of accuracy, the HF equation with the wave function as a variable can greatly improve the accuracy for solving the Schrödinger equation. The KS equation with electron density as a variable shows an unparalleled advantage in speed. Therefore, when solving practical problems, we can choose different methods to deal with the problems according to our needs. The above mentioned is how to simplify the Schrödinger equation to meet the form acceptable to the computer. The following is to improve the variables of this equation, and the density functional theory (DFT) is based on the KS equation theory, which greatly simplifies the computational complexity in the actual calculation, because for the wave function method, an electron has three degrees of freedom, and with the increase of the number of electrons, the required computational complexity will increase greatly. That's why we say that the

huge change proposed by DFT has really made a breakthrough in computational quantum physics. After determining DFT as the research direction of modern computational quantum mechanics, to find a more accurate exchange-related energy functional has become the next problem that we must conquer. Therefore, in this chapter, we briefly introduce the basic theory of computational quantum mechanics and the basic framework of DFT theory, followed by introducing some common software packages based on DFT theory.

2.1.1 Born-Oppenheimer approximation

Since its appearance in the 1920s, quantum mechanics has become a powerful tool for describing microscopic systems. Using quantum mechanics to quantitatively describe the motion of electrons can be used to explain and predict the physical and chemical properties of atoms and their molecules, solids and even more complex systems. The application of quantum mechanics to calculate the physical and chemical properties of the system is mainly to solve the Schrödinger equation of the system.

First of all, we know that for a multi-electron system, it is very difficult to directly find the wave function of this system, but we can change the way of thinking, that is, we can use many single-electron wave functions to form an appropriate wave function in a certain way. Without considering the relativistic effect and its evolution with time, the time independent Schrödinger equation has the following form:

$$H\Psi(\mathbf{r}, \mathbf{R}) = E\Psi(\mathbf{r}, \mathbf{R}) \tag{2.1}$$

and

$$
\begin{aligned}
H(\mathbf{r}, \mathbf{R}) = & -\sum_i \frac{\hbar^2}{2m_e}\nabla^2_{\mathbf{r}_i} + \frac{1}{2}\sum_{i,j} \frac{e^2}{|\mathbf{r}_i - \mathbf{r}_j|} - \sum_j \frac{\hbar^2}{2M_I}\nabla^2_{\mathbf{R}_I} \\
& + \frac{1}{2}\sum_{I,J} \frac{Z_I Z_J e^2}{|\mathbf{R}_I - \mathbf{R}_J|} - \sum_{I,j} \frac{Z_j e^2}{|\mathbf{r}_j - \mathbf{R}_I|}
\end{aligned} \tag{2.2}
$$

where $\mathbf{r}$ and $\mathbf{R}$ are the coordinates of electron and nucleus, respectively; M_I and m_e are the mass of nucleus and electron, respectively; the first term is the kinetic energy of the electron, the second term is the interaction energy between electrons and electrons, the sum is over all electrons except $i = j$, the third term is the kinetic energy of the nucleus, and the fourth term is the nucleus-to-nucleus energy, summed over all nuclei except $I = J'$, and the last term is the interaction energy of electrons and nuclei [29, 30, 31, 32, 33, 34].

Solving the wave function of the many-body Schrödinger equation rigorously is very difficult. The common practice is to use the Born-Oppenheimer (BO) approximation (or called adiabatic approximation, nuclear fixation approximation, and consider the motion of the nucleus's moving nuclear electrons) to simplify the problem. We know that the mass of the nucleus M_j is three orders of magnitude larger than that of the electron m_e, so the movement of the electron is much faster than that of the nucleus. Electrons are in high speed motion, while atomic nuclei only vibrate near their equilibrium positions. The small potential field changes caused by the nuclear motion, the electrons moving at high speed can always keep up with this change. Therefore, the above

many-body problem can be considered in two parts: when considering the motion of electrons, the nuclei are in their instantaneous positions, and when considering the motion of the nucleus, the specific distribution of electrons in space is not considered, which is the BO approximation.

With BO approximation, the Hamiltonian operator can be simplified as:

$$H(\mathbf{r}, \mathbf{R}) = -\sum_i \frac{\hbar^2}{2m_e}\nabla^2_{\mathbf{r}_i} + \frac{1}{2}\sum_{i,i'}\frac{e^2}{|\mathbf{r}_i - \mathbf{r}_{i'}|} - \sum_{i,j}\frac{Ze^2}{|\mathbf{r}_i - \mathbf{R}_j|} \tag{2.3}$$

where the second term is the many-body interactions are also the difficulty in solving this equation. The Hartree approximation is a one-electron approximation, proposed by Hartree in 1928 [35, 36, 37, 38]. He believed that complex electron interactions can be approximated as a single electron moving in an average field formed by other electrons and atomic nuclei, so that the entire multi-electron system can be described only by solving the movement of a single electron in a central potential field. Using this approximation, the many-body equation can be transformed into a one-electron equation:

$$H_i\Psi_i = E_i\Psi_i(\mathbf{r_i}), \tag{2.4}$$

with the wavefunction:

$$\Psi(\mathbf{r}) = \sum_j \psi_j(\mathbf{r}_j), \tag{2.5}$$

and the satisfied Hartree equation:

$$H_i = -\frac{\hbar^2}{2m_e}\nabla^2_{\mathbf{r}_i} + V(\mathbf{r}_j) + \sum_{j\neq i}\int\frac{|\psi_j(\mathbf{r}_j)|^2}{|\mathbf{r}_j - \mathbf{r}_i|}d\mathbf{r}_j \tag{2.6}$$

2.1.2 Hartree-Fock approximation

Since the Hartree wavefunction lacks the consideration of electron exchange antisymmetry, Fock changes it to the Slater determinant form, which satisfies the Pauli principle:

$$\Psi = \frac{1}{\sqrt{N!}}\begin{vmatrix} \Psi_1(\mathbf{r}_1,\phi_1) & \Psi_2(\mathbf{r}_1,\phi_1) & \dots & \Psi_N(\mathbf{r}_1,\phi_1) \\ \Psi_1(\mathbf{r}_2,\phi_2) & \Psi_2(\mathbf{r}_2,\phi_2) & \dots & \Psi_N(\mathbf{r}_2,\phi_2) \\ \vdots & \vdots & \vdots & \vdots \\ \Psi_1(\mathbf{r}_N,\phi_N) & \Psi_2(\mathbf{r}_N,\phi_N) & \dots & \Psi_N(\mathbf{r}_N,\phi_N) \end{vmatrix} \tag{2.7}$$

where ϕ is the spin (i.e. internal angular momentum) [39, 40, 41, 42, 43], and with the total energy:

$$\begin{aligned} E =&\langle\Psi|H|\Psi\rangle = \sum_i\int\Psi_i^*(\xi_i)H_i\Psi_i(\xi_i)d\mathbf{r}_i \\ &+ \frac{1}{2}\sum_{i,j}\int\frac{\Psi_i^*(\xi_i)\Psi_i(\xi_j)\Psi_j^*(\xi_i)\Psi_j(\xi_j) - \Psi_i^*(\xi_i)\Psi_j(\xi_j)\Psi_j^*(\xi_i)\Psi_i(\xi_j)}{|\mathbf{r}_i - \mathbf{r}_j|}d\mathbf{r}_id\mathbf{r}_j \end{aligned} \tag{2.8}$$

where $\xi_i = (\mathbf{r}_i, \phi_i)$. The corresponding single electron equation is:

$$\begin{aligned} \sum_j e_{ij}\Psi_j(\xi_i) =& \left[-\frac{\hbar^2}{2m_e}\nabla^2_i + V(\mathbf{r}_i)\right]\Psi_i(\xi_i) \\ &+ \sum_{i,j(i\neq j)}\frac{|\Psi_j(\xi_j)|^2}{|\mathbf{r}_i - \mathbf{r}_j|}\Psi_i(\xi_i)d\mathbf{r}_j - \sum_{i,j(i\neq j)}\frac{\Psi_j^*(\xi_j)\Psi_i(\xi_j)}{|\mathbf{r}_i - \mathbf{r}_j|}\Psi_j(\xi_i)d\mathbf{r}_j, \end{aligned} \tag{2.9}$$

where there is an extra term $\sum_{i,j(i\neq j)} \frac{\Psi_j^*(\xi_j)\Psi_i(\xi_j)}{|\mathbf{r}_i-\mathbf{r}_j|}\Psi_j(\xi_i)d\mathbf{r}_j$, which is the electron-electron exchange interaction. The Hartree-Fock (HF) method is a method of approximation for the determination of the energy of a quantum many-body system in a stationary state, in computational physics and chemistry. Eq. 2.9 is a nonlinear equation where every single electron wavefunction depends on other electrons. The state wavefunction needs to be solved by a self-consistent iterative method, which is known as the self-consistent field method (SCF).

The HF method is a fundamental method of quantum chemistry and its results are sufficiently precise. However, HF does not consider the relativistic effect and electron correlation effect in the equation, which makes the HF method unable to obtain the exact solution of the system. The relativistic effect is an effect due to the high kinetic energy of electrons in the inner shell of atoms, and this effect is quite significant for the inner shell electrons of heavy atoms and systems composed of them. Nonetheless, the inner shell electrons do not change significantly due to processes of general chemical interest. Therefore, when the system changes from one state to another, its relativistic effects can usually be ignored. The electron correlation effect is due to the fact that in the derivation of the HF equation, although the exchange interaction between electrons and electrons is considered, the repulsive interaction between spin-antiparallel electrons is not considered. The correlation energy is a measure of how much the movement of one electron is influenced by the presence of all other electrons, which accounts for about 1% of the total energy of the system, so the HF approximation is a good approximation when considering the total energy. However, when considering some chemical or physical processes, the physical quantities involved are often energy differences, and the electron correlation energy is equivalent to the reaction heat, activation energy and molecular bond energy of the chemical reaction, so for electronic excitation, reaction transition state, molecular chemical problems such as dissociation, bond energy calculation, etc., the errors caused by the correlation energy make the HF method unable to deal with these problems.

To consider the electron correlations, several theoretical approaches have been developed, including Configuration Interaction (CI)[44, 45, 46], Møller-Plesset perturbation theory (MPx) [47, 48, 49], density functional theory (DFT), etc. These methods are all *ab initio* methods because none of them use empirical parameters in their calculations.

However, due to the large amount of calculation of these methods, their scope of application is also limited by the size of the system. For the case of relatively large systems, some semi-empirical calculation methods have also been developed. The main idea is to simplify the single-electron Hamiltonian solution by introducing approximations, thereby reducing the amount of calculation and increasing the speed. There are also many semi-empirical methods, among which the method based on HF theory is to simplify the integral of two electrons, including Austin Model 1 (AM1) [50, 51], Parametric Method 3 (PM3) [52, 53, 54] etc. for larger systems. These methods have been well applied.

2.1.3 Theoretical Foundations of Density Functional Theory

The computational complexity of the *ab initio* method is too large, which greatly limits its application in large systems. For the HF method, the amount of calculation is proportional to N^3

(N is the number of particles) [55]. For the full configuration interaction method in the post-HF method, the calculation amount increases exponentially with N, and the MP2 method is proportional to N^5. The emergence of DFT solves these difficulties and has a significant improvement in the amount of calculation, which is probably proportional to N^2 or N^3 [56].

2.1.3.1 Thomas-Fermi-Dirac Approximation

The Thomas-Fermi model was proposed by Thomas and Fermi in 1927 [57, 58, 59]. This model considers the system to be a non-interacting electron gas, and the kinetic energy of electrons in the system can be described by a function of electron density $\rho(\mathbf{r})$. The electron density is a physical observable, it can be measured, calculated and easily visualized. For just one particle with its corresponding wavefunction $\varphi(\mathbf{r})$, the density is simply a probability amplitude to find a particle near a certain position in space, $\rho(\mathbf{r}) = \varphi^*(\mathbf{r})\varphi(\mathbf{r})$. The total energy of electron system in the external potential $V_{ext}(\mathbf{r})$ is:

$$E_{tot} = C_K \int [\rho(\mathbf{r})]^{5/3} d\mathbf{r} + e \int \rho(\mathbf{r})V_{ext}(\mathbf{r})d\mathbf{r} + \frac{1}{2}e^2 \int \frac{\rho(\mathbf{r})\rho(\mathbf{r}')}{|\mathbf{r} - \mathbf{r}'|}d\mathbf{r}d\mathbf{r}', \qquad (2.10)$$

where the parameter $C_K = \frac{2\hbar^2}{10m_e}(\frac{3}{8\pi})^{2/3}$. However, the approximation used in the model lacks a description of the exchange of electrons and related effects. In 1930 Dirac took into account the local approximation of electron exchange, which is the Thomas-Fermi-Dirac approximation [60, 61]. Therefore, the energy of electron in the external potential $V_{ext}(\mathbf{r})$ is:

$$E_{tot} = C_K \int [\rho(\mathbf{r})]^{5/3} d\mathbf{r} + e \int \rho(\mathbf{r})V_{ext}(\mathbf{r})d\mathbf{r} + \frac{1}{2}e^2 \int \frac{\rho(\mathbf{r})\rho(\mathbf{r}')}{|\mathbf{r} - \mathbf{r}'|}d\mathbf{r}d\mathbf{r}' + A \int [\rho(\mathbf{r})]^{4/3}d\mathbf{r}, \quad (2.11)$$

where $A \int[\rho(\mathbf{r})]^{4/3}d\mathbf{r}$ is the exchange energy with A and α being parameter. By looking for the lowest energy $E(\rho)$, the electron density of the ground state can be obtained. The Thomas-Fermi-Dirac model forms the basis of density functional theory, but because the approximation used is too simple, it ignores some essential phenomena in physics and chemistry, such as the shell structure of electrons, bonding in molecules, etc., and not widely used [62, 63].

2.1.3.2 Hohenberg-Kohn Theorem

In 1964, Hohenberg and Kohn proposed the Hohenberg-Kohn (HK) first and second theorem, which became a solid theoretical basis for density functional theory [64, 65, 66, 67].

Hohenberg-Kohn first theorem: For a multi-particle system interacting in an external potential V_{ext}, the external V_{ext} potential is uniquely determined by the ground-state particle density (which can differ by a constant.

The second Hohenberg-Kohn theorem: For a given external potential, the ground state energy of the system is equal to the minimum of the energy functional.

The first Hohenberg-Kohn theorem shows that there is a one-to-one correspondence between the external potential and the particle density. It ensures that the system density of states determines

the system ground state energy, wave function and other physical quantities. The variational method given by the second Hohenberg-Kohn theorem is the basis for applications of DFT. The system Hamiltonian is:

$$H = -\frac{\hbar^2}{2m_e}\sum_i \nabla_i^2 + \sum_i V_{ext}(\mathbf{r}_i) + \frac{1}{2}\sum_{i\neq j}\frac{e^2}{|\mathbf{r}_i - \mathbf{r}_j|}, \tag{2.12}$$

with the coresponding energy:

$$\begin{aligned} E_{HK}[\rho] &= T[\rho] + E_{int}[\rho] + \int V_{ext}\rho(\mathbf{r})d\mathbf{r} + E_{II} \\ &= F_{HK}[\rho] + E_{int}[\rho] + \int V_{ext}\rho(\mathbf{r})d\mathbf{r} + E_{II} \end{aligned} \tag{2.13}$$

where $T[\rho]$ is the kinetic energy of the system, $E_{int}[\rho]$ is the potential energy, V_{ext} is the external potential, and E_{II} is the interaction energy of the nucleus. Hohenberg-Kohn theorem gives a way to determine the ground state of the system by the variation of the particle number density function.

2.1.3.3   Kohn-Sham Equation

In 1965, Kohn and Sham introduced a hypothetical multi-electron system without interaction, which has the same charge density as the real multi-electron system, thereby constructing a hypothetical orbital with multiple single electrons (KS orbital). For a hypothetical system, the kinetic energy T_S can be expressed as:

$$T_S = -\frac{1}{2}\sum_\phi \sum_{i=1}^{N^\phi} \langle \Psi_i^\phi(\mathbf{r})|\nabla^2|\Psi_i^\phi(\mathbf{r})\rangle = -\frac{1}{2}\sum_\phi \sum_{i=1}^{N^\phi} \int |\nabla\Psi_i^\phi(\mathbf{r})|^2 d\mathbf{r}, \tag{2.14}$$

and the Coulomb interaction of the system (the Hartree term) can be writen as:

$$E_{Hartree}[\rho] = \frac{1}{2}\int \frac{\rho(\mathbf{r})\rho(\mathbf{r}')}{|\mathbf{r}-\mathbf{r}'|}d\mathbf{r}d\mathbf{r}' \tag{2.15}$$

Finally, with Kohn-Sham approximation, we can get the detailed functional expression of the system energy:

$$E_{KS} = T_S[\rho] + \int V_{ext}(\mathbf{r})\rho(\mathbf{r})d\mathbf{r} + E_{Hartree}[\rho] + E_{II} + E_{xc}[\rho], \tag{2.16}$$

where the complex interactions in the system are all placed in the exchange-related term $E_{xc}[\rho]$, which includes the energy differences of the kinetic and internal energy between the real system and the hypothetical system. Further the Kohn-Sham equation can be obtained by variational principle:

$$[-\frac{\hbar^2}{2m_e}\nabla^2 + V_{ext}(\mathbf{r}) + V_{xc}(\mathbf{r})]\Psi_i^{KS}(\mathbf{r}) = \varepsilon_i^{KS}\Psi_i^{KS}(\mathbf{r}), \tag{2.17}$$

where the term $V_{xc}(\mathbf{r})$ is the exchange correlation potential, and the electron density can be obtained by solving the eigenfunction of the equation, so self-consistent iterative solution is required

for the Kohn-Sham equation. When the self-consistently convergent system charge density n_0 is obtained, the total energy of the system is obtained.

It should be noted that in the Hartree-Fock equation, the eigenvalues correspond to the increase or decrease of the energy of an electron in the multi-particle system, while the eigenvalues in the Kohn-Sham equation have no actual physical meaning [65]. Compared with Hartree-Fock, the computational cost of the density functional is reduced, and the accuracy is greatly improved. It is an *ab initio* theory based entirely on quantum mechanics and is now an important method for calculating properties of condensed matter and macromolecular systems. Therefore, Kohn got the Nobel Prize in Chemistry in 1998.

2.1.3.4 Exchange Correlation Functional

The difficulty of density functional theory lies in how to obtain the exact form of the exchange correlation functional $E_{xc}[\rho]$. Exchange related items can generally be divided into two parts: exchange effect and correlation effect. There are already several approximations to get $E_{xc}[\rho]$.

As a simple approximation, Kohn and Sham replace the non-homogeneous electron gas $E_{xc}[\rho]$ with the homogeneous one [68, 69, 70, 71]. This simple approximation is common local density approximation (LDA), whose $E_{xc}[\rho]$ has the following form:

$$E_{xc}^{LDA}[\rho] = \int \rho(\mathbf{r})\epsilon_{xc}(\rho(\mathbf{r}))d\mathbf{r}, \tag{2.18}$$

where $\epsilon_{xc}(\rho(\mathbf{r}))$ is the exchange-correlation energy per particle of a homogeneous electron gas of charge density $\rho(\mathbf{r})$. The LDA works remarkably well for a wide variety of materials, especially in the calculations of equations of state, elastic constants, and other properties of silicates. Cell parameters and bulk moduli obtained from well-converged calculations often agree with the experimental data within a few percent and $\approx 10\%$, respectively [70]. Agreement with the laboratory data is not perfect, however, some systematic discrepancies are noted for some materials.

When the spin is consindered, it turns into local spin density approximation (LSDA), where the exchange related energy is:

$$E_{xc}^{LSDA}[\rho^\uparrow, \rho^\downarrow] = \int \rho(\mathbf{r})\epsilon_{xc}(\rho^\uparrow(\mathbf{r}), \rho^\downarrow(\mathbf{r}))d\mathbf{r}, \tag{2.19}$$

where $\rho^\uparrow(\mathbf{r})$ and $\rho^\downarrow(\mathbf{r})$ are electron densities with different spins. LSDA is the most general local approximation, for non-polarized systems $\rho^\uparrow(\mathbf{r}) = \rho^\downarrow(\mathbf{r}) = \rho(\mathbf{r})/2$.

Since exchange-correlation is a short-range interaction, LDA has achieved great success, leading to a wide range of applications of density functional theory. However, for heavy atoms, the continuous decay of its spatial electron density is 0 as the distance to the atom increases. In this case, LDA cannot give very good results, which promotes the development of various generalized gradient approximations (GGA) [72, 73].

For practical systems, the charge density will naturally not be as uniformly distributed as in an ideal uniform free electron gas. Adding further gradients in charge density produces GGAs.

Under GGA, E_{xc} is not only a functional of charge density $\rho(\mathbf{r})$, but also a function of the gradient of charge density $|\nabla_\rho(\mathbf{r})|$:

$$
\begin{aligned}
E_{xc}^{GGA}[\rho^\uparrow, \rho^\downarrow] &= \int \rho(\mathbf{r})\epsilon_{xc}(\rho^\uparrow(\mathbf{r}), \rho^\downarrow(\mathbf{r}), |\nabla_{\rho^\uparrow}(\mathbf{r})|, |\nabla_{\rho^\downarrow}(\mathbf{r})|, \cdots)d\mathbf{r} \\
&= \int \rho(\mathbf{r})\epsilon_{xc}^{hom}(\rho(\mathbf{r}))F_{xc}(\rho^\uparrow(\mathbf{r}), \rho^\downarrow(\mathbf{r}), |\nabla_{\rho^\uparrow}(\mathbf{r})|, |\nabla_{\rho^\downarrow}(\mathbf{r})|, \cdots)d\mathbf{r},
\end{aligned}
\tag{2.20}
$$

where F_{xc} is a dimensionless quantity, $\epsilon_{xc}^{hom}(\rho(\mathbf{r}))$ is the exchange energy of non-polarized homogeneous electron gas. The commonly used GGA approximations are Becke1988 [74], PW91 [75] and Perdew-Burke-Ernzerhof (PBE) [76].

For some gapped systems, LDA and GGA results are not good and tend to underestimate the bandgap. In addition, in order to improve the calculation accuracy, better exchange correlation functionals are needed. One method is the linear combination of Hartree-Fock exchange term and DFT exchange terms to improve the functionals:

$$
E_x = \alpha_1 E_x^{HF} + \alpha_2 E_x^{DFT},
\tag{2.21}
$$

where $\alpha_{1/2}$ is the coordinate.

After the above construction, the finally obtained exchange-correlation energy functional is often more accurate, and has been widely used in practical calculations.

2.1.3.5 van der Waals density functional method (vdW-DFT)

Although DFT has been greatly improved, it is still difficult to properly describe intermolecular interactions, especially van der Waals forces. The van der Waals force is caused by the electrostatic interaction between molecules or atoms. It was originally proposed to modify the van der Waals equation, and it generally exists between any particles in solid, liquid and gas states. There are three types of van der Waals forces: inductive force, dispersion force and orientation force. Van der Waals forces play an important role in accurately describing weak interactions between noble gases, biomolecules, polymers, and layered structures.

At present, a variety of different vdW-DFT methods have been developed [77, 78, 79, 80], mainly including the following four methods: the first method is to add a simple dispersion force correction on the basis of the previous density functional, among which the DFT-D method proposed by Grimme is the most widely used [81]; the second method is proposed by Becke, adding the Hartree-Fock equation to the previous density functional [74]; the third method is the method based on transformed pseudopotential proposed by Lilienfeld [75]; the fourth method is the method of constructing a new van der Waals density functional, among which the vdW-DFT functional proposed by Dion is the most widely used [82].

2.2 Optical/Electrical Properties of 2D Materials

In 2010, Konstantin Novoselov and Andre Geim were awarded the Nobel Prize for their first experimental report on two-dimensional (2D) material graphene. In graphene, carbon atoms create

an in plane lattice of σ bonds and π bonds formed by sp^2 hybrid orbitals and out-of-plane p_z orbitals, respectively, which results in a honeycomb crystal lattice structure as shown in Fig. 2.1a). Graphene is the most studied 2D material due to its ease of synthesis and superior properties over other materials such as high Young's modulus (strongest material ever tested), optical transparency, excellent thermal conductivity and high mobility of charge carriers because of the massless Dirac fermions which originate from the out of plane p_z orbitals.
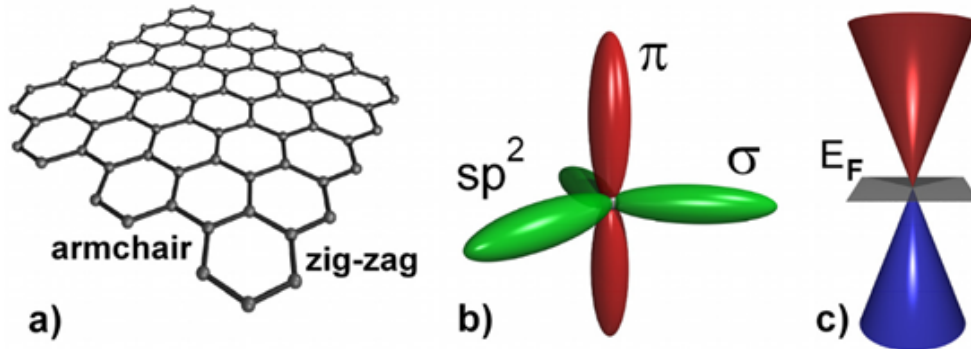
Figure 2.1: a) Schematic of a graphene crystallite with characteristic armchair and zig-zag edges. b) Schematic of orbits of one carbon atom in graphene. c) Band diagram of graphene around Dirac cone [1]

Following the synthesis of graphene [83, 84, 85], immense amount of research has been conducted in the field of 2D materials, including silicene [86], germanene [87], stanene [88] in Group IV, and phosphorene [89], antimonene [90], boronphene [91]. Those 2D materials were realized experimentally and also investigated in detail by advanced computational methods. The ground state bulk form of carbon is graphite (vertical stack of graphene sheets) whereas for borophene it is boron with regular icosahedron structure.

2.2.1 Basic Properties of Boronphene

Borophene is a crystalline atomic monolayer of boron, which is also known as boron sheet [92]. I. Boustani and A. Quandt reported the first computational prediction of boron cluster at 1997, and showed that small boron clusters do not adopt icosahedral geometries like boranes, instead they turn out to be quasi-planar [93]. Afterwards people predicts the possibility of borophene (boron sheets) [93], boron fullerenes (borospherene) [94] and boron nanotubes [95]. These studies showed that extended, triangular borophene is metallic and adopts a non-planar, buckled geometry. Further computational studies, initiated by the prediction of a stable B80 boron fullerene [95], suggested that extended borophene sheets with honeycomb structure and with partially filled hexagonal holes are stable.

The synthesis of borophene is reported recently. Early theoretical works have shown that the metal substrate is critical for stabilizing 2D boron clusters rather than their 3D forms, leading to the kinetically favored growth of 2D boron sheet on the substrate, along with the gradual decrease in stability of the 2D boron clusters with increasing cluster size. Ideally, the substrate must have

sufficient adhesion to boron atoms to enable surface wetting by the deposited boron, but it should not form a chemical bond between boron atoms and substrate [96]. Metal substrates with specific facets, such as Ag(111) [97], Au(111) [98], Cu(111) [99], and Al(111) [100], have been proven to be suitable for depositing 2D boron clusters. These crystal facets can passivate the 3D growth of boron and stabilize its sp^2 hybridization, thus leading to the formation 2D clusters. Guided by theoretical works, several research groups have experimentally fabricated 2D borophene sheets on Ag(111) surface under UHV conditions, as shown in Fig. 2.2.
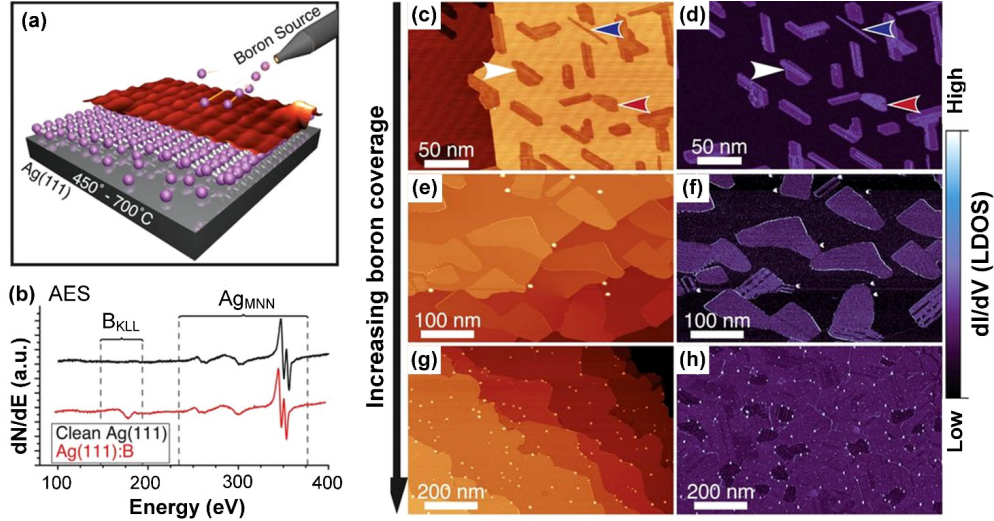
Figure 2.2: (a) Schematic diagram showing the growth setup of borophene sheets on Ag(111) surface with atomic structure model and STM topography rendering. These borophene sheets were grown on Ag(111) surface using a solid boron rod as the boron source under UHV conditions (base pressure of 1011 mBar). (b) AES spectra of clean Ag(111) prior to and after the growth of borophene. (c-h) A series of largescale STM topography (left) and closedloop dI/dV (right) images of borophene sheets, showing the increase of B coverage.

2.2.2   Basic Properties of Transition Metal Dichalcogenides

Although graphene has very good application prospects in gas sensing, catalysis and other fields, there are serious deficiencies in the application of field effect transistors, which is determined by the semi-metallic properties of graphene. Although theoretical and experimental studies have shown that the bandgap of graphene can be increased by applying a longitudinal electric field and doping modification, the control range of bandgap is very small (less than 200meV), which is not suitable for field effect transistor logic devices [101, 102, 103]. Therefore, to make full use of the advantages of 2D nanomaterials, it is necessary to develop functional devices based on 2D semiconductor materials, and the emergence of transition metal dichalcogenides (TMDs) has significantly broadened the application of 2D semiconductor nanomaterials in fields such as energy storage, nanoelectronics, sensor, etc.

2.2.2.1 Structure and Preparation of Transition Metal Dichalcogenides

TMDs, including MoS_2, WS_2, $MoSe_2$, WSe_2 etc, show a wide range of electronic, optical, mechanical, chemical and thermal properties that have been studied by researchers for decades. TMDs are an interesting family of 2D materials with an X-M-X layered structure, where M is a transition metal element from 3 to 12 groups, typical of group IV (Ti, Zr, Hf and so on), group V (for instance V, Nb or Ta) or group VI (Mo,W and so on), and X is a chalcogen (S, Se or Te) as displayed in Fig. 2.3. The atoms in these sandwich structure are strongly held together by covalent bonds, whereas each three-plane sheet is only linked to its neighbors by weak van der Waals bonds, allowing individual sheets to be separated from each other. Until now, the most reported TMDs mainly include MoS_2, WS_2, VS_2, $MoSe_2$ and WSe_2. The heightened interest in these materials has been naturally accompanied by a rapid development of methods for the synthesis, classified into top-down and bottom-up methods.
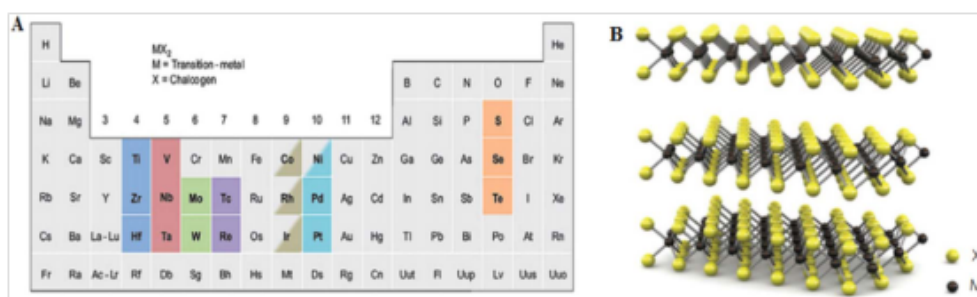
Figure 2.3: (A) Highlighted elements in the Periodic Table show those that form layered transition-metal dichalcogenides. Note that partial highlights for Co, Ni, Rh and Ir denote that only some of the dichalcogenides formed are layered. (B) The sandwich structure of TMDs, where the transition metal atom M is localized between the two hexagonal planes of chalcogen atom X [2]

Top-down method is aimed at changing bulky and layered compounds into mono- and few-layer 2D TMDs, including mechanical exfoliation, liquid exfoliation and chemical or electrochemical exfoliation. The mechanical exfoliation is derived from "scotch tape" method for graphene. The process of liquid exfoliation has also been extensively used to exfoliate layered compounds into 2D nano-materials, basically involving two processes intercalation and sonication. Direct liquid exfoliation (also called as sonication assisted exfoliation in solvents or aqueous surfactant solutions) is the most suitable route for large scale production of 2D MoS_2 [104, 105, 106]. Bottom-up synthesis strategies mainly include chemical vapor deposition (CVD) and solvo-/hydro- thermal methods. Due to some reports, solvo-/hydro- thermal methods are simple, scalable and readily controlled, and the CVD method is a typical bottom-up process that commonly used to prepare 2D nano-materials [107, 108, 109]. The latter not only can prepare continuous single film with certain thickness, but highlight in directly growth layered heterostructures, which would largely avoid interfacial contamination introduced during layer by layer transfer process.

Researchers used Raman spectroscopy to study the phonon vibrational laws of MoS_2 with different layers [110]. As shown in Fig. 2.4, the phonon vibration modes of MoS_2 mainly include the $in-plane$ vibration mode E_{2g} (a double-degenerate vibration that is symmetric under inversion)

and the $out-of-plane$ vibration mode A_{1g} (a non-degenerate total-symmetric vibration), and these two main vibration modes change with the change of thickness. It is shown that the A_{1g} mode is blue-shifted, while the E_{2g} mode is red-shifted. However, the phenomenon that the vibration frequency shifts in the opposite direction cannot be explained only by the van der Waals interlayer coupling. The vibrational frequency varies with the thickness of MoS_2, mainly due to the Coulomb interaction and the change of the intralayer bonding mode induced by the interlayer stacking. This study helps us to quickly identify the thickness of MoS_2 by Raman spectroscopy. Using photoluminescence spectroscopy and reflectance spectroscopy, it experimentally confirmed the variation of the band gap of MoS_2 with thickness for the first time: a single-layer MoS_2 has a direct band gap of 1.8eV, while the multilayer MoS_2 has an indirect band gap of about 1.2eV. As shown in Fig. 2.4b, the photoluminescence intensity of the monolayer MoS_2 is very high, indicating that the monolayer MoS_2 has a high recombination efficiency of photogenerated electron-hole pairs due to the existence of the direct band gap. There are two distinct characteristic peaks in its photoluminescence spectrum and reflectance spectrum, corresponding to A and B excitons respectively, which are caused by the spin-orbit interaction in MoS_2, due to the splitting of valence band energy levels at K point of the Brillouin zone.
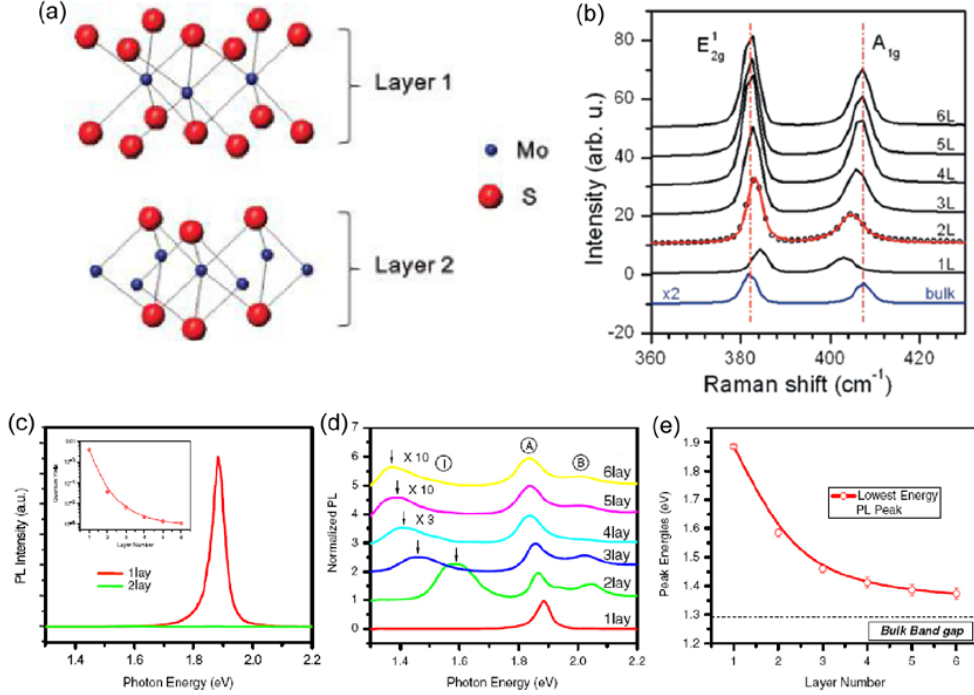
Figure 2.4: Raman and PL spectra of MoS_2 with different layers. (a) Schematic illustration of MoS_2 structure. (b) Raman spectra of MoS_2 with differet layers. (c-d) The photoluminescence performance and (e) bandgap of MoS_2 with different layers [3, 4].

2.2.2.2 Applications of Transition Metal Dichalcogenides

As a class of 2D layered materials, TMDs have been explored in possession of illustriously nonlinear optical properties (such as broadband saturable absorption, high third-order nonlinear

susceptibility, and strong light-matter interactions). Therefore, TMDs have been employed as saturable absorption materials in pulsed laser systems at different operation wavebands in previous researches. The interactions between neighboring layers of TMDs are bonded by weak Van der Waals forces resulted from fully saturated chemical bonds on the surface of a single layer of TMDs, which provides an exciting opportunity to construct heterostructures by vertically stacking different TMDs in turns to obtain desired functional devices without considering mismatch problem. Therefore, TMD-based heterostructures have gained a great deal of interest for exploring new physics behaviors and novel functional devices in photonics and optoelectronics. For example, MoS_2-WS_2 heterostructure has been observed with excellent properties, such as a strong interlayer excitonic transition, enhancement of localized photoluminescence, and ultrafast charge transfer. The conduction band minimum and valence band maximum reside in two separate materials, therefore the photo-excited electrons and holes prefer to stay at separate locations. Fig. 2.5-a illustrates the alignment of electronic bands of MoS_2 and WS_2 monolayers as predicted, where monolayer MoS_2 and WS_2 has a bandgap of 2.39 eV and 2.31eV, respectively, and the MoS_2 valence band maximum is 350 meV lower than that of WS_2. Neglecting the hybridization of electronic states in MoS_2 and WS_2 layers, the MoS_2/WS_2 heterostructure forms a type-II heterojunction, where the conduction band minimum residing in MoS_2 and the valence band maximum in WS_2, respectively. In the single-particle picture, this heterojunction will lead to efficient charge transfer with separated electron and holes in two layers upon optical excitation, leading to a dominating effect on both light emission and photovoltaic responses in MoS_2/WS_2 heterostructures.
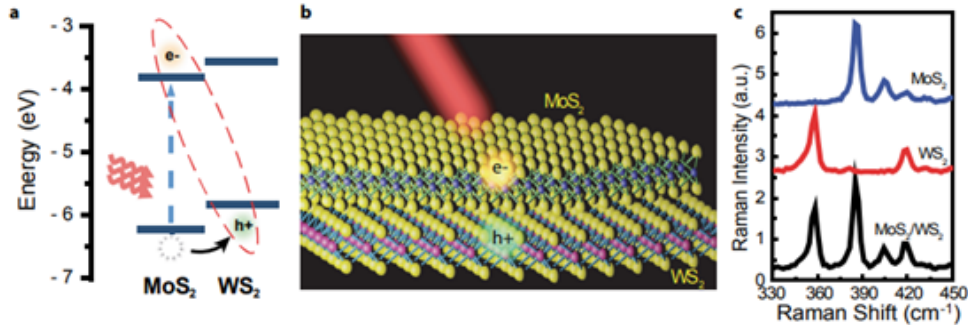
Figure 2.5: Band alignment and structure of MoS_2/WS_2 heterostructures. a. Schematics of theoretically predicted band alignment of a MoS_2/WS_2 heterostructure, which forms a type-II heterojunction. Optical excitation of the MoS_2 A-exciton will lead to layer separated electron and hole carriers. b. Illustration of a MoS_2/WS_2 heterostructure with a MoS_2 monolayer lying on top of a WS_2 monolayer. Electrons and holes created by light are shown to separate into different layers. c. Raman spectra of an isolated MoS_2 monolayer (blue trace), an isolated WS_2 monolayer (red trace), and a MoS_2/WS_2 heterostructure (black trace) [32]. [5].

Field Effect Transistor

Due to its wide band gap, MoS_2 can be applied to field effect transistors. Radisavljevic prepared a single-layer MoS_2 top-gate field effect transistor with a carrier mobility as high as 200 cm^2/(Vs), a threshold swing as low as 74 mV/dec, and a current ON/OFF ratio of more than 108, as shown in

Fig. 2.6. Pu fabricated CVD-grown MoS_2 flexible thin-film transistors using ionic liquid dielectrics as gates with very low threshold voltage (smaller than 1V) , high carrier mobility (12.5 cm^2/(Vs)), and high current ON/OFF ratio, and the flexibility of the transistor was mainly determined by the atomic-scale MoS_2 film thickness and the strong Mo-S bonding [111]. MoS_2 in its native state is an n-type semiconductor, but Zhang created bipolar MoS_2 transistors by introducing the electric double layer (EDL) effect that exists in ionic liquids. Due to the strong capacitance of the EDL in the MoS_2 trench, the n-type and p-type MoS_2 FETs exhibit symmetry, high density of electrons and holes, and comparable conduction paths for electrons and holes [112].
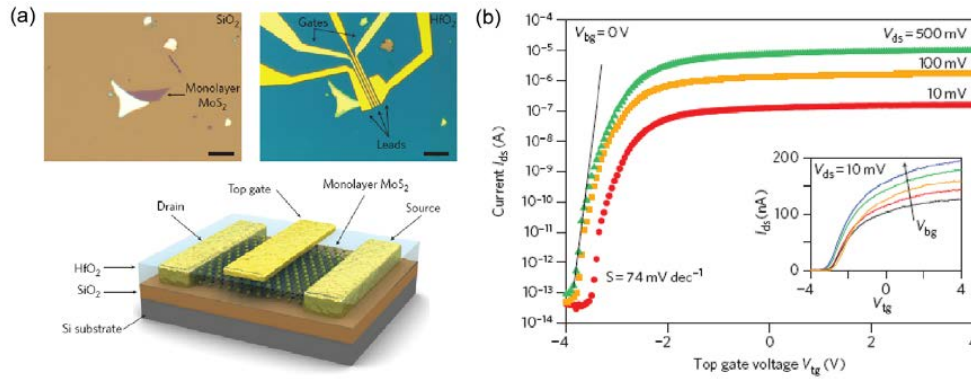
Figure 2.6: The fabrication of monolayer MoS2 top-gated field effect transistor (a) and the transfer characteristic (b) [6].

Phototransistor/Photodetector

Due to the relatively suitable band gaps of transition metal chalcogenides such as MoS_2, the interaction between light and matter in MoS_2 is very strong. For example, Bernardi's calculations show that the absorption rate of single-layer or multi-layer MoS_2 for visible light reaches 2.3%, which is one order of magnitude higher than that of commercially commonly used Si and GaAs [113]. Therefore, it has a good application prospect in the field of optoelectronic devices. As shown in Fig. 2.7 a,b, Zhang studied the optoelectronic properties of monolayer MoS_2 phototransistors for the first time, and found that the photoresponse coefficient reached 7.5 when the electron concentration in MoS_2 was high (that is, when the gate voltage was high)7.5 mA/W, which is one to two orders of magnitude higher than that of graphene photodetectors [7]. Due to the large resistance in the contact area of Au-MoS_2, Lopez-Sanchez chose a metal with low work function, to further reduce the electrical contact barrier between the single-layer MoS_2 and the metal electrode, and improve the electrical performance of the single-layer MoS_2 device [114]. At the same time, the maximum photocurrent region (ie, the photosensitive region) of the monolayer MoS_2 device was determined by scanning photocurrent microscopy (SPCM), and the photoresponse measurement was carried out in this region. It was found that the photoresponse coefficient of the monolayer MoS_2 was as high as 880 A/W, and the cut-off wavelength was 680 nm, which was directly related to the monolayer MoS_2. The band gap (1.8eV) position corresponds exactly as shown in Fig. 2.7 c-f. It should be pointed out that the measurement of the photoresponse coefficient is carried out in the OFF state of the transistor, where the photocurrent is very sensitive to the change of light intensity. With the increase of light intensity, the photocurrent increases linearly and rapidly, while

the photoresponse coefficient decreases gradually. Lee fabricated a top-gate MoS_2 phototransistor using the transparent conductive electrode ITO as the top electrode, and studied the response of monolayer to trilayer MoS_2 to different wavelengths of visible light. The results show that the trilayer MoS_2 transistor has a strong photodetection effect on red light. , and the single-layer and double-layer transistors have a good detection effect for green light, which is completely consistent with the band gaps of single-layer to triple-layer MoS_2 (the band gaps of single-layer to triple-layer MoS_2 are 1.8 eV, 1.65 eV and 1.35 eV, respectively).
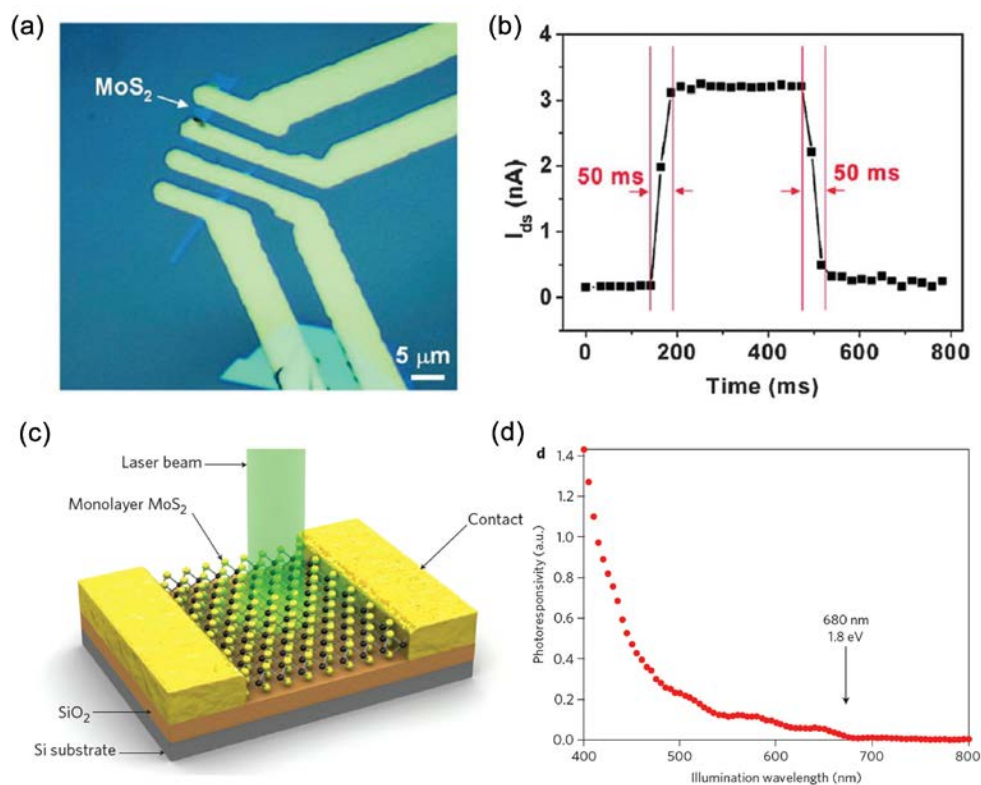
Figure 2.7: The fabrication of monolayer MoS_2 top-gated field effect transistor (a) and the transfer characteristic (b) [7].

2.2.2.3 Structure and Optical/Electronic Properties of TMDs Heterostructure Devices

The continuous emergence of 2D materials with different physical properties over the past decade has led to the rise of another new class of materials, namely van der Waals (vdWs) heterostructures. As shown in Fig. 2.8, vdWs heterostructures are formed by stacking two or more 2D nanomaterials under the interaction by vdWs forces. Strong covalent bonds ensure 2D nanomaterials with highly "in-plane" stability. The "out-of-plane" vdWs interactions are much smaller than covalent interactions, but it is enough to make different 2D nanomaterials tightly combined.

Van der Waals heterostructures can combine the advantages of 2D nanomaterials, but also may produce some novel physical properties, such as superlattice Dirac points and tunneling effects, due to the quantum coupling between 2D nanomaterials. Compared with traditional semiconductor
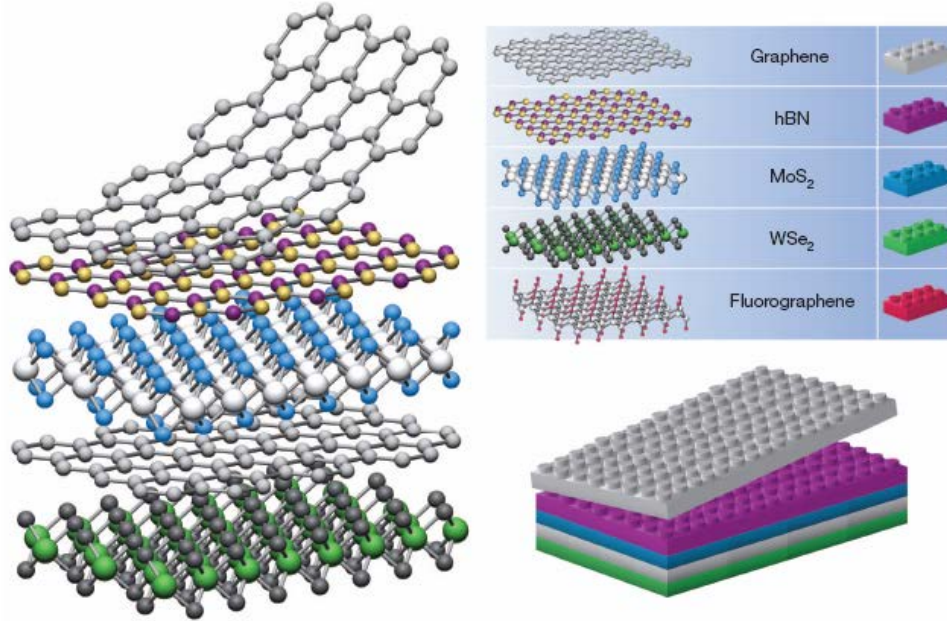
Figure 2.8: Building van de Waals heterostructures with various of 2D materials.

heterostructures, since there are no dangling bonds on the surface of 2D materials, the interface of vdWs heterostructures does not need to satisfy the lattice matching condition, and the interface is very narrow. The construction methods of vdWs heterostructures mainly include mechanical transfer and chemical growth, such as chemical vapor deposition, molecular beam epitaxy and so on. Considering the simple construction method of vdWs heterostructures and the many types of 2D nanomaterials (including insulators, semiconductors, semi-metals, etc.), we can easily design and fabricate different types of vdWs heterostructure devices to meet application requirements. Among the vdWs heterostructures currently studied, the vdWs heterostructures based on TMDs have important practical value, because TMDs have a suitable forbidden band width (from the near-infrared band to the visible region), very strong light-matter The interaction and very rich electronic structure (such as spin-orbit hybridization, valley spin, etc.) make it have broad application prospects in the fields of optoelectronics, photovoltaics and valley devices. From the perspective of optoelectronic applications, such as LEDs and photodetectors, the behavior of photogenerated electron-hole pairs (excitons and charged excitons) largely affects the optical properties of TMDs heterostructures, thereby affecting the device performance. Photoelectric efficiency and other properties. In the following, we mainly introduce the optoelectronic behavior and exciton state behavior of vdWs heterostructures composed of transition metal chalcogenides.

2D/3D Materials with Heterostructure

Integrating 2D atomic crystals with 3D bulk materials to develop lower-cost and higher-efficiency photovoltaic devices, such as MoS_2/Si or MoS_2/CNT, is very important for the development of heterostructure functional devices. Since silicon is abundant in nature with high photovoltaic conversion efficiency, silicon-based photovoltaic devices are widely used. Integrating 2D nanomaterials with silicon can meet the requirements of low-cost and high-performance

devices. As shown in Fig. 2.9a, Lopez transferred the mechanically exfoliated monolayer MoS_2 onto p-Si substrate to realize the MoS_2/p-Si heterostructure, and the electrical curve has diode characteristics in dark field, confirming the existence of p-n junction between MoS_2 and p-Si [115]. Under illumination, the reverse current increases, with the short-circuit current and open-circuit voltage appeared, which indicates that the photo-generated electron-hole pairs are separated under the action of the $built-in$ electric field to form the photocurrent. In addition, the MoS_2/p-Si heterostructure has good electroluminescence properties. These results all indicate that there is effective charge transfer at the interface between MoS_2 and Si. Hersam's group used p-type carbon nanotube (CNT) films and n-type monolayer MoS_2 to construct a p-n junction, and studied the application of p-n junction optoelectronic devices [115], as shown in Fig. 2.9d. Since the polarity of carbon nanotubes can be regulated by an applied electric field, the rectification characteristics of MoS_2/CNT p-n junction can be changed by adjusting the gate voltage, and the forward/reverse current ratio is as high as 104, as shown in Fig. 2.9e. According to the scanning photocurrent distribution in Fig. 2.9 f, it can be seen that the photocurrent of the device is generated in the over-lapping area of MoS_2 and CNT film, indicating that the $built-in$ electric field of the MoS2/CNT p-n junction area can effectively separate photogenerated electrons-hole pair. The heterostructure device is highly responsive to light, with an external quantum efficiency of up to 25%, and a response speed of less than 15 µs.
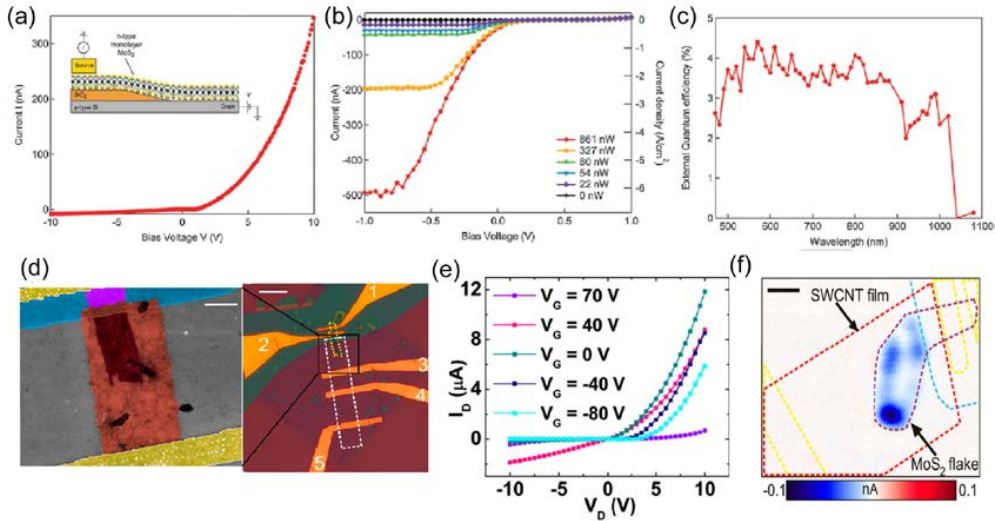
Figure 2.9: Optoelectronic performance of MoS_2/bulk heterojunction. (a) I-V characteristic MoS_2/Si in the dark showing diode-like behavior. (b) I-V characteristic under illumination with wavelength of 514 nm and varying optical power. (c) External quantum efficiency as a function of excitation wavelength. (d) Optical image of MoS_2/CNT p-n junction devices. (e) I-V character-istic of MoS_2/CNT device with varying gate bias. (f) The photocurrent mapping of MoS_2/CNT device.

TMD/TMD Heterostructure

The n- or p-type semiconductor transition metal chalcogenides have suitable band gaps and can be used to fabricate ultrathin $p-n$ junctions for highly sensitive photodetection. As shown in Fig. 2.10 a,b, Lee fabricated atomically thick $p-n$ junctions composed of monolayer MoS_2 and WSe_2

for the first time [116]. It has good diode characteristics and photovoltaic characteristics, and can be effectively controlled by the grid electric field. Different from the traditional semiconductor p-n junction, the majority carriers in each layer recombine through tunneling after illumination, and this recombination modulated by interlayer tunneling plays an important role in the formation of photocurrent. Considering the low lateral mobility of carriers in TMDs, the diffusion time for many carriers to move to the junction region is as long as 1 μs, resulting in the coexistence of photocurrent generation and interlayer recombination of photogenerated electron-hole pairs. In order to further reduce the interlayer recombination efficiency of photogenerated electron-hole pairs and increase the concentration of photogenerated carriers in the junction region, Lee used graphene as an electrode to prepare graphene/WSe$_2$/MoS$_2$/Graphene vertical heterostructure. In this case, the carriers can be accumulated by charge transfer in the vertical direction, rather than by lateral diffusion. Vertical heterostructures also produce photovoltaic properties, with photoresponse coefficients that are 5 times higher than lateral heterostructures.

Cheng confirmed that the WSe$_2$/MoS$_2$ $p-n$ junction photocurrent was formed in the stacked region using scanning photocurrent microscopy [117], and the photoelectric conversion efficiency was as high as 12%, as shown in Fig. 2.10 c. Fig. 2.10 d,e is the electroluminescence spectrum of the forward biased system under forward current, and the electroluminescence spectrum is concentrated near the electrode. As the bias voltage increases, the EL intensity increases. The thermionic fluorescence is found in WSe$_2$ by electroluminescence measurements. Since thermionic fluorescence is generally related to the energy level splitting of the ground and excited states induced by the electron-orbital interaction, it indicates that the interlayer perturbation between the heterostructures has a great influence on the electron-orbital interaction in WSe$_2$, which is consistent with the observed interlayer exciton states in TMD/TMD heterostructures.
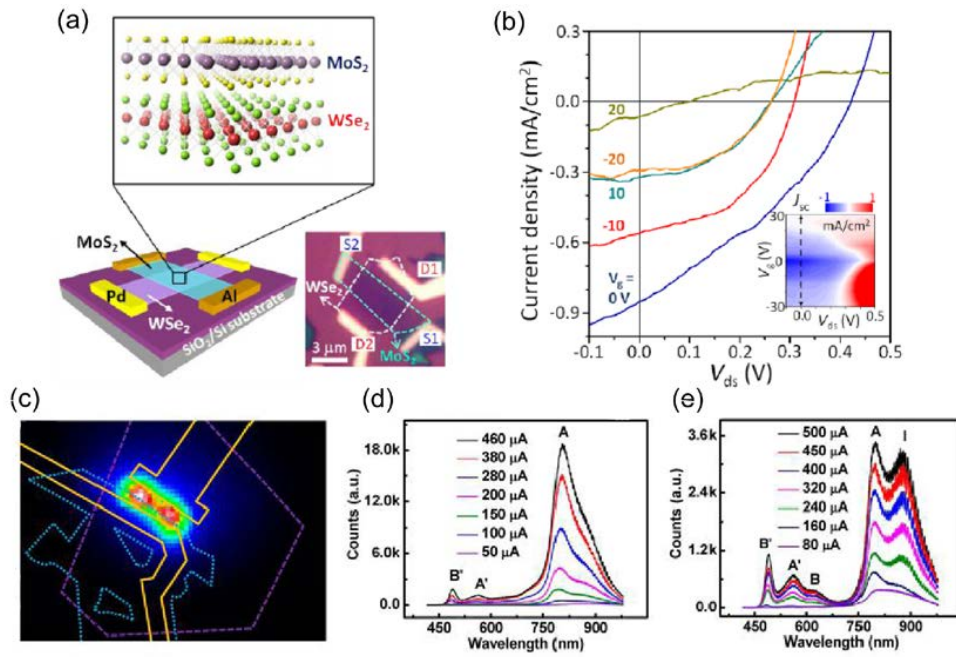
Figure 2.10: Optoelectronic performance of WSe_2/MoS_2 heterostructures. (a) Schematic representation of the single layers composing the heterostructure. (b) I-V characteristics under illumination at different gate bias. (c) The photocurrent mapping of WSe_2/MoS_2. (d,e) Electroluminescence spectra of WSe_2/MoS_2 under different forward current.

Chapter 3

Nodal Lines in Gapless Topological 2D Materials

This chapter presents the Dirac Nodal lines in 2D single-layer material borophene. By First principle calculation and symmetry analysis of effective models, we show the relationship between Dirac Nodal lines and topological properties of crystal.

3.1 Introduction

Following the rising of topological insulators, Topological semimetals (TSMs) [118] have become one of the most attractive materials in condensed matter physics. Different from normal metals, the Fermi surface of TSMs consists of nontrivial band-crossing nodal points (NPs) due to the touching of conduction and valence bands in momentum space (MS) [119]. According to the degeneracy and distribution of the NPs, TSMs can be generally classified as Dirac semimetals (DSMs) [120] and Weyl semimetals (WSMs) [121], where the NPs are discretely distributed in MS with four-fold and two-fold degeneracy, respectively. A special case of DSMs is nodal line semimetals (NLSMs) where the NPs form one-dimensional nodal line in MS and have flexible topological configurations in MS such as nodal ring, nodal chain and nodal nets [122, 123, 124]. NLSMs have recently attracted a great deal of attention due to their distinct drumhead-like surface flat bands and compatibility with other nontrivial fermions [125]. Such unique properties endow NLSMs many exotic properties such as high-temperature surface superconductivity, non-dispersive Landau energy level and specific long-range Coulomb interactions, promising its potential applications in future low-dissipation electronic and spintronic devices [126, 127, 128]

The study of degeneracies between energy bands in the spectrum of a system dates back to the early days of quantum mechanics [129]. Since then, band degeneracies are featured in various physical phenomena, from signaling quantum phase transitions [130] to being the spectral signature of a semimetal [131, 132]. According to the non-crossing rule by von Neumann and Wigner [129], energy bands generally avoid each other, but symmetries entail the possibility of band crossings. A band crossing is *symmetry-enforced* if its existence is guaranteed by the underlying symmetry(ies) alone, and *accidental* if the band crossing requires also tuning parameters of the material (e.g.

the hopping energy, or any other microscopic parameter of the material). A special case occurs in three dimensions where the availability of sufficiently many tunable parameters (three momentum coordinates and one material parameter) leads to accidental band crossings even in the absence of symmetries [131]. Symmetry-enforced band crossings arise from nonsymmorphic symmetries (point group transformations followed by a non-primitive translation), as first realized by Michel and Zak in 1999 [133], and later applied to the research on TSMs [134, 135, 136].

The nontrivial topology of band crossings in TSMs underpins a variety of phenomena, e.g. Fermi arcs [137] and chiral anomaly [138], and promise diverse technological applications, notably in topological quantum computing [132] and in quantum-device designs based on proximity effects [139]. TSMs with accidental band crossings are topologically protected only locally, being eventually destroyed by perturbations. In contrast, TSMs with symmetry-enforced band crossings are endowed with global topological protection, i.e. they are immune to symmetry-preserving perturbations [134, 135].

Here we focus our attention on NLSMs, the TSMs with band crossings occurring along lines in the Brillouin zone (BZ). Two-dimensional (2D) structures, e.g. hexagonal lattices [140] and honeycomb-Kagome lattices [141], and PbFCl-type structures [142], have been predicted to realize NLSMs. However, the frailty to perturbations, particularly to spin-orbit coupling (SOC), of the resulting accidental nodal lines (NLs) hinders possible applications and use of proximity effects [139]. Symmetry-enforced NLSMs are the natural candidates to overcome this challenge. Predicted realizations comprise 3D materials from hexagonal groups $P\bar{6}2c$, $P6_122$, and $P6_3/m$ [143], and group $P4/nmm$ [144]. A recent review gathers the most recent developments in the quest for 3D NLSMs [145].

As an alternative to naturally nonsymmorphic 3D crystals, we propose to engineer 2D symmetry-enforced NLSMs by turning symmorphic monoatomic sheets into nonsymmorphic ones through removing atoms. Quite surprisingly, besides symmetry-enforced NLs, vacancy-engineered materials exhibit also accidental NLs which survive under very strong SOC, with strength even exceeding the experimentally attainable values. These additional NLs were first noted in our previous report [146] where their robustness was conjectured to be symmetry enforced since accidental NLs had so far been known to be easily destroyed by perturbations. However, symmetry-enforced NLs are pinned at high-symmetry momenta in the Brillouin zone, whereas their accidental counterparts can be moved around by varying the parameters of the material inside the regime, however small, in which they exist. Our movable, and yet unusually robust, NLs do not fit in either category. We thus uncover that the usual approach to distinguish NLs by their response to perturbations is inadequate when such band crossings appear simultaneously in the spectrum and have a common origin.

In this work, we develop a complete theoretical description of a 2D vacancy-engineered nonsymmorphic lattice which resolves the puzzle by demonstrating that, despite their unusual robustness, the NLs which are movable in the interior of the BZ are accidental, and that symmetry-enforced NLs also exist, but are pinned at an edge of the BZ. While the accidental NLs are not directly wielded by the nonsymmorphic symmetry *per se*, they are a direct consequence of the proposed

mechanism of attaining nonsymmorphicity out of vacancies. The fact that these accidental NLs can move and change shape inside the BZ might enable manipulation of momentum-dependent scattering processes and, hence, of various responses of the material.

Our analysis based on a 2D four-band effective model adds to the known proofs of band-degeneracy enforcement for a 1D two-band model [134, 135] and for a 2D two-band model [136]. It is well-known that a glide-plane symmetry enforces band degeneracies at the glide-invariant boundary of the BZ. But whether this band degeneracy is a nodal point or a NL is not guaranteed by the glide-plane symmetry. In Refs. [134, 135, 136] the nonsymmorphic symmetry yields nodal points located at BZ corners. In contrast, our formalism is specifically focused on symmetry-enforced NLs along an edge of a 2D BZ. This fundamental difference is connected to the roles played by inversion and time-reversal symmetries in the effective models, which depend on dimensionality and number of bands. The NLs uncovered here are to be contrasted also with those predicted for 3D nonsymmorphic materials [143, 144]. Symmetry-enforced NLs in 2D thus constitute a new case of band-degeneracy enforcement. The proposed mechanism of engineering nonsymmorphic 2D lattices from periodic configurations of vacancies offers an alternative path to fundamental investigations and materials design of NLSMs.

3.2   Computational Details

The band structures of borophene are obtained by first-principles calculations using the QUANTUM ESPRESSO package [147]. The kinetic energies cutoff for wave function (ecutwfc) and for charge density (ecutrho) are set to 600 and 60 Ry, respectively. Perdew, Burke and Ernzerhof (PBE) form of the generalized gradient approximation (GGA) is adopted for the exchange-correlation energy [76]. Numerical integrations in the Brillouin zone are evaluated with the Monkhorst-Pack mesh of $10 \times 10 \times 1$. All structures are relaxed until the total energy converges to within 10^{-4} eV during the self-consistent loop, employing the Methfessele-Paxton method with a smearing of 0.2 eV width.

To incorporate Rashba SOC, we develop a tight-binding (TB) model using the package Wannier90 [148]. This maps the ground-state wave functions from the density functional theory output file onto a maximally localized Wannier function basis $\{|W_{i\vec{R}}\rangle\}$, where $i = (I, \alpha)$ is the composite index accounting for the atom site $\vec{r}_I$ and the atomic orbital α. $\vec{R} = R_a\vec{a} + R_b\vec{b}$ is the Bravais lattice vector with $R_{a/b}$ being the Bravais lattice vector component on the direction of the unit cell lattice vector $\vec{a}/\vec{b}$. The wave function is thus given by

$$|\phi_{i\vec{k}}\rangle = \frac{1}{\sqrt{N}} \sum_{\vec{R}} e^{i\vec{k}\cdot\vec{R}}|W_{i\vec{R}}\rangle. \tag{3.1}$$

We employ an adaptive k-mesh strategy to build the TB Hamiltonian, H_{TB}, of borophene B_n without Rashba SOC. The entries of H_{TB} are given by

$$[H_{TB}(\vec{k})]_{ij} = \langle\phi_{i\vec{k}}|H_{TB}|\phi_{j\vec{k}}\rangle = \sum_{\vec{R}} e^{i\vec{k}\cdot\vec{R}} t_{ij}(\vec{R}), \tag{3.2}$$

where $t_{ij}(\vec{R}) = \langle W_{i0}|H_{KS}|W_{j\vec{R}}\rangle$ is the matrix element extracted from the Wannier90 output file, with H_{KS} being the Hamiltonian of Kohn-Sham equation.

An out-of-plane magnetic exchange field breaks time-reversal symmetry (TRS). Depending on the spin states, their energy bands shift upward or downward along the energy axis. Since the penetration depth of the magnetic proximity effect is governed by short-range exchange interactions, it becomes more pronounced in two-dimensional heterostructures. Unlike conventional approaches for breaking TRS by doping with transition metal atoms or shifting the positions of some atoms, magnetic proximity effect induced by a ferromagnetic substrate provides a versatile method to introduce magnetism and spin-dependent properties in nonmagnetic regions, without stringent requirements on the sample growth. Besides TRS, a ferromagnetic substrate beneath the sample breaks also inversion symmetry along the direction perpendicular to the sample. This yields a Rashba SOC which shifts the energy bands oppositely along a direction in the $k_x - k_y$ plane.

Generically, borophene deposited on a ferromagnetic substrate is described by the following Hamiltonian

$$H = H_{TB} + H_{EX} + H_{SOC}, \tag{3.3}$$

where H_{TB} is the TB Hamiltonian of the free-standing B_n, H_{EX} and H_{SOC} are the magnetic exchange and the Rashba SOC Hamiltonians, respectively, induced by proximity effect of the substrate.

H_{EX} contains spin and orbital exchange [149], $H_{EX} = H_{s-EX} + H_{o-EX}$. The former is determined by

$$H_{s-EX} = J_s \sum_{i,l,s,s'} C_{i,l,s}^+ [\mathbf{M} \cdot \sigma]_{s,s'} C_{i,l,s'}, \tag{3.4}$$

where J_s is the spin-exchange coupling strength, $C_{i,l,s}^+$ ($C_{i,l,s}$) is the creation (annihilation) operator of an electron with spin s and orbital quantum number l at the site i, while $\mathbf{M}$ is the magnetization direction and σ is the vector of Pauli matrices, with $[\mathbf{M} \cdot \sigma]_{s,s'} = [M_x \cdot \sigma_x + M_y \cdot \sigma_y + M_z \sigma_z]_{s,s'}$.

For an out-of-plane exchange field, $M_x = M_y = 0$ and $M_z = M$. In the basis of the atomic orbitals (s, p_x, p_y, p_z) and spin $(\uparrow, \downarrow)$, the matrix elements of H_{s-EX} are given in Table 3.1.

	$|s\uparrow\rangle$	$|p_x\uparrow\rangle$	$|p_y\uparrow\rangle$	$|p_z\uparrow\rangle$	$|s\downarrow\rangle$	$|p_x\downarrow\rangle$	$|p_y\downarrow\rangle$	$|p_z\downarrow\rangle$
$\langle s\uparrow|$	$J_s \cdot M$	0	0	0	0	0	0	0
$\langle p_x\uparrow|$	0	$J_s \cdot M$	0	0	0	0	0	0
$\langle p_y\uparrow|$	0	0	$J_s \cdot M$	0	0	0	0	0
$\langle p_z\uparrow|$	0	0	0	$J_s \cdot M$	0	0	0	0
$\langle s\downarrow|$	0	0	0	0	$J_s \cdot M$	0	0	0
$\langle p_x\downarrow|$	0	0	0	0	0	$J_s \cdot M$	0	0
$\langle p_y\downarrow|$	0	0	0	0	0	0	$J_s \cdot M$	0
$\langle p_z\downarrow|$	0	0	0	0	0	0	0	$J_s \cdot M$

Table 3.1: Matrix elements of the spin-exchange coupling H_{s-EX}.

The orbital exchange contribution is given by

$$H_{o-EX} = J_o \sum_{i,l,l',s,} C_{i,l,s}^+ [\mathbf{M} \cdot L]_{l,l'} C_{i,l',s}, \tag{3.5}$$

where J_o is the orbital-exchange coupling strength and L is a compact notation comprising of angular momentum orbital l and magnetic quantum number m, i.e., $L = (l, m)$, with $[\mathbf{M} \cdot L]_{l,l'} = [M_x \cdot L_x + M_y \cdot L_y + M_z \cdot L_z]_{l,l'}$, and $\langle l, m \mid L_z \mid l', m' \rangle = m\delta_{l,l'}\delta_{m,m'}$. The elements of H_{o-EX} for orbitals (s, p_x, p_y, p_z) and spin $(\uparrow, \downarrow)$ are shown in Table 3.2. In our calculations, we set $\mathbf{M}=1$ and $J_s = J_o = J$, with J being the exchange coupling strength used in Fig. 2 of the main text.

	$|s \uparrow\rangle$	$|p_x \uparrow\rangle$	$|p_y \uparrow\rangle$	$|p_z \uparrow\rangle$	$|s \downarrow\rangle$	$|p_x \downarrow\rangle$	$|p_y \downarrow\rangle$	$|p_z \downarrow\rangle$
$\langle s \uparrow|$	0	0	0	0	0	0	0	0
$\langle p_x \uparrow|$	0	0	$iJ_o \cdot M$	0	0	0	0	0
$\langle p_y \uparrow|$	0	$-iJ_o \cdot M$	0	0	0	0	0	0
$\langle p_z \uparrow|$	0	0	0	0	0	0	0	0
$\langle s \downarrow|$	0	0	0	0	0	0	0	0
$\langle p_x \downarrow|$	0	0	0	0	0	0	$iJ_o \cdot M$	0
$\langle p_y \downarrow|$	0	0	0	0	0	$-iJ_o \cdot M$	0	0
$\langle p_z \downarrow|$	0	0	0	0	0	0	0	0

Table 3.2: Matrix elements of the orbital-exchange coupling H_{o-ex}.

The Rashba SOC is expressed as

$$H_{SOC} = i \sum_n \lambda_n \sum_{\langle i,j \rangle} C_i^+ [\sigma \times \mathbf{d}_{i,j}^n] C_j, \tag{3.6}$$

where $\mathbf{d}_{i,j}^n = \mathbf{r}_i - \mathbf{r}_j$ is the distance connecting a pair of the n-th nearest neighbor sites i and j in the lattice with λ_n the SOC coupling strength, C_i^+ (C_i) is the creation (annihilation) operator of an electron at site i. We only use nearest-neighbors in the calculation, hence the Rashba SOC coupling strength is given by λ. Here we simply replace the Hamiltonian with a set of momenta (k_x, k_y) by $(k_y, -k_x)$, then Eq. (3.6) becomes

$$H_{SOC} = i\lambda \sum_{\langle i,j \rangle} C_i^+ [\sigma \cdot \mathbf{d}_{i,j}] C_j. \tag{3.7}$$

The expression $[\sigma \cdot \mathbf{d}_{i,j}]$ evaluated for nearest-neighbor sites is shown in Fig. 3.1.
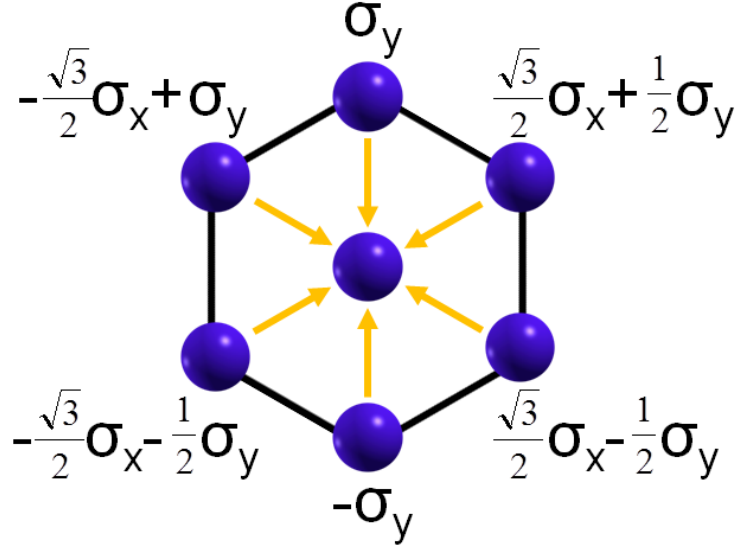
Figure 3.1: The expression $[\sigma \cdot \mathbf{d}_{i,j}]$ in the Rashba SOC Hamiltonian H_{SOC} for nearest-neighbor sites.

3.3 Nodal Lines in Borophenes with Nonsymmorphic Symmetry

NLSMs have been reported in monolayer hexagonal lattices [140], honeycomb-kagome lattices [141] and monolayer transition metal-group VI compounds [150]. However, the fragility to perturbations of the nodal lines in these materials is a severe constraint to their stability, let alone amenability to external manipulations. The realization of a robust NLSM has so far been a daunting challenge. Owing to their global stability, NLSMs protected by nonsymmorphic symmetries have thus attracted a lot of attention. Here we report on a surprisingly simple way to obtain such a phase of matter, namely, by removing atoms from a two-dimensional (2D) symmorphic material, turning it into a nonsymmorphic one. This yet unexplored possibility is illustrated in Fig. 3.2, with free-standing borophene (B_2) transformed into a β-borophene [151, 152, 153, 154, 155, 156] (B_{10}). This 2D material of borophene family can be prepared by physical and chemical routes in many reports. Especially B_{10} which we use here was reported to be synthesized by growing epitaxially on a Ag(111) substrate in Wu's team [154], where all products exhibit a triangular lattice but with different arrangements of periodic holes, leading to borophenes with symmorphic or nonsymmorphic symmetry. Figure 3.2(a) shows B_2, a 2D honeycomb-like boron lattice which is invariant under reflections R_1 and R_2, and inversion I. These symmorphic symmetries lead to an accidental Dirac cone gapped by perturbations, akin to those in graphene, silicene and germanene. Figure 3.2(b) shows B_{10} obtained by introducing vacancies at the center of selected hexagons of B_2, thus producing hollow hexagons, along the armchair direction. As a result, R_2 is replaced by a nonsymmorphic glide plane G, and the Dirac cone gives place to a nodal line (NL) which is robust against perturbations.
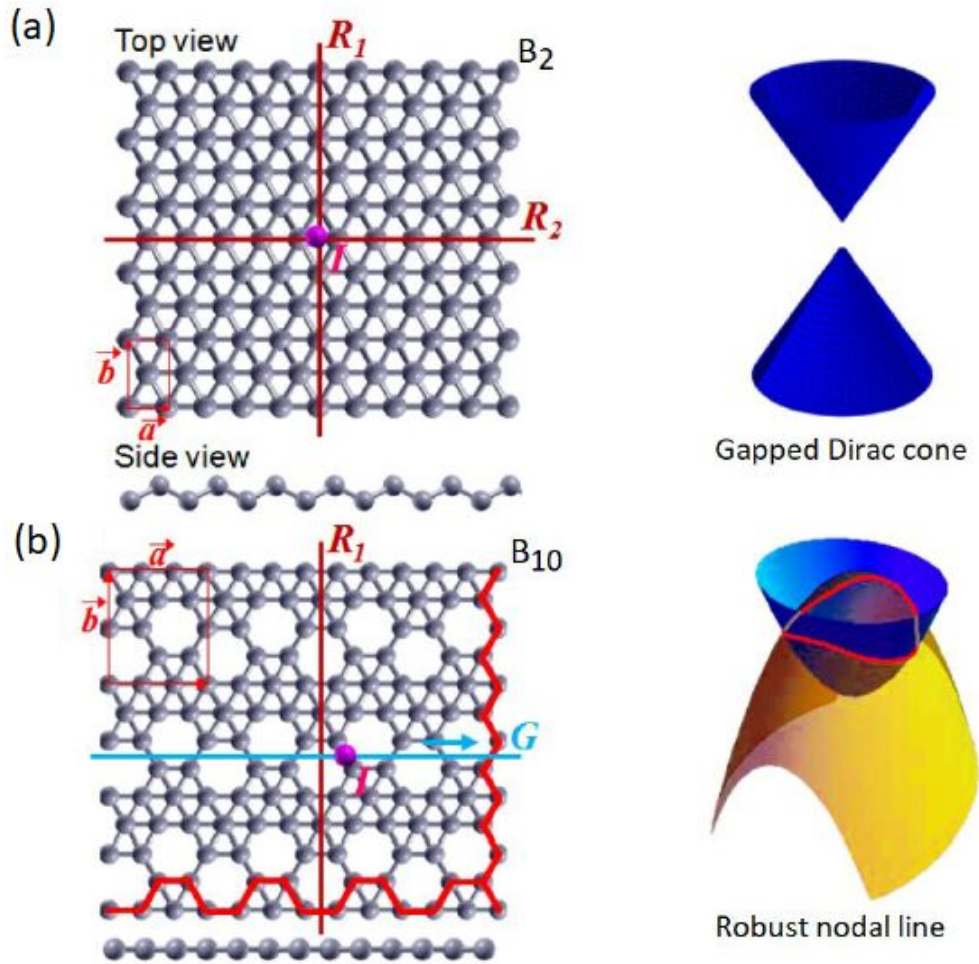
Figure 3.2: (a) Buckled lattice structure of pristine borophene, B_2, with two atoms in the unit cell defined by $\vec{a}$ and $\vec{b}$. The lattice has symmorphic symmetries: reflection planes R_1 and R_2, and an inversion point I. The accidental Dirac cone of B_2 is gapped by perturbations. (b) Planar lattice structure of a $\beta-$borophene, B_{10}, which has ten atoms in the unit cell. The red lines represent armchair and zigzag directions. Hollow hexagons are distributed, one per filled hexagon, along the armchair direction. Reflection plane R_2 of B_2 is replaced by a nonsymmorphic glide plane G composed of a reflection plane and a nonprimitive translation by $\vec{a}/2$. The nodal line of B_{10} is robust against perturbations.

The upper panels of Fig. 3.3 are contour plots on the $k_x - k_y$ plane showing how band crossings of free-standing B_{10} [Fig. 3.3(a)] change under Rashba spin-orbit coupling (SOC) [Fig. 3.3(b)] and under magnetic exchange [Fig. 3.3(c)]. The contour plots convey that the band crossings are NLs and these NLs are robust to strong Rashba SOC and magnetic exchange. For instance, the magnetic proximity effect intensity $J = 0.1$ eV in Fig. 3.3(c) exceeds five times the largest value measured in 2D materials [157]. In the lower panel of Fig. 3.3(a) its inset shows a cut through the NLs marked with blue and red circles from the upper panel. The cut is along the X-V direction in the Brillouin zone (BZ) [shown in the upper panel of Fig. 3.3(b)]. The blue-encircled band crossing in the inset, corresponding to the inner NL, is zoomed out in the panel. The crossing bands are spin-degenerate, with up and down spins measured with respect to an axis which, for

free-standing B_{10}, we choose as the direction perpendicular to the sample (z). The lower panels of Fig. 3.3(b)-(c) show that either Rashba SOC or magnetic exchange lifts this degeneracy. Rashba SOC rotates the spin quantization axis to lie in the plane of the sample and then shifts the up and down (with respect to this new axis) bands towards opposite directions along the X-V path. The magnetic exchange field, from the substrate's out-of-plane anisotropy, keeps the quantization axis along z and splits the up and down bands along the energy axis. The color of the bands represent their spin content: blue/red in (c) stands for spin down/up with respect to z, green in (b) represents a mix of up and down spins with respect to z, and purple in (a) indicates the spin-degeneracy of those bands.
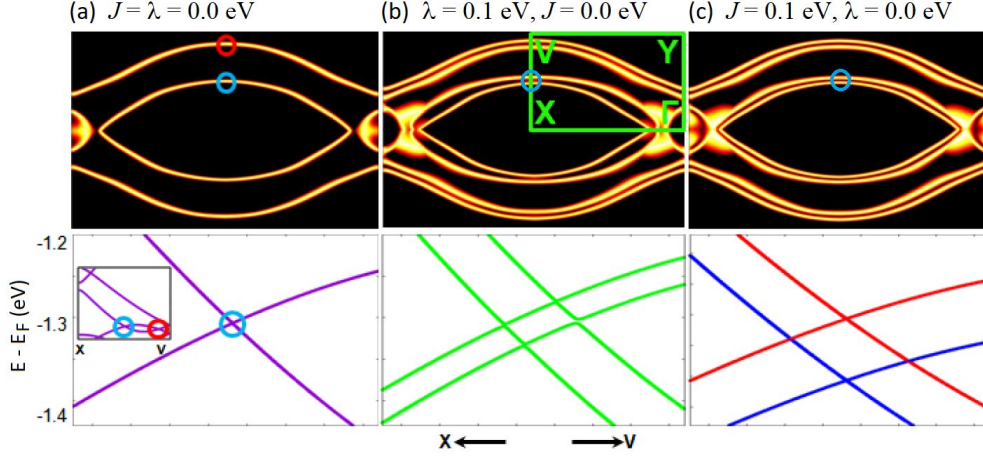
Figure 3.3: Upper panels: Contour plots on the $k_x - k_y$ plane of band crossings of B_{10} (a) in the absence of proximity-effects, (b) subject to Rashba SOC, (c) subject to magnetic exchange. The band crossings are NLs and these NLs are robust against both Rashba SOC and magnetic exchange. Lower panels: (a)-(c) Cut through the nodal line marked with the blue circle in the corresponding upper panel. The cut is along the X-V direction in the Brillouin zone. The inset in lower panel (a) shows the cut through two nodal lines, the blue- and red-marked ones in the upper panel. The bands in (a) are spin-degenerate and this degeneracy is lifted by Rashba SOC in (b) and by magnetic exchange in (c). The colors of the bands indicate spin projection along the axis perpendicular to the sample: blue (red) in (c) stands for spin down (up), green in (b) represents mixed spin states, and purple in (a) indicates the spin-degeneracy of those bands.

The robustness of NLs in B_{10} is consistent with a global topological protection. This is in stark contrast to the Dirac cones of symmorphic B_2 which are gapped by either Rashba SOC or magnetic exchange, as illustrated in Fig. 3.2(a) and numerically confirmed. Below we prove that the origin of this protection is the presence of the nonsymmorphic glide-plane symmetry. Interestingly, the robust NLs are not unique to B_{10}. Changing the concentration of hollow hexagons by specific amounts generates a set of $\beta-$borophenes with the same glide-plane symmetry as B_{10} and, hence, with robust NLs. The concentrations of hollow hexagons in the investigated $\beta-$borophenes are within the stability range obtained in recent reports [158].

3.4 Effective Model and Symmetry Analysis

To better understand the origin of the nodal lines found in B_10, we perform a symmetry analysis of an effective model. The standard proof of band crossing from a nonsymmorphic symmetry which employs a 1D two-band effective model [159] is not applicable in the present case. The minimal lattice representation of B_{10} has four internal degrees of freedom and hence it requires a 2D four-band effective Hamiltonian. The proposed model and symmetry analysis are detailed in the Supporting Information. The minimal representation of B_{10} is shown in Fig. 3.4(a), along with the relevant crystal symmetries, i.e., glide plane G, inversion I, and reflection R. Because G, I, and R are shifted from the unit-cell center, their matrix representations are momentum-dependent: G and I on k_y and R on k_x. Due to the non-primitive translation along x, G is dependent also on k_x. As we shall see, these dependencies impose strong constraints on the band structure of the system.
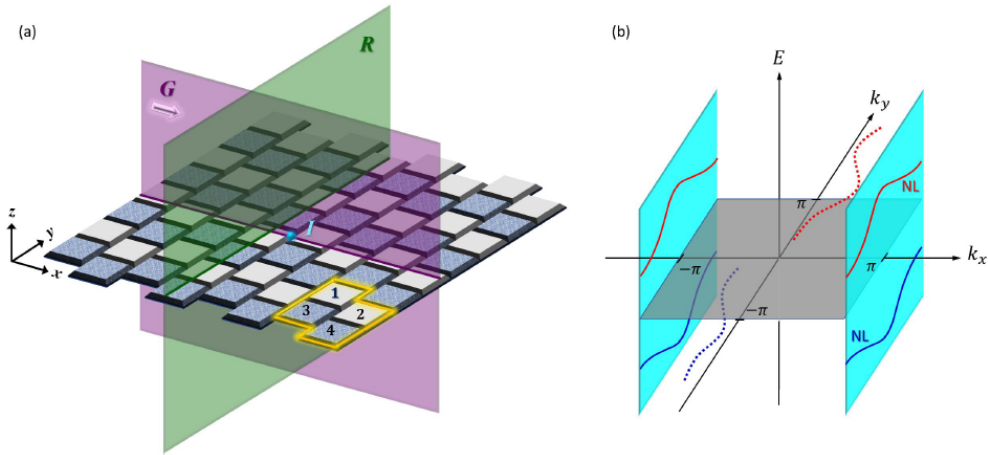
Figure 3.4: (a) Minimal lattice for B_{10} depicted in Fig. 1(b). White (blue) squares represent the hollow (filled) hexagons. The distribution of the squares yields an armchair profile along the x-direction. The primitive unit cell is delimited by yellow lines. The lattice possesses a nonsymmorphic glide-plane symmetry G composed of a reflection about a plane parallel to the armchair direction, followed by a nonprimitive translation of half-length of the unit cell parallel to the glide-plane. The lattice has two symmorphic symmetries: an inversion-point, I, on the line where the plane of G cuts through the lattice, and a reflection-plane, R, perpendicular to the plane of G. (b) The NLs of the lattice in (a) are protected by G, while I sets their location at $k_x = \pm\pi$. Breaking I releases the NLs, as illustrated by the dotted curves. The straight NLs at $k_x = \pm\pi$ of the minimal lattice differ in shape from the NLs of B_{10} (which also has G and I symmetries) shown on the upper panels of Fig. 2(a)-(c). The actual G and I operators relate the 80 intracell degrees of freedom of B_{10} in a more complicated way than the effective ones relating the 4 intracell degrees of freedom of the minimal lattice, resulting in NLs with more complicated shapes on the $k_x - k_y$ plane.

A generic tight-binding Hamiltonian for the minimal lattice of Fig. 3(a) can be written as:

$$H_{\text{eff}} = \sum_{m_x,m_y=1}^{N_x,N_y} \sum_{j,j'=1}^{4} [t_{jj'}\, c_{m_x,m_y}^{j\,\dagger} c_{m_x,m_y}^{j'} + u_{jj'}\, c_{m_x,m_y}^{j\,\dagger} c_{m_x+1,m_y}^{j'} + v_{jj'}\, c_{m_x,m_y}^{j\,\dagger} c_{m_x,m_y+1}^{j'} + H.c.],$$

(3.8)

where $c_{m_x,m_y}^{j\,\dagger}$ (c_{m_x,m_y}^{j}) creates (annihilates) a fermion at the j-th square of the unit cell located at (m_x, m_y). In Eq. (3.8), $t_{jj'}$ is the hopping energy from square j' to j within the same unit cell, with $t_{jj} = \mu_j$ an "on-square" energy, $u_{jj'}$ ($v_{jj'}$) is the hopping energy from square j' to j between neighboring unit cells along the x-direction (y-direction).

Imposing periodic boundary conditions, we make a Fourier transform that $c_{m_x,m_y}^{j} = \sum_{k_x,k_y} c_{k_x,k_y}^{j} e^{i(k_x m_x + k_y m_y)}$, with $k_{x,y} = 2\pi n/N_{x,y}$, $n = 0, \pm 1, ..., \pm N_{x,y}/2$, and get

$$H_{\text{eff}} = \sum_{k_x,k_y} \sum_{j,j'=1}^{4} c_{k_x,k_y}^{j\,\dagger}\, \varepsilon_{j,j'}(k_x, k_y)\, c_{k_x,k_y}^{j'},$$

(3.9)

with

$$\varepsilon_{j,j'}(k_x, k_y) = t_{jj'} + t_{j'j}^{*} + u_{jj'} e^{ik_x} + u_{j'j}^{*} e^{-ik_x} + v_{jj'} e^{ik_y} + v_{j'j}^{*} e^{-ik_y}.$$

(3.10)

The above is a generic expression for the coefficients $\varepsilon_{j,j'}$. Considering hopping only between neighboring squares, the only non-vanishing intercell hopping amplitudes in Eq. (3.25) are $u_{21} = t_{21}$, $u_{23} = t_{23}$, $u_{41} = t_{41}$, $u_{43} = t_{43}$ along x, and $v_{13} = t_{13}$, $v_{14} = t_{14}$, $v_{23} = t_{23}$, $v_{24} = t_{24}$ along y (c.f. Fig. 3(a)).

Finally, Eq. (3.9) can be written in matrix form as

$$H_{\text{eff}} = \sum_{k_x,k_y} c_{k_x,k_y}^{\dagger}\, \mathcal{H}(k_x, k_y)\, c_{k_x,k_y},$$

(3.11)

where $c_{k_x,k_y}^{\dagger} = (c_{k_x,k_y}^{1\,\dagger}, ..., c_{k_x,k_y}^{4\,\dagger})$ is a row spinor containing the creation operators at each one of the four intracell squares, c_{k_x,k_y} is the transpose conjugate spinor, and $\mathcal{H}(k_x, k_y)$ is the 4×4 Bloch matrix whose entries are given in Eq. (3.25).

The symmetries of the lattice depicted in Fig. 3(a) are described by the unitary transformations $G = \mathcal{G}(k_x, k_y)\,\Updownarrow_{k_y}$, $I = \mathcal{I}(k_y)\,\Updownarrow_{k_x,k_y}$, $R = \mathcal{R}(k_x)\,\Updownarrow_{k_x}$, where $\Updownarrow_{k_{x,y}}$ inverts $k_{x,y}$ and

$$\mathcal{G}(k_x, k_y) = \begin{bmatrix} e^{ik_y} g(k_x) & 0 \\ 0 & g(k_x) \end{bmatrix}, \quad g(k_x) = \begin{bmatrix} 0 & 1 \\ e^{ik_x} & 0 \end{bmatrix},$$

(3.12)

$$\mathcal{I}(k_y) = \begin{bmatrix} e^{ik_y} \sigma_x & 0 \\ 0 & \sigma_x \end{bmatrix}, \quad \sigma_x = \begin{bmatrix} 0 & 1 \\ 1 & 0 \end{bmatrix},$$

(3.13)

$$\mathcal{R}(k_x) = \mathcal{G}(k_x, k_y)\mathcal{I}(-k_y).$$

(3.14)

Imposing G on H_{eff} yields the "glide-plane constraints" on the entries of $\mathcal{H}(k_x, k_y)$:

$$\varepsilon_{i+1,i+1} = \varepsilon_{i,i}, \quad i = 1, 3,$$

(3.15)

$$\varepsilon_{i,i+1}^{*}(k_x, k_y) = e^{ik_x}\, \varepsilon_{i,i+1}(k_x, -k_y), \quad i = 1, 3,$$

(3.16)

$$\varepsilon_{2,3}(k_x, k_y) = e^{i(k_x+k_y)}\, \varepsilon_{1,4}(k_x, -k_y),$$

(3.17)

$$\varepsilon_{2,4}(k_x, k_y) = e^{ik_y}\, \varepsilon_{1,3}(k_x, -k_y).$$

(3.18)

Equations (3.16)-(3.17) have the general form $p(k) = e^{ik}q(k)$ on the k_x-momentum. A topological argument yields that $q(\bar{k}) = 0$ at some $\bar{k} \in [-\pi, \pi]$. This implies that the glide-plane symmetry forces the entries constrained by Eqs. (3.16)-(3.17) to vanish somewhere in the BZ. To find where, we impose I on H_{eff} to get the "inversion-point constraints" on the off-diagonal entries of $\mathcal{H}(k_x, k_y)$:

$$\varepsilon_{i,i+1}^*(k_x, k_y) = \varepsilon_{i,i+1}(-k_x, -k_y), \quad i = 1, 3, \tag{3.19}$$

$$\varepsilon_{2,3}(k_x, k_y) = e^{ik_y}\varepsilon_{1,4}(-k_x, -k_y), \tag{3.20}$$

$$\varepsilon_{2,4}(k_x, k_y) = e^{ik_y}\varepsilon_{1,3}(-k_x, -k_y). \tag{3.21}$$

By applying Eqs. (3.15)-(3.21) to the entries of the Bloch matrix as given by Eq. (3.25) (and considering hopping only between neighboring squares) we arrive at the effective 4×4 model of B_{10}:

$$\begin{bmatrix} 2\mu_1 & t_{21}(1 + e^{-ik_x}) & t_{31}^* + t_{13}(1 + e^{ik_y}) & 0 \\ t_{21}^*(1 + e^{ik_x}) & 2\mu_1 & 0 & t_{31}^* e^{ik_y} + t_{13}(1 + e^{ik_y}) \\ t_{31} + t_{13}^*(1 + e^{-ik_y}) & 0 & 2\mu_3 & t_{43}(1 + e^{-ik_x}) \\ 0 & t_{31}e^{-ik_y} + t_{13}^*(1 + e^{-ik_y}) & t_{43}^*(1 + e^{ik_x}) & 2\mu_3 \end{bmatrix}. \tag{3.22}$$

We thus see that the combination of G and I symmetries makes entries $\varepsilon_{1,2}$ and $\varepsilon_{3,4}$ vanish at $k_x = \pm\pi$, while entries $\varepsilon_{1,4}$ and $\varepsilon_{2,3}$ vanish everywhere.

When $k_x = \pm\pi$, the characteristic equation $det[\mathcal{H}(\pm\pi, k_y) - E\mathbb{1}] = 0$ can be analytically solved, yielding the four eigenenergies $E_{1,2/3,4}(\pm\pi, k_y) = E_{+/-}(\pm\pi, k_y)$, where

$$E_\pm(\pm\pi, k_y) = \sigma \pm \sqrt{\delta^2 + |t|^2(5 + 4\cos k_y)}, \tag{3.23}$$

with $\sigma = \mu_1 + \mu_3$, $\delta = \mu_1 - \mu_3$, and $t = t_{13} = t_{31}^*$.

We conclude that the four bands become pairwise degenerate, forming two NLs at $k_x = \pm\pi$ described by Eq. (3.23). These NLs are illustrated in Fig. 3(b). The existence of a pair of NLs follows G alone; the role of I is to pin the NLs at $k_x = \pm\pi$. Breaking I releases the NLs which become free to move and change shape through the BZ as "glide-preserving" perturbations are introduced in H_{eff}. This is illustrated by the dotted lines in Fig. 3(b).

Now, the intracell degrees of freedom of B_{10} in Fig. 1(b) far exceed the four squares forming the unit cell of the minimal lattice in Fig. 3(a). The actual number of intracell degrees of freedom is given by 10 atomic positions × 4 orbitals per atom × 2 spin orientations per orbital. As a result, the 4×4 effective matrices from Eqs. (A-1.6) and (A-2.1) are replaced by 80×80 matrices. Despite this huge increase, the actual glide-plane constraints on the off-diagonal entries of the 80×80 Bloch matrix will keep the same general structure in k_x and k_y as in Eqs. (3.16)-(3.18). This is because k_x and k_y are external degrees of freedom related only to the location of the whole unit cell, i.e. unrelated to intracell degrees of freedom. In other words, that the glide-plane forces the off-diagonal entries of the Bloch matrix to vanish somewhere in the BZ is independent of intracell structure. However, the actual glide-plane and inversion symmetry constraints relate the 80 intracell indexes in some complicated way. As a result, the actual NLs traced out on the BZ have more complicated shapes [c.f. Figs. 2(a)-(c)] than the NLs of the minimal lattice [c.f. Fig. 3(b)].

The topological nature of the NLs of B_{10} follows from non-spatial symmetries. Free-standing B_{10} possesses time-reversal symmetry, but lacks chiral and particle-hole symmetries. It thus belongs to symmetry class AII of the Altland-Zirnbauer classification [160]. Time-reversal symmetry is broken in B_{10} on a ferromagnetic substrate, changing the symmetry class from AII to A [160]. The topological classification of band crossings [159] thus yields that free-standing and deposited B_{10} are endowed with a topological invariant given by the winding of the eigenvalue of the glide plane operator as the Brillouin zone is swiped [159]. The only way to make this winding trivial is by breaking the glide-plane symmetry. We conclude that the robust topological NLs of B_{10} are globally stable.

We numerically demonstrate that certain β-borophenes host nodal lines (NLs) which are robust against perturbations. We prove through a symmetry analysis of an effective 2D four-band model that the NLs are protected by a nonsymmorphic glide plane symmetry, hence their robustness. Our choice of borophene as a case study was motivated by the multi-center characteristics of B-B bonding which results in vacancy-mediated structural motifs, with a plethora of polymorphs. Besides, borophene possesses unique properties, including mechanical flexibility, transparency, and superconductivity, making a NLSM-realization an enticing achievement. Tuning the material towards topological superconductivity - either by enhancing the inherent superconductivity of borophene or by proximity effect [161] - would be a very interesting path to follow. This could expand ongoing efforts to realize Majorana states in 2D [162, 163, 164] which, unlike their 1D counterparts [165], can simplify probing their non-Abelian statistics through fusion or braiding, crucial for topological quantum computing. Nonetheless, being based on crystal symmetries only, our proposal does not rely on chemical composition or microscopic details of the sample; it is applicable to materials other than borophene. For example, it has recently been proven that crystalline symmetries can stabilize NLs with quadratic and cubic dispersion in a wealth of symmetry groups [166]. Combing this finding with ours could lead to symmetry-protected higher-order NLs. The concept of engineering a nonsymmorphic symmetry simply by introducing vacancies in a symmorphic crystal therefore opens an unexplored path in the quest of material realizations of nodal-line semimetals and their technological applications.

3.5 Symmetry-enforced band degeneracies of a nonsymmorphic two-dimensional lattice

In this section we carry out a symmetry analysis of a minimal lattice which captures the symmetries of B_{10} and B_{16} shown in Figures 3.5(a)-(b). Fig. 3.5(c) depicts a 2D lattice whose unit cell has four internal degrees of freedom, represented by the magenta and blue disks which are shifted along the m_y-direction. This shift mimics the profile of the filled and hollowed stripes in B_{10} and B_{16}. The minimal lattice is invariant under a nonsymmorphic glide plane G, a symmorphic reflection plane R, and a symmorphic inversion point I. We now analyze how these symmetries constrain the band structure of the 4×4 Bloch Hamiltonian, $\mathcal{H}(k_x, k_y)$, of the lattice depicted in Fig. 3.5(d). This analysis is sample-independent; it relies only on the symmetries of the minimal lattice shown in Fig. 3.5(c).
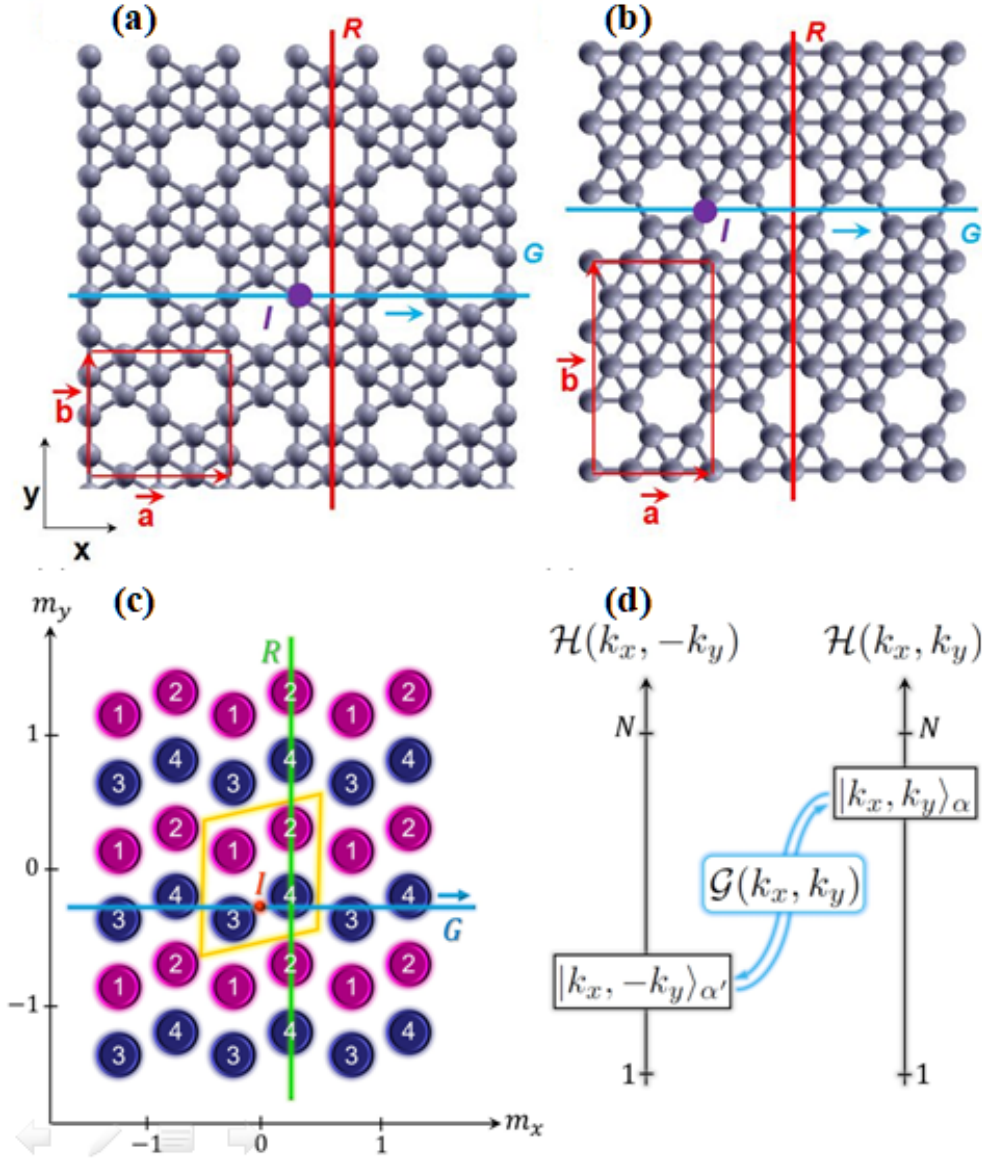
Figure 3.5: Lattice structure of borophene B_{10} (a) and B_{16} (b) with ten and sixteen atoms, respectively, in the unit cell defined by primitive vectors $\vec{a}$ and $\vec{b}$. B_{10} [B_{16}] is obtained from pristine borophene by removing boron atoms from the center of hexagons which share one corner [side] along the x-direction. In both panels (a) and (b), the hollow hexagons form a string along the x-direction, with a zigzag profile in the y-direction. This basic feature yields a nonsymmorphic glide-plane symmetry G (composed of a reflection plane running along the x-direction and a non-primitive translation by $\vec{a}/2$), a symmorphic reflection-plane symmetry R perpendicular to G, and a symmorphic inversion-point symmetry I. (c) A minimal nonsymmorphic two-dimensional lattice, with the unit cell delineated by the yellow lines. The location of the unit cell is defined by (m_x, m_y). The disks numbered from 1 to 4 represent two types of structures within the unit cell. In real borophenes B_{10} and B_{16} shown in (a) and (b), these structures are the hollow and filled pieces that make up the unit cell of those materials. The minimal lattice has the following spatial symmetries: a nonsymmorphic glide plane, G, composed of a reflection about the m_x-direction, followed by a nonprimitive translation by half of the length of the unit cell along the m_x-direction, a symmorphic reflection plane, R, about the m_y-direction, and a symmorphic inversion point, I, which takes a point $\vec{r}$ on the lattice to $-\vec{r}$. (d) The glide-plane symmetry $\mathcal{G}(k_x, k_y)$ transforms the $|k_x, k_y\rangle_\alpha$ eigenstate of the Bloch Hamiltonian $\mathcal{H}(k_x, k_y)$ into the $|k_x, -k_y\rangle_{\alpha'}$ eigenstate of $\mathcal{H}(k_x, -k_y)$, and vice-versa. N is the number of bands ($N = 4$ for the lattice depicted in (c)).

34

The invariance of the lattice with respect to the glide-plane transformation G is manifest as followed:

$$\mathcal{G}(k_x, k_y)\mathcal{H}(k_x, -k_y)\mathcal{G}^{-1}(k_x, k_y) = \mathcal{H}(k_x, k_y), \tag{3.24}$$

where $\mathcal{G}(k_x, k_y)$ is the 4×4 matrix representation of G in the basis constructed by the eigenstates of $\mathcal{H}(k_x, k_y)$. The k_x-dependance of $\mathcal{G}$ stems from the fractional translation along the m_x-direction, while the k_y-dependance originates from the shift of the glide plane from the center of the unit cell along the m_y-direction, as shown in Fig. 3.5(c). So G is an unusual symmetry which is both nonsymmorphic (along m_x) and off-centered [167, 168] (along m_y). Such a glide plane differs from the one used to prove band-degeneracy enforcement in a 1D two-band model, the latter being a 2×2 matrix which depends on only one momentum coordinate [134, 135].

We show in I that $\mathcal{G}(k_x, k_y)|k_x, -k_y\rangle_{\alpha'} \rightarrow |k_x, k_y\rangle_{\alpha}$, where $|k_x, k_y\rangle_{\alpha}$ $(\alpha = 1, 2, 3, 4)$ is a Bloch eigenstate of $\mathcal{H}(k_x, k_y)$. This transformation between the negative-k_y and positive-k_y Bloch eigenspaces is illustrated in Fig. 3.5(d). On the lines $k_y = \bar{k}_y = 0, \pm\pi$, $\mathcal{H}(k_x, -\bar{k}_y) = \mathcal{H}(k_x, \bar{k}_y)$. Eq. (3.24) thus yields $[\mathcal{G}(k_x, \bar{k}_y), \mathcal{H}(k_x, \bar{k}_y)] = 0$ and, hence, $|k_x, \bar{k}_y\rangle_{\alpha}$ are also eigenstates of $\mathcal{G}(k_x, \bar{k}_y)$. By constructing the matrix $\mathcal{G}(k_x, k_y)$ (shown in I), we obtain the two-fold degenerate eigenvalues of $\mathcal{G}(k_x, \bar{k}_y)$: $\xi_{1,3} = \exp(ik_x/2)$, and $\xi_{2,4} = -\exp(ik_x/2)$. As k_x swipes the BZ from $-\pi$ to π, the $(+)$-eigenvalues wind around the half-unit circle on the complex plane from $-i$ to i through 1, while the $(-)$-eigenvalues wind from i to $-i$ through -1, as illustrated on Fig. 3.6(a). As a result, the eigenstates $|-\pi, \bar{k}_y\rangle_{1,3}$ and $|\pi, \bar{k}_y\rangle_{2,4}$ have the same $\mathcal{G}$-eigenvalue, $-i$, and the eigenstates $|\pi, \bar{k}_y\rangle_{1,3}$ and $|-\pi, \bar{k}_y\rangle_{2,4}$ have the same $\mathcal{G}$-eigenvalue, i. It follows that the associated pairs of $\mathcal{H}$-eigenvalues must cross at least once along the k_x-axis [134] (when $k_y = \bar{k}_y$), as shown in Figure 3.6(b). From this analysis we conclude that the glide-plane symmetry enforces the appearance of two nodal points at $k_y = 0$ and two nodal points at $k_y = \pm\pi$. These nodal points are the precursors of symmetry-enforced NLs.
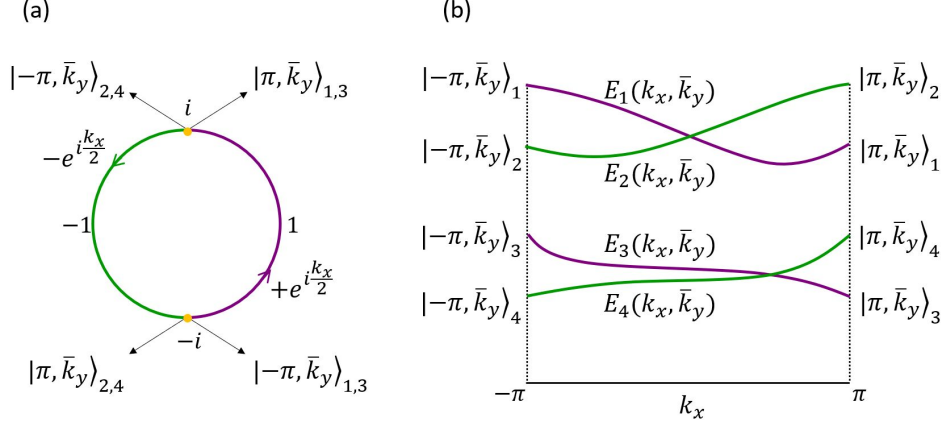
Figure 3.6: (a) Doubly-degenerate eigenvalues $\pm e^{i\frac{k_x}{2}}$ of the glide-plane matrix winding around the half-unit circles on the complex plane, one pair of eigenvalues from $-i$ to i through 1, and the other pair from i to $-i$ through -1. The eigenstates $|\pm\pi, \bar{k}_y\rangle_{1,3}$ and $|\pm\pi, \bar{k}_y\rangle_{2,4}$ associated to the extreme points of the eigenvalue-trajectories are indicated. (b) The behavior of the eigenvalues of the glide-plane matrix implies that the eigenvalues of the Bloch Hamiltonian must cross pairwise at some value of k_x.

To further clarify the origin of the nodal points depicted in Fig. 3.6(b), we analyze the simplest tight-binding model for the lattice shown in Fig. 3.5(c) in which only hopping between nearest-neighbor sites and on-site energies are considered. The entries of the corresponding Bloch Hamiltonian $\mathcal{H}(k_x, k_y)$ read:

$$\varepsilon_{n,m}(k_x, k_y) = t_{n,m} + t^*_{m,n} + u_{n,m}e^{ik_x} + u^*_{m,n}e^{-ik_x} + v_{n,m}e^{ik_y}$$
$$+ v^*_{m,n}e^{-ik_y} + w_{n,m}e^{i(k_x+k_y)} + w^*_{m,n}e^{-i(k_x+k_y)}, \tag{3.25}$$

where $n, m = 1, ..., 4$, and $t_{n,m}$, $u_{n,m}$, $v_{n,m}$, and $w_{n,m}$ denote the hopping energy from site m to n within the same unit cell, between neighboring unit cells along the x-direction, y-direction, and diagonal direction, respectively, and with $t_{n,n} = \mu_n$ the on-site energy. In Eq. (3.25), only $u_{2,1} = t_{2,1}$, $u_{4,1} = t_{4,1}$, $u_{4,3} = t_{4,3}$ along x, $v_{1,3} = t_{1,3}$, $v_{2,3} = t_{2,3}$, $v_{2,4} = t_{2,4}$ along y, and $w_{2,3} = t_{2,3}$ along the diagonal are non-vanishing neighboring hopping (c.f. Figure 3.5(c)).

Imposing Eq. (3.24), with $\mathcal{G}(k_x, k_y)$ given by Eq. A-1.6, leads to Eqs. A-1.9-A-1.12 constraining the entries $\varepsilon_{n,m}(k_x, k_y)$ of $\mathcal{H}(k_x, k_y)$. A similar argument to the one used for the off-diagonal entry of a 1D two-band model [134] can be applied here to show that Eq. S9 implies that $\varepsilon_{n,n+1}(k_x, \bar{k}_y)$, $n = 1, 3$, must vanish at some value of k_x. In a 1D two-band model with only one off-diagonal entry, its vanishing is sufficient to guarantee a band crossing. In a four-band model, on the other hand, the vanishing of only two of its off-diagonal entries is not a sufficient condition. For a 1D multi-band model, band crossings occur provided that the model has, on top of the nonsymmorphic symmetry, also chiral symmetry [134]. Chiral symmetry means that the Bloch Hamiltonian admits an off-diagonal block form which, in turn, means that half of its entries are identical to zero. This is clearly not the case of our 2D four-band $\mathcal{H}(k_x, k_y)$ with entries given by Eq. (3.25), which allows

for hopping between any two intracell sites and on-site energies. This is particularly relevant for making a connection with a real 2D material in which hopping occurs in all directions. Therefore, the (nonsymmorphic + chiral)-symmetries argument designed for the 1D multi-band case is not applicable here.

Instead, we must impose all Eqs. A-1.9-A-1.12 on the entries given by Eq. (3.25). This yields the entries constrained by the glide-plane symmetry given by Eqs. A-1.13-A-1.17. The upper panel of Fig. 3.7(a) shows two views of the band structure of the glide-plane invariant effective model given by Eqs. A-1.13-A-1.17 on the positive quadrant of the $k_x - k_y$ plane, for $\mu_1 = \mu_3 = 0$ and $t_{2,1} = t_{4,3} = t_{1,3} = t_{3,1} = t_{1,4} = t_{4,1} = \exp(i0.3\pi)$ (with μ's and t's given in arbitrary units). The bands touch pairwise at some value of k_x, provided $k_y = \bar{k}_y = 0, \pi$. The lower panels of Fig. 3.7(a) depicts the projection of the nodal points on the $k_x - k_y$ plane, with the 1D two-band model result [134] shown on the left for comparison. Including higher-order hopping in Eq. (3.25) will move the glide-plane enforced nodal points along k_x, but will not gap them out since higher-order hopping preserve the glide-plane symmetry. We thus see that exact diagonalization of the effective model confirms the previous prediction derived from the general relations obeyed by the eigenvalues of $\mathcal{H}(k_x, k_y)$ and $\mathcal{G}(k_x, k_y)$, namely, that the glide-plane symmetry enforces two pairs of nodal points, one pair at $k_y = 0$ and another at $k_y = \pm\pi$. Having the energy spectrum and the corresponding single-particle states wielded by exact diagonalization, one can form the density matrix and compute thermodynamic averages or, using linear response theory, extract transport properties. For the present purpose of demonstrating the existence of NLs, next we show how the remaining symmetries turn G-enforced two pairs of nodal points into two NLs pinned at the $k_x = \pi$ edge of the BZ.
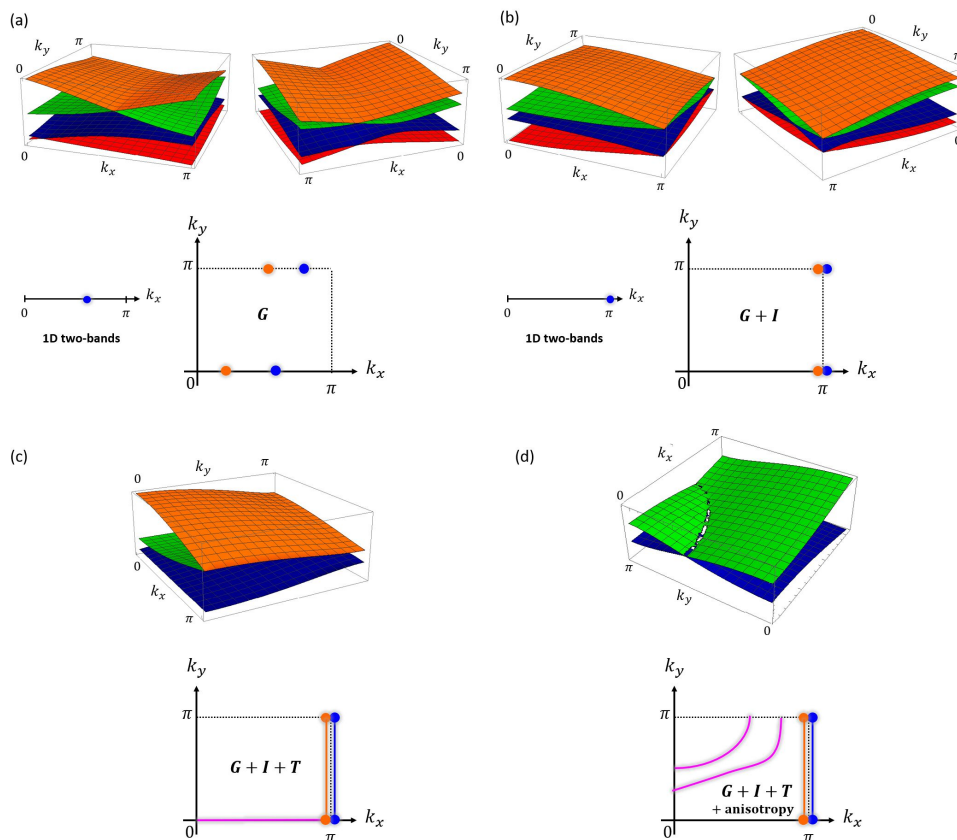
Figure 3.7: (a)-(d) upper panels: Energy bands of the effective model with glide-plane (G) symmetry, with glide-plane (G) + inversion-point (I) symmetries, with glide-plane (G) + inversion-point (I) + time-reversal (T) symmetries, and with glide-plane (G) + inversion-point (I) + time-reversal (T) symmetries + anisotropy, respectively. (a)-(d) lower panels: Projection on the $k_x - k_y$ plane of the nodal points or nodal lines shown on the corresponding upper panels. The lower panels of (a) and (b) contain also the 1D two-band result for comparison. The lower panel of (d) illustrates two accidental nodal lines inside the Brillouin zone, corresponding to different anisotropic cases.

3.6 Effect of inversion and time-reversal symmetries

The invariance relation representing the symmetry of the lattice with respect to the inversion-point transformation I is

$$\mathcal{I}(k_y)\mathcal{H}(-k_x, -k_y)\mathcal{I}^{-1}(k_y) = \mathcal{H}(k_x, k_y), \tag{3.26}$$

where $\mathcal{I}(k_y)$ is the 4×4 matrix representation of I in the basis constructed by the eigenstates of $\mathcal{H}(k_x, k_y)$. Similar to what happens with $\mathcal{G}$, the k_y-dependance of $\mathcal{I}$ is a consequence of the shift of I from the center of the unit cell along the m_y-direction, as shown in Fig. 3.5(c)).

Combining the constraints imposed by Eq. (3.26) with those from Eq. (3.24), we obtain Eqs. A-2.10-A-2.14 which give the off-diagonal entries of the glide-plane and inversion-point invariant effective model. The resulting band structure and projection of nodal points on the $k_x - k_y$ plane are

shown on the upper and lower panels of Fig. 3.7(b) for $\mu_1 = \mu_3 = 0$, $t_{2,1} = t_{4,3} = 1$ (I-symmetry implies that these hopping parameters must be real), and $t_{1,3} = t_{3,1} = t_{1,4} = \exp(i0.3\pi)$. Fig. 3.7(b) conveys that the effect of the inversion-point symmetry is to pin at $k_x = \pi$ the four nodal points of the glide-plane invariant effective model. The inversion-point combines with a last local constraint on the Hamiltonian to generate NLs at $k_x = \pi$. Within the present framework, the influence of the inversion-point symmetry alone, i.e. with no additional constraints, is simply to push the nodal points enforced by the glide-plane symmetry to $k_x = \pi$. The NLs emerge only when invoking time-reversal symmetry, as we shall see next. For completeness, the known result from the 1D two-band model is shown on the left side of the lower panel of Fig. 3.7(b). It can be shown that G and I imply R. Therefore, it is sufficient to analyze the constraints imposed by G and I on the band structure.

Turning to the time-reversal transformation T, the invariance relation is given by

$$\mathcal{T}\mathcal{H}^*(-k_x, -k_y)\mathcal{T}^{-1} = \mathcal{H}(k_x, k_y), \tag{3.27}$$

where $\mathcal{T} = \mathbb{1}_{4\times 4}$ since $\mathcal{H}(k_x, k_y)$ is spinless.

Imposing Eq. 3.27 implies that the entries of $\mathcal{H}(k_x, k_y)$ satisfy $\varepsilon^*_{n,m}(-k_x, -k_y) = \varepsilon_{n,m}(k_x, k_y)$ which, given Eq. (3.25), yields real hopping parameters. As can be seen in the upper and lower panels of Fig.3.7(c), in which $\mu_1 = \mu_3 = 0$, $t_{2,1} = t_{4,3} = t_{1,3} = t_{3,1} = t_{1,4} = 1$, the effect of time-reversal symmetry on the band structure of the glide-plane and inversion-point invariant effective model is two-fold: it connects the symmetry-enforced nodal points of the same pair of bands, thus forming two NLs at $k_x = \pi$, and it also induces an additional NL at $k_y = 0$. While the former NLs are symmetry-enforced, the later is accidental, being gapped, for instance, by an anisotropy of the hopping parameters, as we shall see next section.

3.7   Effect of anisotropy

Here we discuss another feature of the band structure which is special to our scheme of engineering a nonsymmorphic symmetry out of vacancies: The appearance of unusually robust accidental NLs in the interior of the BZ. Accidental band crossings are usually very fragile to perturbations or change in material parameters. The appearance of NLs inside the BZ which survived extremely strong SOC and magnetic exchange field (of strengths nearing or exceeding current experimental bounds) was initially conjectured to come from symmetry enforcement. The framework developed here conclusively resolves this puzzle and identifies the origin of such unusually robust, yet accidental, NLs.

In a pristine monoatomic lattice in which the distance between neighboring atoms is the same in all directions (such as borophene), the hopping amplitudes are direction-independent. In such an isotropic environment (and disregarding non-structural degrees of freedom such as orbitals and spin), the crossings between energy bands are the ones associated only to the symmetries, as we have seen in the previous sections. Defects (including vacancies) break the isotropy of the hopping amplitudes, with the result that now bands can cross also in generic places of the BZ.

For the particular band structure shown in Fig. 3.7(c), the anisotropy gaps out the accidental NL at $k_y = 0$, but creates another accidental NL between the middle bands in the interior of the BZ, as shown on the upper panel of Fig. 3.7(d) where $\mu_1 = \mu_3 = 0$, $t_{21} = t_{43} = 1$, and $t_{13} = t_{31} = t_{14} = 100$. Smoothly changing the anisotropy between the hopping amplitudes makes the NL move and change shape through the BZ, as illustrated on the lower panel of Fig. 3.7(d). Eventually, the NL starts to fade and finally disappears when the parameters are taken out of a certain anisotropic regime. Unlike accidental NLs of nonstructural origin, which are easily gapped by perturbations, anisotropy-induced accidental NLs should have an enhanced robustness owing to their structural origin. This feature can be traced to the fact that perturbations do not restore isotropy (sometimes they might actually enhance the anisotropy). Finally, while anisotropy in the Hamiltonian parameters induces accidental NLs inside the BZ, this is not a sufficient condition. The appearance of such NLs is preconditioned by the presence of time reversal symmetry. We will further elaborate on this point in the next section where the shapes of the accidental NLs of vacancy-engineered borophenes signal their connection to time-reversal symmetry.

We conclude that a nonsymmorphic 2D material created by vacancy-engineering possesses symmetry-enforced NLs at one edge of the BZ originated from a glide-plane symmetry (combined with inversion-point and time-reversal symmetries), and also accidental NLs with enhanced robustness in the interior of the BZ from the vacancy-induced anisotropy and time-reversal symmetry.

3.8 Confirmation of our symmetry analysis with DFT results

Fig. 3.8(a)-(b) show the band structure of B_{10} and B_{16}, respectively, both without Rashba SOC ($\lambda = 0$). The bands are given along the Γ-X-V-Γ-Y-V path in the BZ (points Γ, X, V, and Y are shown on the left panel of Figure 3.8(e)). Fig. 3.8(a)-(b) indicate that bands stick together pairwise, forming NLs, along the X-V direction (corresponding to $k_x = \pi/a$). Fig. 3.8(c)-(d) show the amplified image of the bands inside the red rectangles in Fig. 3.8(a)-(b), respectively, but in the presence of Rashba SOC ($\lambda = 0.05$ eV). Fig. 3.8(e)-(f), left panels, are the contour plots in the $k_x - k_y$ plane of the lower NL indicated by the arrow in Fig. 3.8(a)-(b), respectively. In these contour plots, the orange line running along X-V represents the vanishing of the energy difference between the sticking bands. Fig. 3.8(g)-(h), left panels, are the contour plots of the NLs which exist in the interior of the BZ of the band structures shown in Fig. 3.8(a)-(b), respectively, within an energy window of 2.0 eV about the Fermi energy. Fig. 3.8(e)-(h), right panels, show the contour plots of the NLs in the corresponding left panels but with Rashba SOC of strength $\lambda = 0.05$ eV in Fig. 3.8(e)-(f) and $\lambda = 0.1$ eV in Fig. 3.8(g)-(h).
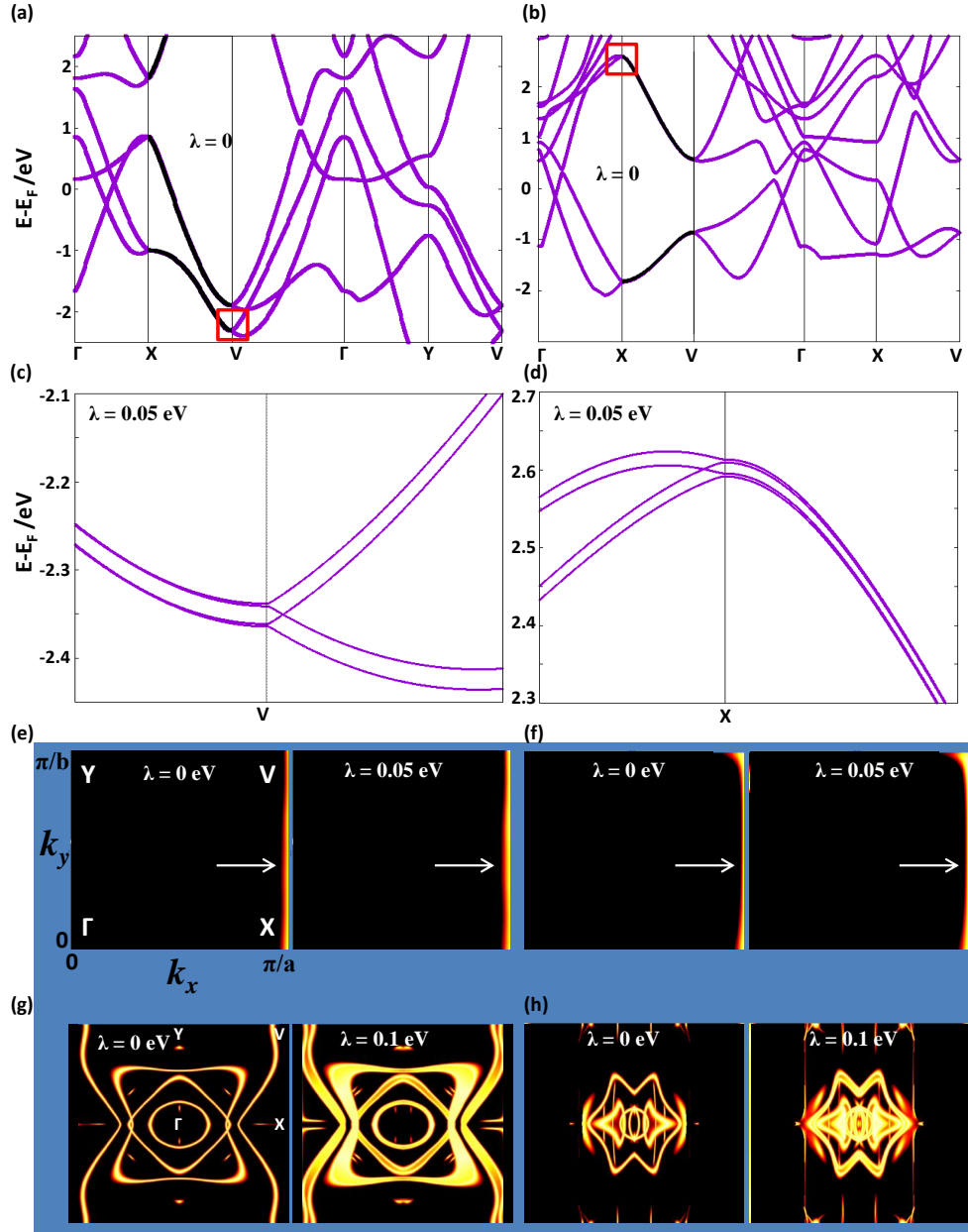
Figure 3.8: (a) [(b)] Band structure of B_{10} [B_{16}] without Rashba spin-orbit coupling (SOC) ($\lambda = 0$ eV) along the Γ-X-V-Γ-Y-V path in the Brillouin zone, with the position of points Γ, X, V, and Y given in the left panel of (e). The symmetry-enforced nodal lines along the X-V direction are highlighted in black. (c)[(d)] Amplified image of the bands inside the red rectangles in (a)[(b)], but in the presence of Rashba SOC ($\lambda = 0.05$ eV). Each four-fold degenerate symmetry-enforced nodal line splits into a pair of spin-split two-fold degenerate nodal lines. (e) [(f)] Contour plot of the symmetry-enforced nodal lines shown in (a) [(b)] without Rashba SOC in the left panel ($\lambda = 0$ eV) and in the presence of Rashba SOC in the right panel ($\lambda = 0.05$ eV). The nodal lines, which are pinned at the edge $k_x = \pi/a$ of the Brillouin zone, are indicated by arrows. (g) [(h)] Contour plot of all accidental nodal lines which exist within an energy window of 2.0 eV about the Fermi energy in the band structure shown in (a) [(b)], without Rashba SOC in the left panel ($\lambda = 0$ eV) and in the presence of Rashba SOC in the right panel ($\lambda = 0.1$ eV).

Chapter 4

Excitons and Optical Properties of 2D van der Waals Heterostructures

This chapter presents the calculation of excitons in 2D semiconductors, by solving the Bethe–Salpeter equation. With this calculation, we will study the optical spectra of 2D materials and their heterostructure by depositing on magnetic substract.

4.1 Introduction

When light hits a semiconductor, it excites one of the electrons to a higher conduction band level, leaving a positive charge (hole) at the valence band level. In the early studies of condensed matter physics, it was believed that the excitation process of electrons has nothing to do with holes. Therefore, the minimum photon energy $E_g^{optical}$ required for electron excitation is the energy level difference E_g^{elec} between the bottom of the conduction band E_{CBM} minus the top of the valence band E_{VBM} ($E_g^{optical} = E_g^{elec} = E_{CBM}$ - E_{VBM}), which is the edge of the light absorption spectrum, as shown in Fig. 4.4(a). However, with the development of research, there are some systems where the light absorption peak is smaller than the minimum photon energy calculated according to $E_g^{optical} = E_g^{elec} = E_{CBM}$ - E_{VBM}. Such a phenomenon has been found, for example, in the low-temperature spectroscopic measurements of Cu_2O and KBr. When we consider the interaction of electrons and holes to form excitons (as shown in Fig. 4.4(b)), these spectral lines can be well explained by the exciton model.
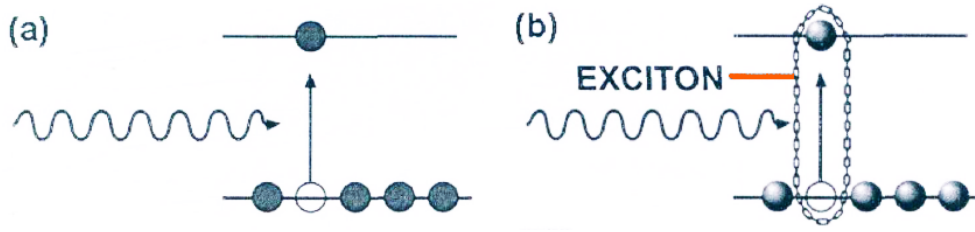
Figure 4.1: The photon-excitation model in solids without consideration (a) and with consideration (b) of electron-hole interaction

Excitons are hypothetical quasiparticles that belong to a kind of meta-excitation, first proposed by Frenkel. The most basic idea is that a bound state energy level is formed between the valence band and the conduction band (the red horizontal line in Fig. 4.4(b))), due to the Coulomb interaction between the excited electron and the hole left. In this way, the energy of the absorbed photon is reduced from E_g^{elec} to the energy level difference between the bound state energy level and the VBM. The energy difference between the CBM and the bound state is defined as the exciton binding energy. Usually in three-dimensional solids, there are two types of excitons: weakly bound Mott-Wannier excitons and tightly bound Frenkel excitons. In three-dimensional solid materials, weakly bound excitons are generally defined as the average distance between electrons and holes greater than the atomic radius. In fact, it is because the Coulomb interaction is relatively weak, and the binding energy is generally in the order of 1-10 meV. Tightly bound excitons are the opposite. Tightly bound excitons generally exist in ionic crystals, while weakly bound excitons are widespread in almost all other semiconductors.

For weakly bound excitons, since the most basic interaction of the exciton model is the Coulomb force between pairs of positive and negative charges, therefore the excitons can be mathematically described using the hydrogen-like model. Under the effective mass approximation, the exciton Hamiltonian can be written as:

$$
\begin{aligned}
H = & \frac{p_e^2}{2m_e^*} + \frac{p_h^2}{2m_h^*} - \frac{q^2}{4\pi\epsilon|r_e - r_h|} \\
= & \frac{p_R^2}{2(m_e^* + m_h^*)} + \frac{p^2}{2\mu^*} - \frac{q^2}{4\pi\epsilon\epsilon_0 r}
\end{aligned}
\tag{4.1}
$$

where $m_{e/h}^*$ is the effective mass of electron/hole, $r_{e/h}$ is the position coordinate of electron/hole, ϵ is the dielectric constant of the crystal, q is the charge and μ is the reduced mass, p_R and p are the momentum corresponding to the centroid and relative coordinates, with

$$
R = \frac{m_e^* r_e + m_h^* r_h}{m_e^* + m_h^*}.
\tag{4.2}
$$

The wavefunction should be an exponential form of $\Phi(r)e^{ikR}$, which satisfies the equation:

$$
(\frac{p^2}{2\mu^*} - \frac{q^2}{4\pi\epsilon\epsilon_0 r})\Phi(r) = E_b\Phi(r)
\tag{4.3}
$$

This is the equation describing the interaction of hydrogen-like atoms, the interaction energy

(the eigenvalue E_b) can be written directly in the form of hydrogen-like atomic energy levels:

$$E_b = \frac{(q^2/4\pi\epsilon)^2}{2(\hbar^2/\mu^*)n^2} \tag{4.4}$$

where n is the quantum number of energy level. From this, the exciton energy levels we calculated should be discrete energy levels from the middle of the band gap to the conduction band just like the hydrogen-like atoms, as shown in Fig. 4.2. In addition, from this energy expression, we can obtain the following basic information about weakly bound excitons by analogy with hydrogen atoms: when the effective mass of the carrier in the semiconductor is relatively small and the dielectric constant is relatively large, the interaction between electrons and hole in the excitons is similar as $\frac{\mu^*}{m_0\epsilon^2}$ times the first energy level (13.6 eV) of the hydrogen atom, which is about 0.01 eV. Its radius expands to approximately $\frac{m_0\epsilon}{\mu^*}$ times the Bohr radius. Let us come back to the equations of motion, the total energy of the excitons can be expressed as:

$$E = \frac{\hbar^2 k^2}{2(m_e^* + m_h^*)} + E_b \tag{4.5}$$
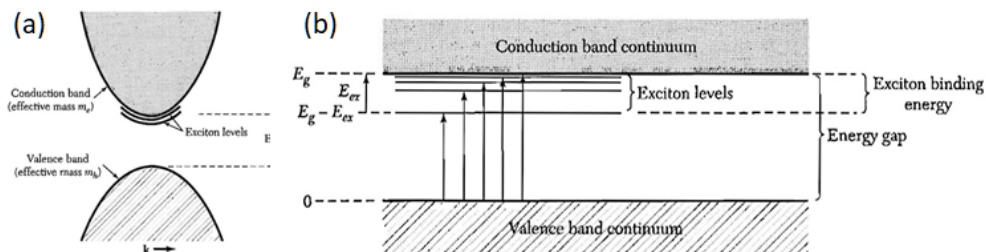
Figure 4.2: (a) Exciton energy levels shown on band gap diagram. (b) Energy levels of an exciton created in a direct process where k is neglected for clarity. Optical transitions from the top of the valence band are shown by the arrows.

During light absorption of exciton, two conditions need to be satisfied at the same time: conservation of energy and conservation of momentum. We assume that the quasi-momentum of electrons and holes is constant before and after the transition, that is to say, $k = 0$ in the above formula, so we only need to consider the photon energy as:

$$\begin{aligned} \hbar\omega &= E_g - \frac{(q^2/4\pi\epsilon)^2}{2(\hbar^2/\mu^*)n^2} \\ &= E_g - E_b \end{aligned} \tag{4.6}$$

where we can clearly see that after considering the exciton effect, the minimum absorbed photon energy is reduced by E_b compared with the original E_g.

In most semiconductors and insulators, the condition for weakly bound excitons can be satisfied, so Mott-Wannier excitons are relatively common. For tightly bound excitons, although their mutual use is essentially unchanged, the electrons and holes are located in the same unit cell or even around the same atom. Therefore, the complex surrounding dielectric environment makes the condition $\epsilon > 1$ invalid, so the hydrogen-like atom model is no longer applicable. Frenkel believed

that excitons with small moving radius are actually the transfer of excited electrons from one atom to another within the same atom. The specific model can refer to Ref. [169], which will not be described in detail here.

4.2 Development of Exciton models in 2D materials

Although GW+BSE has been recognized as an accurate method for first-principles calculation of excitons, the development of exciton models is still helpful for understanding the properties of excitons in 2D materials and estimating exciton-related information at low computational cost. In 2D materials, Zhang first proposed that there is a linear relationship between the binding energy of excitons and the band gap of quasiparticles [8]:

$$E_b = 0.12 * E_g + 0.4 \tag{4.7}$$

which are obtained by using the method of computational data fitting, and using the effective mass theory to understand the linear law under the condition of $\epsilon = 1$. But it can not give a good explanation of the coefficients and intercepts of the curves. In the 2D system, although the dielectric shielding has been greatly weakened, it does not mean that the global $\epsilon = 1$ can be considered in all 2D systems. Therefore, it is necessary to introduce the modified expression of the dielectric function [170]:

$$\epsilon(Q_{ex}) = 1 + 2\pi\alpha_{2D}|q_{ex}| \tag{4.8}$$

where q_{ex} is the center-of-mass momentum of exciton. Based on this, Duan team modified this linear relationship in the form of analytical derivation. Without considering the local field approximation, the simplified dielectric function expression was obtained:

$$
\begin{aligned}
\epsilon_{3D} &= \lim_{q_{ex}\to 0} \epsilon_{00}(q_{ex}, \omega = 0) \\
&= 1 + \lim_{q_{ex}\to 0} \frac{16\pi e^2}{V|q_{ex}|^2 \times \sum_k \sum_{c,v} |\langle v,k|e^{-iq_{ex}r}|c,k+q_{ex}\rangle|^2} \times \frac{1}{E_{c,k+q_{ex}} - E_{v,k}}
\end{aligned}
\tag{4.9}
$$

where the module square of the wave functions $|\langle v,k|e^{-iq_{ex}r}|c,k+q_{ex}\rangle|^2$ can be done with Taylor expansion of $q_{ex} \to 0$ by the Bloch wave. Using the $k \cdot p$ perturbation [171], the α in Eq. 4.8 can be expressed as:

$$\alpha_{2D} = \frac{N_g e^2}{2\pi E_g} \tag{4.10}$$

where N_f is the energy level. Combining with the expression the Ref. [172]:

$$E_B = \frac{8^4}{\hbar^2(1 + \sqrt{1 + \frac{32^2}{3\hbar}\alpha^2 D\mu})^2}, \tag{4.11}$$

it finally obtain the linear relationship between exciton binding energy and quasiparticle band gap:

$$E_b = \frac{3}{2N_g} E_g \tag{4.12}$$

Usually we have $N_g = 6$ for a hexagonal lattice like graphene, then it is obtained that:

$$E_b = \frac{1}{4}E_g, \tag{4.13}$$

which is always in good agreement for most 2D materials (as shown in Fig. 4.3). Although the values used for hexagonal lattices are taken above, good predictions can still be made in some tetragonal lattice materials (such as black phosphorus). And although it is discussed in the article that large errors may occur when the quasiparticle band gap is greater than 4.eV, this relationship still holds for hexagonal boron nitride (bandgap greater than 5.eV). Therefore, in most cases, this linear relationship can be used to estimate the exciton binding energies of most 2D materials.
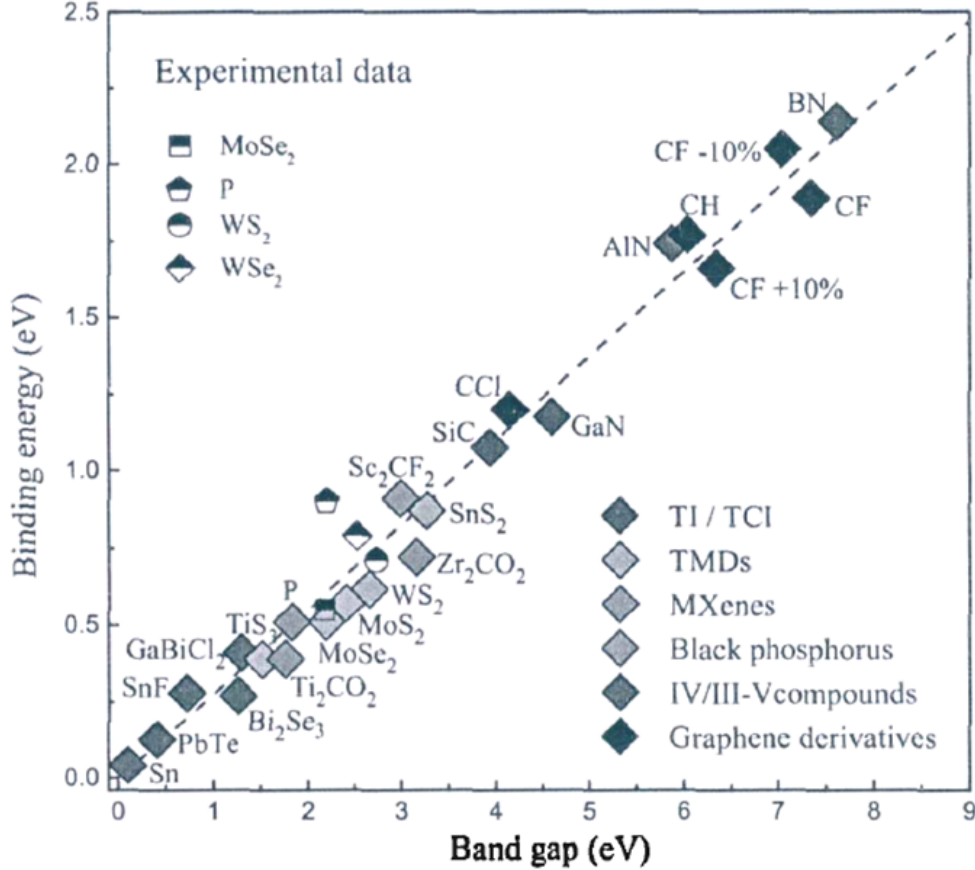
Figure 4.3: The linear relationship between exciton binding energy and quasiparticle band gap [8]

In order to better understand the various related effects caused by changes in dielectric shielding in two-dimensional materials, it is necessary to start with the dielectric function itself. In this regard, Professor K. S. Thygesen did a series of excellent work [173, 174]. They not only carried out model analysis and numerical analysis of the dielectric function in two-dimensional materials, but also extended it to multilayer and heterojunction materials. From this, the dielectric function database is established, and the model method developed by them can be used to make a relatively accurate estimation of excitons in two-dimensional materials with a small computational cost.

4.3 Valley Excitons

Valleytronics is a very special property of transition metal dichalcogenides (TMD) materials. The concept of electron valley was proposed in graphene, which means that at the edge (the K point) of the first Brillouin zone of the hexagonal lattice, there is a new degree of freedom similar to charge and spin. Particles in the valley may exhibit σ polarization properties similar to their spins at $\pm K$ point, and can be used as carriers for storing information. But only in a system with broken inversion symmetry such as TMD, can valley electron flow be generated. Therefore, it is possible to observe and utilize the value T the $\pm K$ points with $\pm \sigma$. In TMD, exciton peaks with valley properties, called valley excitons, are observed in the PL spectrum by irradiating the sample with circularly polarized light experimentally, as shown in Fig. 4.4. At present, valley exciton polarization in TMD has not reached the ideal state of preserving information in terms of lifetime and discrimination, so much work has been devoted to understanding the valley polarization mechanism and regulating the lifetime and discrimination of valley excitons [175].
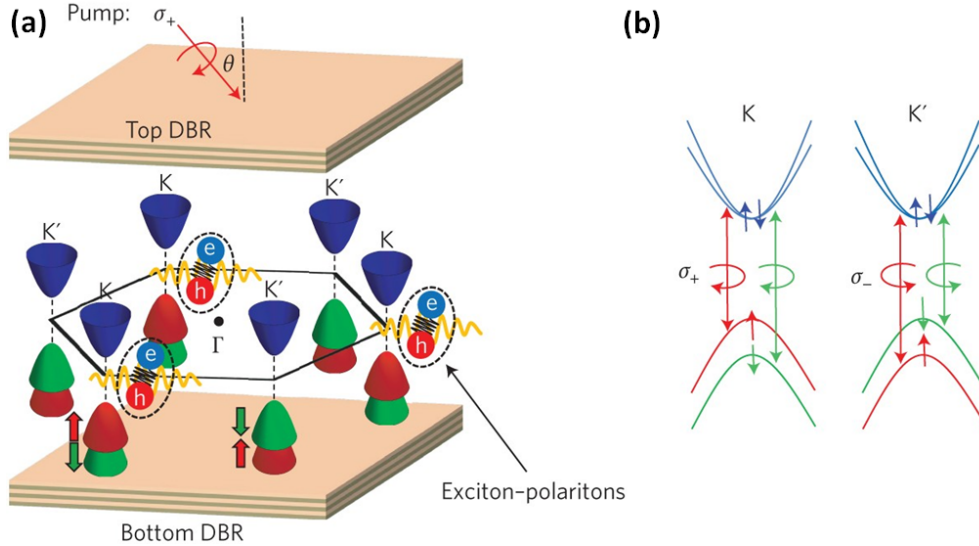
Figure 4.4: Schematic of valley-polarized exciton–polaritons. Monolayer MoS_2 is represented in reciprocal space. (a) Coloured surfaces represent the conduction (blue) and spin-up and spin-down (red and green) valence band dispersions. When the material is pumped by circularly polarized light ($\sigma+$) at angle θ, strongly coupled exciton–polaritons are created primarily in the K valleys. (b) Valley and spin optical transitions of MoS_2.

4.4 Bethe–Salpeter equation

The Bethe-Salpeter equation (BSE) is actually found via the rigorous treatment of the problem within Green's-function theory [176]. It requires the correct calculation of the quasi-electron and the quasi-hole (for example, via GW approximation) and contains an interaction term that mixes the formerly independent transitions. The interaction term in real space, or called Non-interacting density response function χ, can be represented by the four-point Feynman diagrams in Fig. 4.5. It

has been very successful in describing the absorption spectra of a large variety of systems, including insulators, semiconductors, atoms, clusters, surfaces or polymers. First principle methods have been widely used to investigate optical properties applying the BSE, like the Yambo package [177]. However, the computation cost is very expensive due to the bottleneck step of the all-band calculation, which leads to optical spectra based on modest reciprocal space sampling with poor resolution.
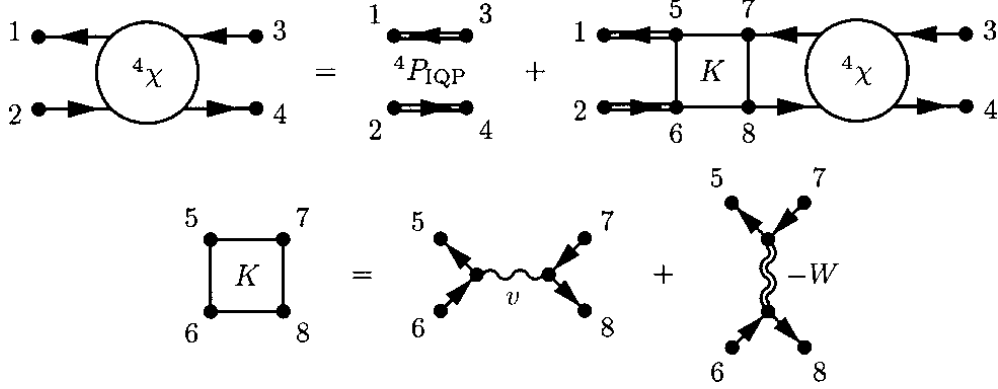
Figure 4.5: Feynman diagrams representing the Bethe-Salpeter equation for χ

The first step of the BSE approach is the calculation of the ground state $|g\rangle$. This is nothing else than the solution of the TB model for a correct sampling of the Brillouin zone, as we did in the borophene chapter be combining DFT calculation and post-treatment by Wannier90 package, say:

$$H(k)\Phi_{n,k}(r) = E_n\Phi_{n,k}(r).\tag{4.14}$$

Here we have to pay attention to our interesting zone in the Brillouin zone (BZ).The wavefunctions are periodic over the BZ, but the interaction potential is not. Thus to capture all the effect of the interaction for a chosen k-point, it is better to chose this k-point close to the light zone. The most important points are K and K' in the center of BZ, which are responsible for the main A and B exciton series [178]. If the K points on the edge of the BZ are chosen, the degeneracies and values of the A and B excitons are not correctly reproduced. By placing K/K' points close to the center of the BZ, we avoid the need of inclusion of the 'local field corrections' to the interaction potential [179].

The second step is to define the wave functions of excitons. In this chapter we consider excitons with zero center of mass momentum, which are the ones that can be optically bright and contribute to the optical conductivity. The wave function of the m-th exciton with center-of-mass momentum $\vec{k}_{ex}$ (we put the value of zero in this chapter) is defined as a linear combination of electron-hole pairs $|vc\rangle = \sum_{\vec{k}} \hat{a}^\dagger_{c(\vec{k}+\vec{k}_{ex})}\hat{a}_{v\vec{k}}|g\rangle$:

$$|X^{m,\vec{k}_{ex}}\rangle = \sum_{vc} A^{(m,\vec{k}_{ex})}_{vc}|vc\rangle = \sum_{vc\vec{k}} A^{(m,\vec{k}_{ex})}_{vc\vec{k}}\hat{a}^\dagger_{c(\vec{k}+\vec{k}_{ex})}\hat{a}_{v\vec{k}}|g\rangle,\tag{4.15}$$

where c and v are the index of conduction band and valence band, respectively, $\hat{a}^\dagger_{c(\vec{k}+\vec{k}_{ex})}$ is the

creation operator of an electron at conduction band, $\hat{a}_{v\vec{k}}$ is the annihilation operator of an electron at valence band, $|g\rangle$ is the non-interacting ground state, and $A_{vc\vec{k}}^{(m,\vec{k}_{ex})}$ is the BSE expansion coefficient. Let us define the BSE Hamiltonian as H^{BSE}, and we have:

$$H^{BSE}_{vc\vec{k}\vec{k}_{ex},v'c'\vec{k}'\vec{k}'_{ex}} = \langle vc\vec{k}\vec{k}'\vec{k}_{ex}|H^{BSE}|v'c'\vec{k}'\vec{k}'_{ex}\rangle = [e_{c(\vec{k}+\vec{k}_{ex})} - e_{v\vec{k}}]\delta_{vv'}\delta_{cc'}\delta_{\vec{k}\vec{k}'}\delta_{\vec{k}_{ex}\vec{k}'_{ex}} + K_{vc\vec{k}\vec{k}_{ex},v'c'\vec{k}'\vec{k}'_{ex}}$$
$$(4.16)$$

where $K_{vc\vec{k}\vec{k}_{ex},v'c'\vec{k}'\vec{k}'_{ex}}$ is the BSE kernel, $e_{v\vec{k}/c(\vec{k}+\vec{k}_{ex})}$ is the single-particle valence/conduction band energy, obtained by TB model. And the form of BSE is as followed:

$$[e_{c(\vec{k}+\vec{k}_{ex})} - e_{v\vec{k}}]A_{vc\vec{k}}^{(m,\vec{k}_{ex})} + \frac{1}{S_{uc}N_k}\sum_{v'c'\vec{k}'}K_{vc\vec{k},v'c'\vec{k}',\vec{k}_{ex}}A_{v'c'\vec{k}'}^{(m,\vec{k}_{ex})} = E_m A_{vc\vec{k}}^{(m,\vec{k}_{ex})}, \qquad (4.17)$$

where S_{uc} is the area of unit cell and N_k is the total number of k points in the Brillouin zone, used in the TB model, E_m is the excitonic energy. The BSE kernel $K_{vc\vec{k},v'c'\vec{k}',\vec{k}_{ex}}$ is the Coulomb interaction between two electron-hole pairs, including the direct interaction K^d, and the exchange interaction K^x [176]:

$$\begin{aligned}K_{vc\vec{k},v'c'\vec{k}',\vec{k}_{ex}} =& K^d_{vc\vec{k},v'c'\vec{k}',\vec{k}_{ex}} + K^x_{vc\vec{k},v'c'\vec{k}',\vec{k}_{ex}}\\ =& U(\vec{k}-\vec{k}')I_{c(\vec{k}+\vec{k}_{ex}),c'(\vec{k}'+\vec{k}_{ex})}I_{v'\vec{k}',v\vec{k}} - U(\vec{k}_{ex})I_{c(\vec{k}+\vec{k}_{ex}),v\vec{k}}I_{v'\vec{k}',c'(\vec{k}'+\vec{k}_{ex})},\end{aligned}$$
$$(4.18)$$

where the integral $I_{n'\vec{k}',n\vec{k}}$ is written in terms of eigenvectors from the TB Hamiltonian:

$$\begin{aligned}I_{n'\vec{k}',n\vec{k}} =& \langle\psi_{n'\vec{k}'}|\psi_{n\vec{k}}\rangle\\ =& \sum_i (C_{i\vec{k}'}^{n'})^* C_{i\vec{k}}^n\end{aligned}$$
$$(4.19)$$

and $U(\vec{k}-\vec{k}')$ is the Fourier transform of the Coulomb potential, given by:

$$U(\vec{k}-\vec{k}') = -\frac{e^2}{2\epsilon_0}\frac{1}{|\vec{k}-\vec{k}'|(1+r_0|\vec{k}-\vec{k}'|)}\frac{1}{\epsilon_d}, \qquad (4.20)$$

where ϵ_d is the environment dielectric constant, r_0 is the screening length. As we only focus on direct exciton here, we adopt the center-of-mass momentum $\vec{k}_{ex} = 0$ and use only the direct interaction K^d in Eq. 4.18.

4.5   Optical Spectrum

Our ultimate goal is to calculate the optical response: macroscopic dielectric function (ω), or the directly related optical conductivity $\theta(\omega)$, a measurable quantity. The calculation of optical properties is considerably more complicated since momentum matrix elements (MMEs) between initial and final states in the entire first BZ are needed in addition to the band structure. This complication was circumvented by the 'substitution' of $\mathbf{p}\rightarrow(m_0/\hbar)\nabla_k H$ (m_0 being the free-electron mass), which relates the momentum operator to the Hamilton operator. Hence, once the matrix elements of H are determined from a fit to the experimental band structure or a first principles calculation, the MMEs are readily available.

We start with the usual light-matter interaction Hamiltonian H_{LM}, described by:

$$H_{LM} = -\frac{e}{mc}\mathbf{A}(\mathbf{r}) \cdot \hat{p}, \qquad (4.21)$$

where $\mathbf{A}(\mathbf{r})$ is vector potential for the electromagnetic field in the Coulomb gauge, $\hat{p}$ is the momentum operator, e and m are electron charge and mass, respectively, and c is light speed. The vector potential can be written as $\mathbf{A}(\mathbf{r}) = \sqrt{\frac{2\pi\hbar c}{Vq}}(e^{i\mathbf{q}\cdot\mathbf{r}}\hat{a}_{\lambda,\mathbf{q}}\,\mathbf{n}_{\lambda,\mathbf{q}} + h.c.)$, where V is the volume of system, $\hat{a}_{\lambda\mathbf{q}}$ is photon annihilation operator, λ, $\mathbf{q}$ and $\mathbf{n}_{\lambda,\mathbf{q}}$ are the light mode, wavenumber and unit vector along light polarization direction, respectively. We calculate the real part of the diagonal, linear optical sheet conductivity tensor for the exciton combination from an exciton state $|\Psi_S(\mathbf{Q}),0\rangle$ to the final ground state $|G,1_{\lambda\mathbf{q}}\rangle$ (the second term in the states gives the photon state), is given by:

$$Re\theta_{xx}(\lambda\mathbf{q}) = \frac{2\pi}{\hbar}\sum_{\lambda\mathbf{q}}|\langle G,1_{\lambda\mathbf{q}}|H_{LM}|\Psi_S(\mathbf{Q}),0\rangle|^2\delta(E_S(\mathbf{Q}) - E_{\lambda\mathbf{q}}), \qquad (4.22)$$

where $E_S(\mathbf{Q})$ and $E_{\lambda\mathbf{q}}$ are the energies of the exciton and photon, respectively, δ is the delta function. The term $\langle G,1_{\lambda\mathbf{q}}|H^{LM}|\Psi_S(\mathbf{Q}),0\rangle$ can be extended as:

$$\begin{aligned}
&\langle G,1_{\lambda\mathbf{q}}|H_{LM}|\Psi_S(\mathbf{Q}),0\rangle \\
=&\langle G|\left[-\frac{e}{mc}\sqrt{\frac{2\pi\hbar c}{Vq}}e^{-i\mathbf{q}\cdot\mathbf{r}}\mathbf{n}_{\lambda,\mathbf{q}}\cdot\hat{p}\right]\sum_{c,v,\mathbf{k}}A^S_{c,v,\mathbf{k},\mathbf{Q}}|c,\mathbf{k}+\mathbf{Q}\rangle \\
&\otimes|v,\mathbf{k}\rangle \\
\approx&-\frac{e}{m}\sqrt{\frac{2\pi\hbar}{cVq}}\mathbf{n}_{\lambda,\mathbf{q}}\cdot\sum_{c,v,\mathbf{k}}A^S_{c,v,\mathbf{k},\mathbf{Q}}\langle c,\mathbf{k}+\mathbf{Q}|\hat{p}|v,\mathbf{k}\rangle,
\end{aligned} \qquad (4.23)$$

where the long wavelength approximation, $e^{-i(\mathbf{k}\cdot\mathbf{r})} \approx 1$, is adopted. For a two-dimensional material assuming in the xy plane, due to momentum conservation, the in-plane components of the photon wavenumber $\mathbf{q} = (q_x, q_y, q_z)$ and the 2D exciton momentum $\mathbf{Q} = (Q_x, Q_y, 0)$ are equal. Since the photon momentum is small in comparison with the size of the Brillouin zone, we can safely approximate optical transition element as follows,

$$\langle c,\mathbf{k}+\mathbf{Q}|\hat{p}|v,\mathbf{k}\rangle \approx \langle c,\mathbf{k}|\hat{p}|v,\mathbf{k}\rangle\delta_{q_x,Q_x}\delta_{q_y,Q_y} \qquad (4.24)$$

Substituting the above matrix elements in Eq. 4.22, simplifying the term $\sum_{\mathbf{q}}$ using the two delta functions δ_{q_x,Q_x} and δ_{q_y,Q_y}. Then we arrive at that,

$$\begin{aligned}
Re\theta_{xx}(\lambda\mathbf{q}) =&\frac{4\pi^2e^2}{m^2cV}\sum_{\lambda q_z}\frac{1}{q}|\mathbf{n}_{\lambda,\mathbf{q}}\cdot\sum_{c,v,\mathbf{k}}A^S_{c,v,\mathbf{k},\mathbf{Q}}\langle c,\mathbf{k}|\hat{p}|v,\mathbf{k}\rangle|^2 \\
&\times\delta(E_S(\mathbf{Q}) - E_{\mathbf{q}\lambda}) \\
=&\frac{4\pi^2e^2}{m^2cV}\sum_{\lambda}\frac{L_z}{2\pi}|\sum_{c,v,\mathbf{k}}A^S_{c,v,\mathbf{k},\mathbf{Q}}\langle c,\mathbf{k}|\hat{p}_\parallel|v,\mathbf{k}\rangle|^2 \\
&\times\int_{-\infty}^{\infty}dq_z\frac{1}{q}|\mathbf{n}_{\lambda,\mathbf{q}}\cdot(\hat{x}+\hat{y})|^2\delta(E_S(\mathbf{Q}) - q\hbar c),
\end{aligned} \qquad (4.25)$$

where $\hat{x}$ and $\hat{y}$ are unit vectors along the x-axis and y-axis, respectively, $\hat{p}_\parallel$ is the momentum operator in an arbitrary in-plane direction, the sum on q_z is transformed to an integral, employing

the identity $\sum\limits_{q_z} = \frac{L_z}{2\pi} \int_{-\infty}^{\infty} dq_z$ with L_z being the plane-normal length ($V = A_\parallel L_z$ is the volume, $A_\parallel$ being the in-plane area). With the two delta functions, we have $\mathbf{q} = (Q_x, Q_y, q_z)$. As $\mathbf{Q} = (Q_x, Q_y, 0)$, we get $q = \sqrt{Q^2 + q_z^2}$. By introducing a unit vector $\hat{u}$ in the $x = y$ direction in $x - y$ plane, i.e., $\hat{u} = (\hat{x} + \hat{y})/\sqrt{2}$ [180], we can rewrite the term $\mathbf{n}_{\lambda,\mathbf{q}} \cdot (\hat{x} + \hat{y}) = \sqrt{2}\mathbf{n}_\lambda, \mathbf{q} \cdot \hat{u}$. We choose two components of the polarization direction unit vector $\mathbf{n}_\mathbf{q}$, $\mathbf{n}_\perp$ perpendicular to the $\mathbf{q} - \hat{u}$ plane, and $\mathbf{n}_\parallel$ in the $\mathbf{q} - \hat{u}$ plane with a angle θ between $\mathbf{n}_\parallel$ and $\hat{u}$. Then we get $\mathbf{n}_\parallel \cdot \hat{u} = \cos\theta$, $\mathbf{q} \cdot \hat{u} = q\sin\theta$ and $\mathbf{n}_\perp \cdot \hat{u} = 0$, which means that $\mathbf{n}_\perp$ does not contribute to the exciton lifetime. Thus we obtain:

$$
\begin{aligned}
\sum_\lambda |\mathbf{n}_{\lambda,\mathbf{q}} \cdot (\hat{x} + \hat{y})|^2 &= 2|\mathbf{n}_\parallel \cdot \hat{u}|^2 \\
&= 2\cos^2\theta \\
&= 2\left[1 - (\frac{\mathbf{q} \cdot \hat{u}}{q})^2\right] \\
&= \frac{2}{q^2}\left[q^2 - \frac{(q_x + q_y)^2}{2}\right],
\end{aligned}
\tag{4.26}
$$

where we use $\mathbf{q} \cdot \hat{u} = (q_x + q_y)\sqrt{2}$. Substituting Eq. 4.26 into Eq. 4.25, we get:

$$
\begin{aligned}
&\sum_\lambda \int_{-\infty}^{\infty} dq_z \frac{1}{q}|\mathbf{n}_{\lambda,\mathbf{q}} \cdot (\hat{x} + \hat{y})|^2 \delta(E_S(\mathbf{Q}) - q\hbar c) \\
&= \int_{-\infty}^{\infty} dq_z \frac{2}{q^3}[q^2 - \frac{(q_x + q_y)^2}{2}]\delta(E_S(\mathbf{Q}) - q\hbar c) \\
&= \int_{-\infty}^{\infty} dq_z \frac{2q_z^2 + (Q_x - Q_y)^2}{(q_z^2 + Q^2)^{3/2}}\delta(E_S(\mathbf{Q}) - (q_z^2 + Q^2)^{1/2}\hbar c) \\
&= \int_{-\infty}^{\infty} dq_z \frac{2q_z^2 + (Q_x - Q_y)^2}{(E_S(\mathbf{Q})\hbar c)^3} \\
&= \frac{2\hbar^2 c^2}{E_S^2(\mathbf{Q})}\left[2\sqrt{\frac{E_S^2(\mathbf{Q})}{\hbar^2 c^2} - Q^2} + \frac{(Q_x - Q_y)^2}{\sqrt{\frac{E_S^2(\mathbf{Q})}{\hbar^2 c^2} - Q^2}}\right] \equiv I(\mathbf{Q}),
\end{aligned}
\tag{4.27}
$$

where we use $q_x = Q_x$, $q_y = Q_y$, and $q^2 = q_z^2 + Q^2$ in the third line; use the property of delta function in the forth line; and define this integral term as $I(\mathbf{Q})$. Then we have:

$$
\begin{aligned}
&\langle c, \mathbf{k}|\hat{p}_\parallel|v, \mathbf{k}\rangle \\
&= \langle c, \mathbf{k}|(\frac{\partial H^{TB}(\mathbf{k})}{\partial \mathbf{k}})|v, \mathbf{k}\rangle \\
&= \frac{1}{\sqrt{N}}\sum_\mathbf{R} e^{i\mathbf{k}\cdot\mathbf{R}}\langle W_{c\mathbf{R}}|[\sum_{ij}\sum_{\mathbf{R}'''}(-i\mathbf{k}\cdot\mathbf{R}''')e^{-i\mathbf{k}\cdot\mathbf{R}'''} \\
&\quad t_{ij}(\mathbf{R}''')\hat{a}_{i0}^\dagger\hat{a}_{j\mathbf{R}'''}] \times \frac{1}{\sqrt{N}}\sum_{\mathbf{R}'} e^{-i\mathbf{k}\cdot\mathbf{R}'}|W_{v\mathbf{R}'}\rangle \\
&= \frac{1}{N}\sum_\mathbf{R}(-i\mathbf{k}\cdot\mathbf{R})e^{-i\mathbf{k}\cdot\mathbf{R}}t_{cv}(\mathbf{R}),
\end{aligned}
\tag{4.28}
$$

where we use the commutation relation $\hat{p} = (im_e/\hbar)[\mathbf{H}, \mathbf{k}] = \partial\mathbf{H}/\partial\mathbf{k}$. Then we get the final form

for exciton lifetime:

$$Re\theta_{xx}(\lambda\mathbf{q}) = \frac{4\pi e^2}{m^2 cAN^2}|\sum_{c,v,\mathbf{k}} A^S_{c,v,\mathbf{k},\mathbb{Q}}\frac{1}{N}\sum_{\mathbf{R}}(-i\mathbf{k}\cdot\mathbf{R})e^{-i\mathbf{k}\cdot\mathbf{R}}$$

$$\times t_{cv}(\mathbf{R})|^2 I(\mathbf{Q}) \qquad (4.29)$$

$$= \frac{4\pi e^2}{m^2 cAN^2}\mu^2_S(\mathbf{Q})I(\mathbf{Q}),$$

where we define the square modulus of the BSE exciton transition dipole element $\mu^2_S(\mathbf{Q}) \equiv |\sum_{c,v,\mathbf{k}} A^S_{c,v,\mathbf{k},\mathbb{Q}}\frac{1}{N}\sum_{\mathbf{R}}(-i\mathbf{k}\cdot\mathbf{R})e^{-i\mathbf{k}\cdot\mathbf{R}}t_{cv}(\mathbf{R})|^2$. In our calculation, we studied the recombination of direct excitons located within the light cone nearby the K point, where $I(0) = \frac{2\hbar c}{E_S(0)}$ and $Re\theta_{xx}(\lambda\mathbf{q}, Q=0) = \frac{8\pi\hbar e^2}{m^2 E_S(0)AN^2}\mu^2_S(0)$. Considering the temperature factor, we use the relationship $\langle\tau_{0,T}\rangle = \tau_0 \cdot \frac{3M_S c^2 k_B T}{2E^2_S(0)}$ [180], where M_S is the exciton mass, k_B is the Boltzmann constant and T is the temperature.

4.6 Optical properties of excitons in 2D Heterostructures

Apart from the excellent properties of Dirac cones in graphene and its derivatives, the weak SOC and zero band gap have limit its application in optical-electronic devices such as field effect transistors (FET). As a result, transition metal chalcogenides (TMDs), namely MX_2 (M = Mo, W; X = S, Se, Te), represented by MoS_2, have semiconductor properties with unique advantages [181]. The suitable band gaps in TMDs have a wide range of applications in photocatalytic, photovoltaic, optoelectronic and spintronic devices. TMDs have attracted great interest for optics, optoelectronics, and information technology. They are direct-gap semiconductors with two inequivalent valleys located at the K and K' points of the hexagonal BZ. Not only that, the van der Waals (vdW) layered structure composed of TMDs has weak van der Waals interaction between the layers not only can maintain the unique characteristics of their respective monolayers, but also the type II band-alignment characteristics exhibited by the electronic properties lead to the generation of photoexcitation. Therefore, the electrons and holes are distributed in different monolayers and generate long-lived photoexcited carriers, which greatly increases the application of vdW materials of TMDs in photovoltaic devices. Coupling also brings more novel physical properties [182].

The feature of the bright or dark ground-state exciton plays a significant role in light emission processes. For instance, in Mo-based TMDs, the ground-state exciton is a bright exciton, but it is a dark exciton in W-based TMDs [183]. Consequently, the former are optically bright monolayers, while the latter are dark ones. On the other hand, the character of the excitons is governed by the ordering of the spin states in CB and VB bands. Hence, switching the ordering of the spin states would bring out a change of exciton character (bright or dark) in the TMDs, which will give rise to a dramatic change in light emission processes.

Generating and manipulating valley polarization (VP) closely associated with valley splitting (VS), is a critical first step toward valleytronics applications. Dynamical VP has been achieved by either optical pumping or optical stark effect, where the circularly polarized light can preferentially create excitons in one valley, generating a difference in the population of the two valley excitons.

Such property offers a new paradigm for optoelectronic devices. As dynamical VP is based on optical excitation to create a transient nonequilibrium photo-carrier distribution in the two valleys, the extremely short carrier lifetime severely limits the manipulation of the valley degree of freedom. An alternative route to VP is to lift the valley degeneracy by magnetic proximity effects (MPE) in 2D materials on ferromagnetic (FM) substrates. Various FM substrates have been explored, including europium sulfide (EuS), europium oxide (EuO), manganese oxide (MnO), manganese dioxide (MnO_2), yttrium iron garnet (YIG), chromium triiodide (CrI_3), chromium tribromide ($CrBr_3$), VSe_2 and $Cr_2Ge_2Te_6$ et al [184]. Among these substrats, the 2D FM insulators (CrI_3, $CrBr_3$, VSe_2 and $Cr_2Ge_2Te_6$) have attracted more attention, due to their large contact surfaces and an elimination of lattice mismatch. However, the exchange field-induced VS is typically small ≈ 2 meV/T, strongly potential for the valley device applications.

In this chapter, we report a mechanism for producing a giant VS in semiconductor layered material/CrI_3 heterostructures. By using TiXY/CrI_3 (X/Y = Br, I) heterostructures as prototypical systems, we reveal the underlying mechanism. The large difference in work functions between TiXY and CrI_3 generates an atypical type-III band alignment. Namely, the CB edges of CrI_3 fall into the VBs of the TiXY, favoring electron transfer from the latter to the former and hybridization between them. The charge transfer creates a fully spin-polarized 2D electron gas and emergent ferromagnetism at the interface. We demonstrate that the hybridization together with interlayer magnetic exchange interaction between TiXY and FM substrate can produce very strong MPE, giving rise to a giant VS. Additionally, the VS exhibits a strong polarity of TiXY crystal structure and stacking configuration dependence. Interestingly, such MPE drives a switch of spin-band ordering of TiXY CB in the vicinity of K and K' points.

To construct stable hybrid TiBrI/CrI_3, $TiBr_2$/CrI_3, and TiI_2/CrI_3 heterostructures, the 2H monolayer TiBrI, $TiBr_2$ and TiI_2 were relaxed firstly, using a 2×2 supercell, and the corresponding crystallographic constants are set as the same as lattice constant of monolayer CrI_3, 7.10 Å. For the Janus TiBrI/CrI_3 heterostructure, six possible stacking configurations, denoted by Br_1, Br_2, Br_3, I_1, I_2 and I_3, were considered. Among them, the former three stacking configurations (Br_1, Br_2 and Br_3) were created with the underneath Br atoms in upper layer. The latter three (I_1, I_2 and I_3) were obtained by exchanging the positions of Br and I atoms of the upper layer, as shown in Fig. 4.6.
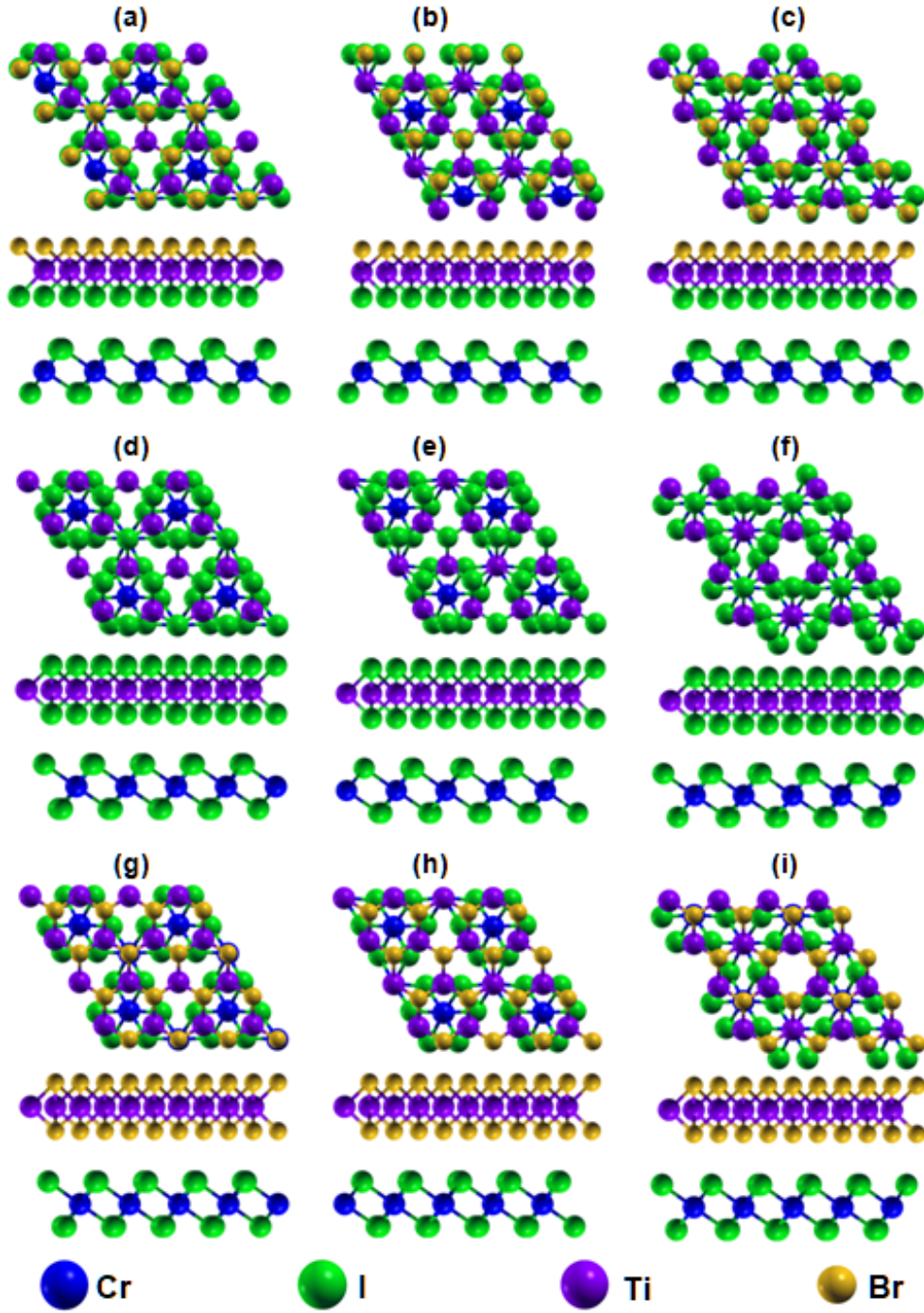
Figure 4.6: The schematic structure of top- (upper row) and side- (lower row) views for TiBrI/CrI$_3$, TiI$_2$/CrI$_3$ and TiBr$_2$/CrI$_3$ heterostructures, with stacking configuration of I$_1$ (a), I$_2$ (b), I$_3$ (c), I$_1$1 (d), I$_1$2 (e), I$_1$3 (f), Br$_1$1 (g), Br$_1$2 (h) and Br$_1$3 (i).

We have selected four typical stacking configurations such as Br$_1$, I$_1$, Br$_1$1 and I$_1$1, where Br$_1$1 and I$_1$1 stand for TiX$_2$/CrI$_3$, and their corresponding layer and spin projected band structures are shown in Fig. 4.7. The effect of SOC is considered in the band structure spectra. Notice that the monolayer TiBrI has an indirect band gap of 0.69 eV, which is consistent with the literature. SOC leads to a spin-orbit splitting of 70 meV in the VB and 28 meV in the CB. Because of an

inversion asymmetry of atomic structure and time reversal symmetry (TRS), TiBrI exhibits a unique spin-valley locked band structure. MPE and VS depend strongly on stacking configuration, that exchange field induced by MPE breaks Kramer's degeneracy of K and K' valley of TiBrI, giving rise to VS determined by:

$$\Delta_{KK'}^{v/c} = E_K^{v/c,\downarrow} - E_{K'}^{v/c,\uparrow} \tag{4.30}$$

Fig. 4.7shows that the VS in Janus TiBrI/CrI$_3$ with Br$_1$ stacking is 59 meV, while it is only 25 meV in corresponding conventional TiBr$_2$/CrI$_3$ with Br$_{11}$ stacking. Therefore, the polarity of TiBrI stemming from the difference in electronegativity between Br and I atoms enlarges VS. While the VS is 16 meV for TiBrI/CrI$_3$ with I$_1$ stacking configuration, it is 110 meV for TiI$_2$/CrI$_3$ with I$_{11}$, the opposite polarity reduces VS. Therefore, the stacking configuration together with the crystal structure polarity can significantly tune VS in TiBrI/CrI$_3$. Therefore it comes to the conclusion that in addition to the stacking configuration, the crystal structure polarity also strongly impacts the magnitude of VS.
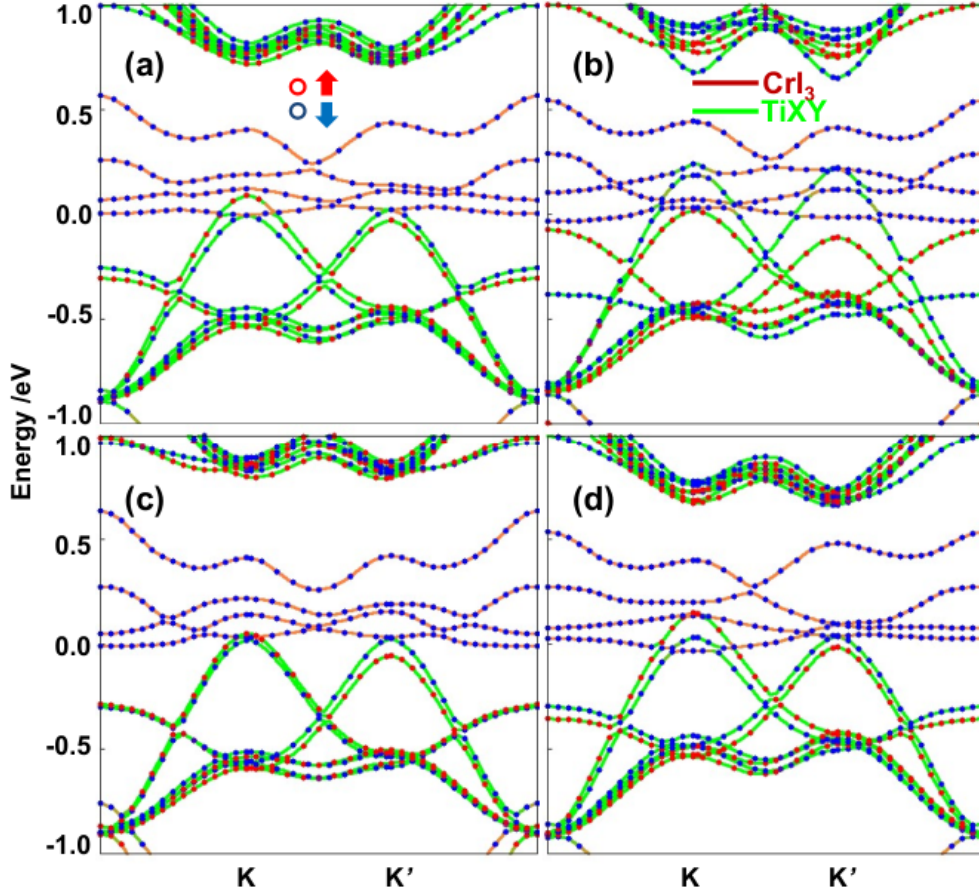
Figure 4.7: (a)–(d) Layer and spin projected band structures of Br$_1$, I$_1$, Br$_{11}$ and I$_{11}$ with spin-orbit coupling. The red and blue circles correspond to spin-up and spin-down bands, while the green and orange curves represent TiXY and CrI$_3$ layers, respectively.

As shown in Fig. 4.7(a), no hybridization is allowed between the states of CrI$_3$ and TiBrI with opposite spins. Consequently, no anticrossing is observed. Hence, the VB dispersion at $_K$ and

K' points is like that of freestanding TiBrI. The magnetic proximity effect, however, breaks the TRS, leading to opposite shifts of the VBs in the K and K' valleys; i.e., it enlarges the spin-orbit splitting in the K valley, while it reduces the spin-orbit splitting in the K valley. A smaller shift in the CB is also observed. A giant valley splitting of 59 meV, defined as the difference of the exciton transition energies in the K and K' valleys, respectively, is obtained, which is 20 plus times higher than that reported for WSe_2/CrI_3.

The charge transfer is very pronounced in TiI_2/CrI_3, an average electron transfer being equal to 0.319 e. On the other hand, a less pronounced average charge transfer of 0.160 e occurs in $TiBr_2/CrI_3$. Therefore, TiI_2/CrI_3 exhibits a larger valley splitting (110 meV) than that (25 meV) of $TiBr_2/CrI_3$, where the very pronounced average charge transfer giving rise to a strong exchange interaction, enhancing the VS.

A giant magnetic proximity effect induces a switch of spin-up and spin-down CBs ordering. In the freestanding TiBrI, the lowest two CBs are spin-up and spin-down in the K valley. The energy separation between them is due to the SOC. In the K' valley, TRS requires spin splitting with the same magnitude, but an opposite sign. In $TiBrI/CrI_3$ heterostructures, the orbital angular momentum in CB is equal to zero. Thus, the Zeeman shift arises mainly from the interaction between the magnetic dipole of electron spin and a magnetic field. For Br stacking, the FM exchange interaction always lowers the energy of the spin-up bands and raises the spin-down bands. Thus, the spin-orbit splitting enlarges in the K valley and shrinks in the K valley, leading to valley contrasting behavior. For the magnetic exchange interaction energy being larger than the SOC of CB, the ordering of the spin-split bands is reversed in the K' valley, while there are no ordering changes in the K valley. Eventually, the lowest CB in the K and K' valleys has the same spin state (spin-up). For I stacking, however, the FM exchange interaction lowers the energy of the spin-down bands while raising the spin-up bands. Then the lowest CBs will have the same spin state such as spin-down in both K and K' valleys for a strong magnetic exchange field. From Figs. 4.7(a) and 4.7(b), we notices that the lowest CB state for both Br and I stackings has the same spin state in K and K' valleys. This implies that magnetic exchange interaction energy induced by magnetic proximity effect has overcome the SOC gap and brings about a switch of character of the lowest CB.

Now let us come to the exciton picture. The VS in magneto-PL was evaluated, considering the contributions of CB splitting, VB splitting, and exciton binding energy. We assume that the excitation laser is linearly polarized. For simplification purposes, we also suppose that there is no intervalley scattering. Fig. 4.8 displays valley selective σ^+ (red) and σ^- (green) light emissions for freestanding (M = 0) monolayer TiXY [(a2)–(d2), the middle panels] and $TiXY/CrI_3$ heterostructures (the top and bottom panels) with Br_1, I_1, Br_{11} and I_{11} stacking. The photon-excited electron (hole) relaxes to the CB (VB) local minimum (maximum) located near (at) either the K or K' point through a multiphoton scattering process, where the bright exciton in the K or K' valley forms. The former emits σ^+ polarized light, while the latter emits the σ^- one, as illustrated by red and green arrows in Fig. 4.8. As expected, without the magnetic substrate, the σ^+ and σ^- emission peaks coincide because of the valley degeneracy protected by TRS. The MPE induced by the CrI_3 substrate is manifested clearly in (a1)–(d1) for $\theta = \pi/2$ and (a3)–(d3) for $\theta =$

$\pi/2$, which corresponds to out-of-plane magnetization of CrI$_3$ with the field direction downwards and upwards, respectively. Notice that, when deposited on CrI$_3$ substrate, the single emission peak of freestanding monolayer TiXY in (a2)–(d2) splits into σ^+ and σ^- polarized emissions, which occurs in the K and K' valleys, respectively. Hence, it exhibits a valley optical selectivity, as photons do not carry significant momentum; therefore, they cannot selectively populate different valleys based on this attribute. In addition, for magnetization aligned along the $+z$ direction ($\theta = \pi/2$), the σ^+ peak exhibits a redshift, while the σ^- peak shows a blueshift with a giant peak separation, corresponding to a VS of 85.11 meV for Br$_1$, 319.15 meV for I$_1$, 51.06 meV for Br$_{11}$, and 110.63 meV for I$_{11}$, respectively. It is noteworthy to recall that these values of VS correspond to the difference of exciton energy in the K and K' valleys. Hence, these VSs depends not only on single-particle band structure but also excitonic states. Then a discrepancy between the values estimated by means of BSE and by single-particle picture (see the VS values in previous sections) is expected. Interestingly, the σ^+ and σ^- peaks move to an opposite direction for $\theta = \pi/2$, producing an opposite value of VS. In addition, because the MPE breaks the valley degeneracy, the σ^+ and σ^- peaks show different intensities, which endues this 2D heterostructure material with optical emission polarization. The variation of PL intensity,
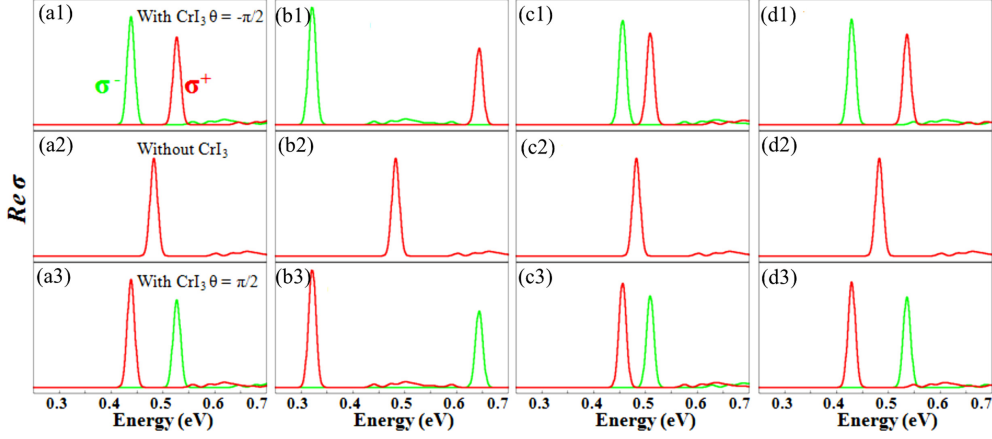
Figure 4.8: Emission spectra of (a) Br$_1$, (b) I$_1$, (c) Br$_{11}$, and (d) I$_{11}$, excited by σ^+ (red) and σ^- (green) circularly polarized lights. The middle panels (a2), (b2), (c2), and (d2) correspond to zero-field emission spectrum of freestanding monolayers, and top panels (a1)–(d1) and bottom panels (a3)–(d3) depict the emission spectra of samples deposited on CrI$_3$ with an out-of-plane angle $\theta = \pi/2$ and $\theta = -\pi/2$, respectively, where θ is the angle between exchange field and sample plane.

Chapter 5

Exciton-Phonon Couplings

This chapter presents the calculation of exciton-phonon coupling, which is the most important part during the optical scattering process.

5.1 Introduction

Electron-phonon interactions determine the temperature dependence of transport behaviors such as electron mobility in semiconductors, inducing conventional low-temperature superconductivity that can function in topological materials [185]. In addition, electron-phonon interactions can also affect the dynamics of phonons through the Berry phase term from electrons, which may eventually lead to the so-called phonon Hall effect [185]. Straightforwardly, the electron-phonon interaction can be understood as the local charge imbalance caused by this lattice distortion drags down the electrons in motion when phonons are excited in the crystal. In contrast, from the phonon's point of view, the electrons in motion are dragging the phonons at the same time, and they compete with each other for dynamic equilibrium. As a result, electrons and phonons are always coupled to each other, making it difficult to rigorously solve their equations of motion.

The exciton-phonon interaction is another fundamental physical problem that plays a crucial role in condensed matter physics. For example, exciton-phonon coupling can excite the production of Cooper pairs, thereby realizing the superconducting properties of ionic materials; it also dominates the dynamic characteristics of photogenerated carriers. Monolayer transition metal dichalcogenides can achieve ultra-strong exciton resonance due to their ultra-high Coulomb attraction and weak electromagnetic shielding [184]. Therefore, excitons dominate the linear and nonlinear optical and electrical effects of monolayer transition metal dichalcogenides [184]. One of the most significant is the exciton-phonon coupling effect. In Raman spectroscopy, the presence of exciton effect will significantly enhance the resonance of its phonons, thus achieving strong Raman peaks. On the other hand, two-dimensional materials can perfectly combine with other materials to form new heterogeneous crystals due to their large specific surface area. It is possible that the resonance effect of excitons is transmitted to the surface of the material to which it is bound via van der Waals forces.

In fact, it has been found that the strong resonance of excitons can excite new phonon modes in

heterojunction materials. As shown in Fig. 5.1, Du et al. combined few-layer tungsten diselenide with boron nitride to form a heterojunction structure, and used a 532 nm laser to excite the excitonic properties of tungsten diselenide, thereby clearly observing nitrogen [9]. The ZO phonon resonance of boron nitride material cannot be detected in pure boron nitride [9]. This strong exciton-phonon resonance effect not only enables Raman enhancement, but also facilitates a better understanding of the physical mechanism of phonons.
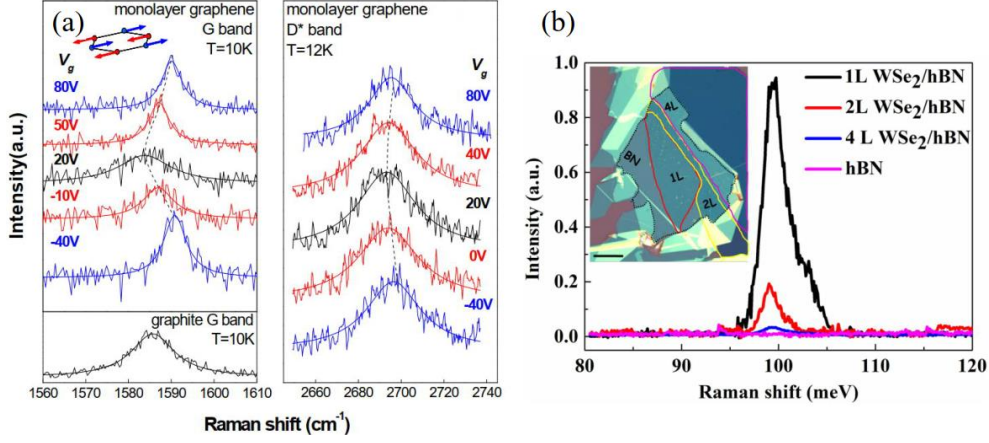
Figure 5.1: (a) Gate-tuned graphene Raman spectroscopy; (b) Exciton coupling-enhanced phonon resonance of boron nitride [9].

The fluctuation of the exciton energy level comes from the coupling of electrons or holes with phonons, The fluctuation of the exciton energy level comes from the exciton-phonon coupling. Fig. 5.2 shows the Fourier transform of the exciton energy level. The amplitude of the energy level oscillation represents the strength of the coupling, which can be characterized by the peak value of the Fourier transform. The peak position gives the coupled phonon type. In Fig. 5.2(b), it can be seen that the optical mode A_1 near 400 cm^{-1} and the acoustic phonons near 200 cm^{-1} contribute to a certain extent, and the distribution of these coupled phonons is consistent with the form previously discussed in the heterojunction [186]. In addition, smaller peak positions can be seen around 600 cm^{-1} and 700 cm^{-1}, which are a mixture of the optical phonon A_1 and the above-mentioned acoustic phonon. The middle Fourier transform shows the phonons coupled to the exciton levels. The main phonon mode peaks are still around 400 cm^{-1} and 200 cm^{-1}, while the phonon peaks around 600 cm^{-1} and 700 cm^{-1} are significantly improved. This originates from the excitons themselves, which are bound by the electron-hole interaction.
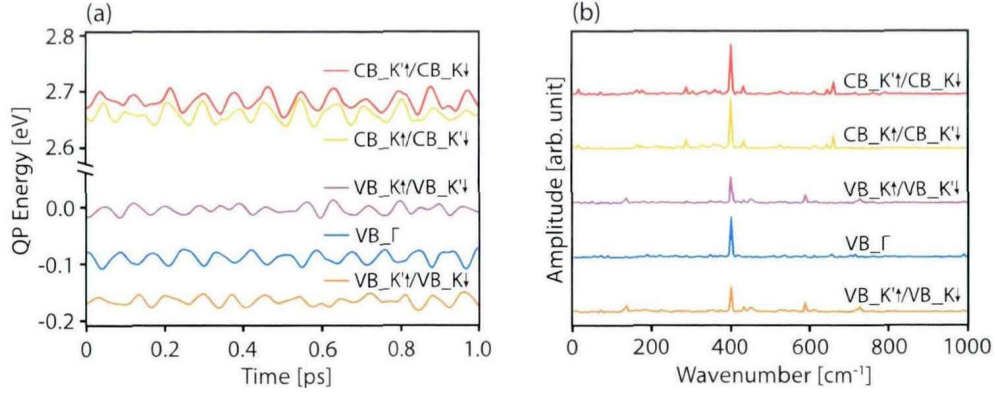
Figure 5.2: Time-dependent evolution of exciton energy levels and its Fourier transform

The scattering of electrons by zone-center optical and intervalley phonons in semiconductor crystals has been treated rather extensively by many authors. In particular, the polar optical-phonon interaction was treated by Frohlich [187], Callen [188] and Ehrenreich [189]. Consideration of the nonpolar optical interaction with electrons was carried out by Seitz and Harrison. The nonpolar optical interaction is important for intravalley scattering as well as being utilized for scattering of electrons (or holes) between different minima of the conduction (or valence) band. This latter interaction is important for scattering of carriers in semiconductors with many-valley band structure, and also in the Gunn effect, where scattering occurs between different sets of equivalent minima. Harrison pointed out that the nonpolar optical matrix element may be either of zero or higher order in the wave vector of the phonon. In subsequent treatments of electron transport in which the nonpolar interaction is important, only the zero-order term has been considered, generally owing to the impression that the higher-order terms are much smaller. Although this is usually the case, there arise many cases in which the zero-order term is forbidden by the symmetry of the states involved.

5.2   Exciton-Phonon Coupling

We now turn to the exciton-phonon interaction in the phonon-assisted transition process. Here we choose the single layer MoS_2 as an example. Let us define the perturbed BSE Hamiltonian as $\tilde{H}$. We write the matrix element of $\tilde{H}$:

$$\tilde{H}_{\tilde{v}\tilde{c},\tilde{v}'\tilde{c}'} = \langle \tilde{v}\tilde{c}|\tilde{H}|\tilde{v}'\tilde{c}'\rangle = (e_{\tilde{c}} - e_{\tilde{v}})\delta_{\tilde{v}\tilde{v}'}\delta_{\tilde{c}\tilde{c}'} + \tilde{K}_{\tilde{v}\tilde{c},\tilde{v}'\tilde{c}'} \tag{5.1}$$

where $\tilde{K}_{vc,v'c'}$ is the perturbed BSE kernel. We define the unperturbed single-particle wave function as $|\phi\rangle$ and the perturbed one as $|\tilde{\phi}\rangle$ with the relationship between the two:

$$\begin{aligned}|\tilde{\phi}^n\rangle =& |\phi^n\rangle + \delta|\phi^n\rangle \\ =& |\phi^n\rangle + \sum_{n'\neq n}\Delta_{n'n}|\phi^{n'}\rangle\end{aligned} \tag{5.2}$$

with

$$\Delta_{n'n} = \frac{\langle \phi^n|\Delta V|\phi^{n'}\rangle}{e_{n'} - e_n}, \tag{5.3}$$

$$\Delta V = \sum_{\kappa \alpha p} \frac{\partial V^{KS}}{\partial u_{\kappa \alpha p}} \cdot u_{\kappa \alpha p} \tag{5.4}$$

where $u_{\kappa \alpha p}$ is the static atomic displacements of the atom κ in the unit cell p along the direction α. and can be expressed in terms of the ladder operators as follows:

$$u_{\kappa \alpha p} = \left(\frac{M_0}{N_p M_\kappa} \right)^{1/2} \sum_{\vec{q}\lambda} e^{i\vec{q}\cdot\vec{R}_p} \varepsilon_{\kappa \alpha, \lambda}(\vec{q}) \iota_{\vec{q}\lambda} (\hat{b}_{\vec{q}\lambda} + \hat{b}^\dagger_{-\vec{q}\lambda}), \tag{5.5}$$

where $\iota_{\vec{q}\lambda} = [\hbar/(2M_0\omega_{\vec{q}\lambda})]^{1/2}$ is the 'zero-point' displacement amplitude, $\varepsilon_{\kappa \alpha, \lambda}(\vec{q})$ is the phonon eigenmode, M_0 is an arbitrary reference mass which is introduced to ensure that $\iota_{\vec{q}\lambda}$ has the dimensions of a length and is similar in magnitude to $u_{\kappa \alpha p}$, M_0 is the nuclear mass, $\hat{b}_{\vec{q}\lambda}/\hat{b}^\dagger_{-\vec{q}\lambda}$ is the annihilation/creation operator of a phonon with momentum $\vec{q}$ and phonon mode λ, and V^{KS} is the Kohn-Sham potential, given by a Taylor expansion about the equilibrium positions:

$$V^{KS}(u_{\kappa p}) = V_0^{KS} + \delta_V + \mathcal{O}[u_{\kappa p}]^2, \tag{5.6}$$

Following Merzbacher's work [190], we define the lattice-periodic functions:

$$\partial_{\kappa \alpha} \upsilon^{KS} = \sum_i e^{-i\vec{q}\cdot(\vec{r}-\vec{R}_i)} \frac{\partial V^{KS}}{\partial u_{\kappa \alpha}}\big|_{\vec{r}-\vec{R}_i}, \tag{5.7}$$

$$\Delta_{\vec{q}\lambda} \upsilon^{KS} = \iota_{\vec{q}\lambda} \sum_{\kappa \alpha} \frac{M_0}{M_s}^{1/2} \varepsilon_{\kappa \alpha, \lambda}(\vec{q}) \partial_{\kappa \alpha} \upsilon^{KS}, \tag{5.8}$$

and we get the derivative of the Kohn-Sham potential:

$$\Delta_{\vec{q}\lambda} V^{KS} = e^{i\vec{q}\cdot\vec{r}} \Delta_{\vec{q}\lambda} \upsilon^{KS} \tag{5.9}$$

Substituting Eq. 5.5 - 5.9 into Eq. 5.4, we get the change in potential as a sum of phonon interactions [179]:

$$\Delta V = \sum_{\vec{q}\lambda} \left(\frac{\hbar}{2M\omega_{\vec{q}\lambda}} \right)^{1/2} \Delta_{\vec{q}\lambda} V^{KS} (\hat{b}_{\vec{q}\lambda} + \hat{b}^\dagger_{-\vec{q}\lambda}) \tag{5.10}$$

Therefore the transition in Eq. 5.3 for a periodic system can be written as:

$$\begin{aligned}
\Delta_{n\vec{k},n'\vec{k}'} &= \frac{\langle n'\vec{k}'|\Delta V|n\vec{k}\rangle}{e_{n\vec{k}} - e_{n'\vec{k}'}} \\
&= \frac{\langle n'\vec{k}'| \sum_{\vec{q}\lambda} \left(\frac{\hbar}{2M\omega_{\vec{q}\lambda}} \right)^{1/2} \Delta_{\vec{q}\lambda} V^{KS} (\hat{b}_{\vec{q}\lambda} + \hat{b}^\dagger_{-\vec{q}\lambda}) |n\vec{k}\rangle}{e_{n\vec{k}} - e_{n'\vec{k}'}} \\
&= \sum_{\vec{q}\lambda} \left(\frac{\hbar}{2M\omega_{\vec{q}\lambda}} \right)^{1/2} \frac{\langle n'\vec{k}'|\Delta_{\vec{q}\lambda} V^{KS}|n\vec{k}\rangle}{e_{n\vec{k}} - e_{n'\vec{k}'}} (\hat{b}_{\vec{q}\lambda} + \hat{b}^\dagger_{-\vec{q}\lambda}) \\
&= \sum_{\vec{q}\lambda} \frac{g_{nn'\lambda}(\vec{k},\vec{q}) \delta_{(\vec{k}'-\vec{k}-\vec{q})}}{e_{n\vec{k}} - e_{n'\vec{k}'}} (\hat{b}_{\vec{q}\lambda} + \hat{b}^\dagger_{-\vec{q}\lambda}),
\end{aligned} \tag{5.11}$$

where we define electron-phonon matrix element $g_{nn'\lambda}(\vec{k},\vec{q}) = \left(\frac{\hbar}{2M\omega_{\vec{q}\lambda}} \right)^{1/2} \langle n'\vec{k}'|\Delta_{\vec{q}\lambda} V^{KS}|n\vec{k}\rangle$, meaning the probability amplitude for an electron in band n with crystal momentum $\vec{k}$ to be

scattered to band n' with momentum $\vec{k}'$ by absorbing/emitting a phonon with mode index λ and wave vector $\vec{q}$, M being the formula weight of MoS$_2$

We solve the unperturbed BSE Hamiltonian H and obtain the exciton energy E_n and wave function $|X^n\rangle$. However the perturbed BSE Hamiltonian is not solved directly, but to first order it provides the exciton-phonon interactions we aim to derive. Here we project the perturbed BSE Hamiltonian onto the unperturbed basis set and keep terms of first-order in the phonon perturbation [191], and the additional term in $\tilde{H}$, compared with H, is attributed to the exciton-phonon interaction. We use the tilde for physical quantities of the perturbed system. As the correction of electron energies is of second order, we will use $e_i = \tilde{e}_i$.

Firstly, we project the perturbed BSE Hamiltonian onto the unperturbed basis set, and get the matrix element:

$$
\begin{aligned}
\tilde{H}_{m\vec{k}_{ex},m'\vec{k}'_{ex}} &= \langle X^{m',\vec{k}_{ex}}|\tilde{H}|X^{m',\vec{k}'_{ex}}\rangle \\
&= \sum_{vc,v'c'} \langle X^{m,\vec{k}_{ex}}|vc\rangle\langle vc|\tilde{H}|v'c'\rangle\langle v'c'|X^{m',\vec{k}'_{ex}}\rangle \\
&= \sum_{vc,v'c'} \sum_{\tilde{v}\tilde{c},\tilde{v}'\tilde{c}'} \langle X^{m,\vec{k}_{ex}}|vc\rangle\langle vc|\tilde{v}\tilde{c}\rangle\langle \tilde{v}\tilde{c}|\tilde{H}|\tilde{v}'\tilde{c}'\rangle\langle \tilde{v}'\tilde{c}'|v'c'\rangle\langle v'c'|X^{m',\vec{k}'_{ex}}\rangle
\end{aligned}
\tag{5.12}
$$

where we insert the complete unperturbed basis sets $\sum_{vc}|vc\rangle\langle vc| = \sum_{v'c'}|v'c'\rangle\langle v'c'| = 1$ and perturbed basis sets $\sum_{\tilde{v}\tilde{c}}|\tilde{v}\tilde{c}\rangle\langle\tilde{v}\tilde{c}| = \sum_{\tilde{v}'\tilde{c}'}|\tilde{v}'\tilde{c}'\rangle\langle\tilde{v}'\tilde{c}'| = 1$. With the BSE wave function $\langle X^{m,\vec{k}_{ex}}|vc\rangle = A_{vc}^{(m,\vec{k}_{ex})*}$ and $\langle v'c'|X^{m',\vec{k}'_{ex}}\rangle = A_{v'c'}^{(m',\vec{k}'_{ex})}$, Eq.5.12 can be written as,

$$
\begin{aligned}
\tilde{H}_{m\vec{k}_{ex},m'\vec{k}'_{ex}} &= \sum_{vc,v'c'} A_{vc}^{(m,\vec{k}_{ex})*} A_{v'c'}^{(m',\vec{k}'_{ex})} \sum_{\tilde{v}\tilde{c},\tilde{v}'\tilde{c}'} \langle vc|\tilde{v}\tilde{c}\rangle\langle\tilde{v}\tilde{c}|\tilde{H}|\tilde{v}'\tilde{c}'\rangle\langle\tilde{v}'\tilde{c}'|v'c'\rangle \\
&= \sum_{vc,v'c'} A_{vc}^{(m,\vec{k}_{ex})*} A_{v'c'}^{(m',\vec{k}'_{ex})} \sum_{\tilde{v}\tilde{c},\tilde{v}'\tilde{c}'} \langle vc|\tilde{v}\tilde{c}\rangle \left[(\tilde{e}_{\tilde{c}} - \tilde{e}_{\tilde{v}})\delta_{\tilde{v}\tilde{v}'}\delta_{\tilde{c}\tilde{c}'} + \tilde{K}_{\tilde{v}\tilde{c},\tilde{v}'\tilde{c}'} \right] \langle\tilde{v}'\tilde{c}'|v'c'\rangle \\
&= \sum_{vc,v'c'} A_{vc}^{(m,\vec{k}_{ex})*} A_{v'c'}^{(m',\vec{k}'_{ex})} \left[\sum_{\tilde{v}\tilde{c}} \langle vc|\tilde{v}\tilde{c}\rangle(\tilde{e}_{\tilde{c}} - \tilde{e}_{\tilde{v}})\langle\tilde{v}\tilde{c}|v'c'\rangle + \sum_{\tilde{v}\tilde{c},\tilde{v}'\tilde{c}'} \langle vc|\tilde{v}\tilde{c}\rangle\tilde{K}_{\tilde{v}\tilde{c},\tilde{v}'\tilde{c}'}\langle\tilde{v}'\tilde{c}'|v'c'\rangle \right]
\end{aligned}
\tag{5.13}
$$

Now let us focus on the two terms in brackets and calculate them separately, and the first part is:

$$
\sum_{\tilde{v}\tilde{c}} \langle vc|\tilde{v}\tilde{c}\rangle(\tilde{e}_{\tilde{c}} - \tilde{e}_{\tilde{v}})\langle\tilde{v}\tilde{c}|v'c'\rangle = \sum_{\tilde{v}\tilde{c}} (e_{\tilde{c}} - e_{\tilde{v}})\langle vc|\tilde{v}\tilde{c}\rangle\langle\tilde{v}\tilde{c}|v'c'\rangle
\tag{5.14}
$$

where we use $e_i = \tilde{e}_i$ as we described above that the correction of electron energies is of second order. With Eq. 5.2, we insert $\tilde{v} = |v''\rangle + \sum_{v'''\neq v''}\Delta_{v''v'''}|v'''\rangle$ and $\tilde{c} = |c''\rangle + \sum_{c'''\neq c''}\Delta_{c''c'''}|c'''\rangle$ to expand Eq. 5.14 to order $\mathcal{O}(\Delta)$ and we get:

$$
\begin{aligned}
\langle vc|\tilde{v}\tilde{c}\rangle &= \langle v|\tilde{v}\rangle\langle c|\tilde{c}\rangle \\
&= (\delta_{vv''} + \sum_{v'''\neq v''}\Delta_{v''v'''}\delta_{vv'''})(\delta_{cc''} + \sum_{c'''\neq c''}\Delta_{c''c'''}\delta_{cc'''}) \\
&= \delta_{vv''}\delta_{cc''} + \delta_{cc''}\sum_{v'''\neq v''}\Delta_{v''v'''}\delta_{vv'''} + \delta_{vv''}\sum_{c'''\neq c''}\Delta_{c''c'''}\delta_{cc'''} + \mathcal{O}(\Delta^2),
\end{aligned}
\tag{5.15}
$$

62

$$\langle \tilde{v}\tilde{c}|v'c'\rangle = \langle v'|\tilde{v}\rangle^* \langle c'|\tilde{c}\rangle^*$$

$$= \delta_{v'v''}\delta_{c'c''} + \delta_{c'c''}\sum_{v'''\neq v''}\Delta^*_{v''v'''}\delta_{v'v'''} + \delta_{v'v''}\sum_{c'''\neq c''}\Delta^*_{c''c'''}\delta_{c'c'''} + \mathcal{O}(\Delta^2) \quad (5.16)$$

With neglecting $\mathcal{O}(\Delta^2)$ items in above results, Eq. 5.14 can be written as:

$$\sum_{\tilde{v}\tilde{c}}(\tilde{e}_{\tilde{c}} - \tilde{e}_{\tilde{v}})\langle vc|\tilde{v}\tilde{c}\rangle\langle \tilde{v}\tilde{c}|v'c'\rangle$$

$$\approx (e_c - e_v)\delta_{vv'}\delta_{cc'} + \delta_{cc'}\sum_{v''}(e_c - e_{v''})\sum_{v'''\neq v''}(\Delta^*_{v''v'''}\delta_{v'v'''}\delta_{vv''} + \Delta_{v''v'''}\delta_{vv'''}\delta_{v'v''})$$

$$+ \delta_{vv'}\sum_{c''}(e_{c''} - e_v)\sum_{c'''\neq c''}(\Delta^*_{c''c'''}\delta_{c'c'''}\delta_{cc''} + \Delta_{c''c'''}\delta_{cc'''}\delta_{c'c''}) \quad (5.17)$$

$$= (e_c - e_v)\delta_{vv'}\delta_{cc'} + \delta_{cc'}[(e_c - e_v)\Delta^*_{vv'} + (e_c - e_{v'})\Delta_{v'v}]$$

$$+ \delta_{vv'}[(e_c - e_v)\Delta^*_{cc'} + (e_{c'} - e_v)\Delta_{c'c}]$$

With the relation $\Delta_{ij} = -\Delta^*_{ji}$, we have:

$$\sum_{\tilde{v}\tilde{c}}(e_{\tilde{c}} - e_{\tilde{v}})\langle vc|\tilde{v}\tilde{c}\rangle\langle \tilde{v}\tilde{c}|v'c'\rangle = (e_c - e_v)\delta_{vv'}\delta_{cc'} + \delta_{cc'}(e_v - e_{v'})\Delta_{v'v} + \delta_{vv'}(e_{c'} - e_c)\Delta_{c'c} \quad (5.18)$$

We use the approximation $\tilde{K}_{\tilde{v}\tilde{c},\tilde{v}'\tilde{c}'} \approx \langle \tilde{v}\tilde{c}|K|\tilde{v}'\tilde{c}'\rangle$ for the second item in Eq. 5.13, as the effect of the atomic displacements on the bare and screened Coulomb interactions can be neglected:

$$\sum_{\tilde{v}\tilde{c},\tilde{v}'\tilde{c}'}\langle vc|\tilde{v}\tilde{c}\rangle\tilde{K}_{\tilde{v}\tilde{c},\tilde{v}'\tilde{c}'}\langle \tilde{v}'\tilde{c}'|v'c'\rangle \approx \sum_{\tilde{v}\tilde{c},\tilde{v}'\tilde{c}'}\langle vc|\tilde{v}\tilde{c}\rangle\langle \tilde{v}\tilde{c}|K|\tilde{v}'\tilde{c}'\rangle\langle \tilde{v}'\tilde{c}'|v'c'\rangle$$

$$= \langle vc|K|v'c'\rangle \quad (5.19)$$

$$= K_{vc,v'c'}$$

When we substitute the above results into Eq. 5.13, we get:

$$\tilde{H}_{m\vec{k}_{ex},m'\vec{k}'_{ex}} = \sum_{vc,v'c'}A^{(m,\vec{k}_{ex})*}_{vc}A^{(m',\vec{k}'_{ex})}_{v'c'}[(e_c - e_v)\delta_{vv'}\delta_{cc'} + \delta_{cc'}(e_v - e_{v'})\Delta_{v'v} + \delta_{vv'}(e_{c'} - e_c)\Delta_{c'c} + K_{vc,v'c'}]$$

$$= \sum_{vc,v'c'}A^{(m,\vec{k}_{ex})*}_{vc}A^{(m',\vec{k}'_{ex})}_{v'c'}[(e_c - e_v)\delta_{vv'}\delta_{cc'} + K_{vc,v'c'}]$$

$$+ \sum_{vc,v'c'}A^{(m,\vec{k}_{ex})*}_{vc}A^{(m',\vec{k}'_{ex})}_{v'c'}[\delta_{cc'}(e_v - e_{v'})\Delta_{v'v} + \delta_{vv'}(e_{c'} - e_c)\Delta_{c'c}]$$

$$(5.20)$$

where the first term in the second line, is equal to:

$$\sum_{vc,v'c'}A^{(m,\vec{k}_{ex})*}_{vc}A^{(m',\vec{k}'_{ex})}_{v'c'}[(e_c - e_v)\delta_{vv'}\delta_{cc'} + K_{vc,v'c}]$$

$$= \sum_{vc,v'c'}A^{(m,\vec{k}_{ex})*}_{vc}A^{(m',\vec{k}'_{ex})}_{v'c'}H_{vc,v'c'} = \sum_{vc}A^{(m,\vec{k}_{ex})*}_{vc}\sum_{v'c'}H_{vc,v'c'}A^{(m',\vec{k}'_{ex})}_{v'c'} = H_{m\vec{k}_{ex},m'\vec{k}'_{ex}} \quad (5.21)$$

Eq. 5.20 and Eq. 5.21 are the perturbed and unperturbed Hamiltonian, respectively, therefore the second term in the third line of Eq. 5.20 is the exciton-phonon interaction,

$$
\begin{aligned}
H_{ex-ph} &= \sum_{m\vec{k}_{ex},m'\vec{k}'_{ex}} \sum_{vc,v'c'} A_{vc}^{(m,\vec{k}_{ex})*} A_{v'c'}^{(m',\vec{k}'_{ex})} \left[\delta_{cc'}(e_v - e_{v'})\Delta_{v'v} + \delta_{vv'}(e_{c'} - e_c)\Delta_{c'c} \right] \hat{c}^\dagger_{m\vec{k}_{ex}} \hat{c}_{m'\vec{k}'_{ex}} \\
&= \sum_{m\vec{k}_{ex},m'\vec{k}'_{ex}} \sum_{vc\vec{k},v'c'\vec{k}'} A_{vc\vec{k}}^{(m,\vec{k}_{ex})*} A_{v'c'\vec{k}'}^{(m',\vec{k}'_{ex})} \left[\delta_{cc'}(e_{v\vec{k}} - e_{v'\vec{k}'})\Delta_{v'\vec{k}',v\vec{k}} + \delta_{vv'}(e_{c'(\vec{k}'+\vec{k}_{ex})} - e_{c(\vec{k}+\vec{k}_{ex})}) \right] \\
&\quad \times \Delta_{c'(\vec{k}'+\vec{k}'_{ex}),c(\vec{k}+\vec{k}_{ex})} \hat{c}^\dagger_{m\vec{k}_{ex}} \hat{c}_{m'\vec{k}'_{ex}} \\
&= \sum_{m\vec{k}_{ex},m'\vec{k}'_{ex}} \sum_{vc\vec{k},v'c'\vec{k}'} A_{vc\vec{k}}^{(m,\vec{k}_{ex})*} A_{v'c'\vec{k}'}^{(m',\vec{k}'_{ex})} \left[-\delta_{cc'} \sum_{\vec{q}\lambda} g_{v'v\lambda}(\vec{k},\vec{q}) + \delta_{vv'} \sum_{\vec{q}\lambda} g_{c'c\lambda}(\vec{k}+\vec{k}_{ex},\vec{q}) \right] \\
&\quad \times \delta_{(\vec{k}-\vec{k}'-\vec{q})}(\hat{b}_{\vec{q}\lambda} + \hat{b}^\dagger_{-\vec{q}\lambda}) \hat{c}^\dagger_{m\vec{k}_{ex}} \hat{c}_{m'\vec{k}'_{ex}} \\
&= \sum_{m\vec{k}_{ex},m'\vec{k}'_{ex}} \sum_{\vec{q}\lambda} \sum_{vc\vec{k}} \left[\sum_{c'} A_{vc\vec{k}}^{(m,\vec{k}_{ex})*} A_{vc'\vec{k}}^{(m',\vec{k}'_{ex})} g_{c'c\lambda}(\vec{k}+\vec{k}_{ex},\vec{q}) - \sum_{v'} A_{vc\vec{k}}^{(m,\vec{k}_{ex})*} A_{v'c(\vec{k}-\vec{q})}^{(m',\vec{k}'_{ex})} g_{v'v\lambda}(\vec{k},\vec{q}) \right] \\
&\quad \times \hat{c}^\dagger_{m\vec{k}_{ex}} \hat{c}_{m'\vec{k}'_{ex}} (\hat{b}_{\vec{q}\lambda} + \hat{b}^\dagger_{-\vec{q}\lambda})
\end{aligned}
$$

(5.22)

where we use the exciton creation ($\hat{c}^\dagger_{m\vec{k}_{ex}}$) and annihilation ($\hat{c}_{m\vec{k}_{ex}}$) operators to build the matrix, relabel all quantities for a periodic system in the second line, and use Eq. 5.11 to introduce the electron-phonon matrix element g in the third line.

In some reports with DFT calculations, the derivative of self-consistent Kohn-Sham potential (which is determined within the density functional perturbation theory calculation, DFPT) is employed as $\Delta_{\vec{q}\lambda}V^{KS}$ in Eq. 5.11 [192]. However, for practical applications, it would be convenient if the DFPT results can be approximated by a simple analytical model. Therefore, we use analytic expressions with the deformation potential approximation for $\Delta_{\vec{q}\lambda}V^{KS}$, which can be simplified by the expressions in the zeroth order (D_0, for intervalley scattering) or the first order (D_1, for intravalley scattering) of deformation potential constant [193]. As there is only intervalley scattering in this paper, then $\langle n'_\zeta \vec{k}' | \Delta_{\vec{q}\lambda}V^{KS} | n_\zeta \vec{k} \rangle = D_0^\zeta$ ($\zeta = c/v$ corresponding to conduction/valence band, here we use the value $D_0^c = 1.4*10^8$ eV/cm and $D_0^v = 1.2*10^8$ eV/cm [194]). Therefore, we get $g_{n_\zeta n'_\zeta \lambda}(\vec{k},\vec{q}) = \left(\frac{\hbar}{2M\omega_{\vec{q}\lambda}} \right)^{1/2} D_0^\zeta$. Then H_{ex-ph} becomes:

$$
\begin{aligned}
H_{ex-ph} &= \sum_{m\vec{k}_{ex},m'\vec{k}'_{ex}} \sum_{\vec{q}\lambda} \sum_{vc\vec{k}} \left[D_0^e \sum_{c'} A_{vc\vec{k}}^{(m,\vec{k}_{ex})*} A_{vc'\vec{k}}^{(m',\vec{k}'_{ex})} - D_0^h \sum_{v'} A_{vc\vec{k}}^{(m,\vec{k}_{ex})*} A_{v'c(\vec{k}-\vec{q})}^{(m',\vec{k}'_{ex})} \right] \left(\frac{\hbar}{2M\omega_{\vec{q}\lambda}} \right)^{1/2} \\
&\quad \times \hat{c}^\dagger_{m\vec{k}_{ex}} \hat{c}_{m'\vec{k}'_{ex}} (\hat{b}_{\vec{q}\lambda} + \hat{b}^\dagger_{-\vec{q}\lambda}) \\
\\
&= \sum_{m\vec{k}_{ex},m'\vec{k}'_{ex}} \sum_{\vec{q}\lambda} G_{m'\vec{k}'_{ex},m\vec{k}_{ex},\vec{q}\lambda} \hat{c}^\dagger_{m\vec{k}_{ex}} \hat{c}_{m'\vec{k}'_{ex}} (\hat{b}_{\vec{q}\lambda} + \hat{b}^\dagger_{-\vec{q}\lambda})
\end{aligned}
$$

(5.23)

where we define $G_{m'\vec{k}'_{ex},m\vec{k}_{ex},\vec{q}\lambda} = \sum_{vc\vec{k}} \left[D_0^e \sum_{c'} A_{vc\vec{k}}^{(m,\vec{k}_{ex})*} A_{vc'\vec{k}}^{(m',\vec{k}'_{ex})} - D_0^h \sum_{v'} A_{vc\vec{k}}^{(m,\vec{k}_{ex})*} A_{v'c(\vec{k}-\vec{q})}^{(m',\vec{k}'_{ex})} \right] \left(\frac{\hbar}{2M\omega_{\vec{q}\lambda}} \right)^{1/2}$ as the exciton-phonon coupling constant.

5.2.1 Mixed Exciton State Due to Exchange Effect

According to optical selection rules, the intermediate state $|n\rangle$ must be a mixture of states with opposite spins due to presence of the exchange interaction between the two states [195, 196, 197], as shown in Fig..
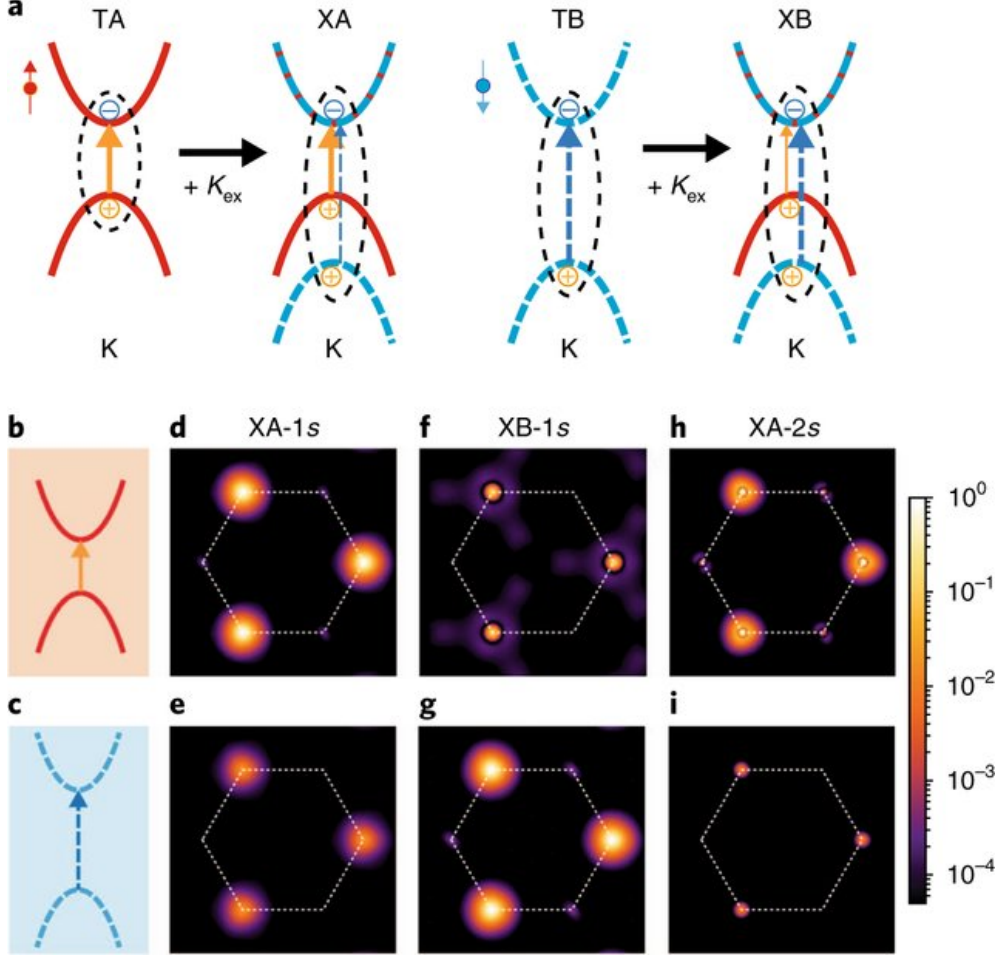
Figure 5.3: Exciton state mixing from the intravalley exchange interaction a, Schematic of exchange-driven mixing of the two spin-polarized Ising excitons, TA and TB, which produces the exciton eigenstates, XA and XB. The solid orange arrows denote the transition between spin-up states (in TA subspace) while the dashed blue arrows denote the transition between spin-down states (in TB subspace). The thicker arrow in the plot of XA or XB indicates the major subspace. Dashed ovals denote the exciton states composed of the corresponding interband transitions. Kex represents the exchange interaction kernel. b,c, Illustration of TA and TB subspaces, respectively. d–i, Log-scale wavefunction amplitudes in k-space (normalized to unity at the highest amplitude for each state) for exciton eigenstates XA-1s (d,e), XB-1s (f,g) and XA-2s (h,i) with the exchange interaction included. The upper (d,f,h) and lower (e,g,i) panels show the projected amplitudes of the wavefunction onto TA and TB subspaces, respectively. [10]

Two exciton states $|X_{K/K'}^{\vec{k}_{ex}}\rangle$ at K/K' valley coupled to each other, as described by the Hamil-

tonian with the basis functions $\{|X_K^{\vec{k}_{ex}}\rangle, |X_{K'}^{\vec{k}_{ex}}\rangle\}$, in terms of the spin-1/2 Pauli matrices:

$$
\begin{aligned}
H_{\vec{Q}} &= \tilde{E}_{\vec{k}_{ex}} + J_{\vec{Q}} \cdot \sigma \\
&= \tilde{E}_{\vec{k}_{ex}} + J_Q(sin\theta cos\phi\sigma_x + sin\theta sin\phi\sigma_y + cos\theta\sigma_z),
\end{aligned}
\tag{5.24}
$$

where $\tilde{E}_{\vec{k}_{ex}}$ is the average energy of two excitons after exchange; Q/ϕ is the magnitude/orientation angle of the center-of-mass momentum $\vec{Q}$; $J_{\vec{Q}}$ is the coupling vector and $J_Q = |J_{\vec{Q}}|$ is the coupling constant [198]; $\sigma_{x/y/z}$ are the Pauli matrix; θ is the polar angle that $\theta \approx \tan^{-1}\left(\frac{|\vec{k}_{ex}|}{\Delta E}\right)$ with ΔE being the energy difference between the two origin excitons [199], made by the energy difference between the valley-uncoupled exciton basis states. Therefore the energy of $|X_{K/K'}^{\vec{k}_{ex}}\rangle$ excitons under inter-valley exchange interaction is:

$$
E_{\vec{k}_{ex}}^{+} = \tilde{E}_{\vec{k}_{ex}} + J_Q,
\tag{5.25}
$$

and

$$
E_{\vec{k}_{ex}}^{-} = \tilde{E}_{\vec{k}_{ex}} - J_Q,
\tag{5.26}
$$

where the subscript '+' and '-' in $E_{\vec{k}_{ex}}^{\pm}$ indicate the higher and lower eigenvalues, respectively, and the corresponding states are:

$$
|X_+^{\vec{k}_{ex}}\rangle = e^{-i\cdot\phi}cos\frac{\theta}{2}|X_K^{\vec{k}_{ex}}\rangle + sin\frac{\theta}{2}|X_{K'}^{\vec{k}_{ex}}\rangle,
\tag{5.27}
$$

and

$$
|X_-^{\vec{k}_{ex}}\rangle = e^{-i\cdot\phi}sin\frac{\theta}{2}|X_K^{\vec{k}_{ex}}\rangle - cos\frac{\theta}{2}|X_{K'}^{\vec{k}_{ex}}\rangle
\tag{5.28}
$$

When the two excitons at different valleys are degenerated, we get the special case with $\theta = \pi/2$, and the states under exchange effect will be:

$$
|X_+^{\vec{k}_{ex}}\rangle = \frac{\sqrt{2}}{2}\left(e^{-i\cdot\phi}|X_K^{\vec{k}_{ex}}\rangle + |X_{K'}^{\vec{k}_{ex}}\rangle\right),
\tag{5.29}
$$

and

$$
|X_-^{\vec{k}_{ex}}\rangle = \frac{\sqrt{2}}{2}\left(e^{-i\cdot\phi}|X_K^{\vec{k}_{ex}}\rangle - |X_{K'}^{\vec{k}_{ex}}\rangle\right)
\tag{5.30}
$$

5.3 DFT Calculations of MoS$_2$

Fig.5.4 shows the orbital-projected band structure of MoS$_2$, and it is found that the top valence band is composed by $d_{x^2-y^2}$ and d_{xy} orbitals of Mo atom, and the bottom conduction band is composed by d_{z^2} orbital of Mo atom. The obtained direct bandgap at the K point is 1.78 eV and 1.66 eV for LDA-PZ and GGA-PBE, respectively, which is also in agreement with previously reported theoretical results.
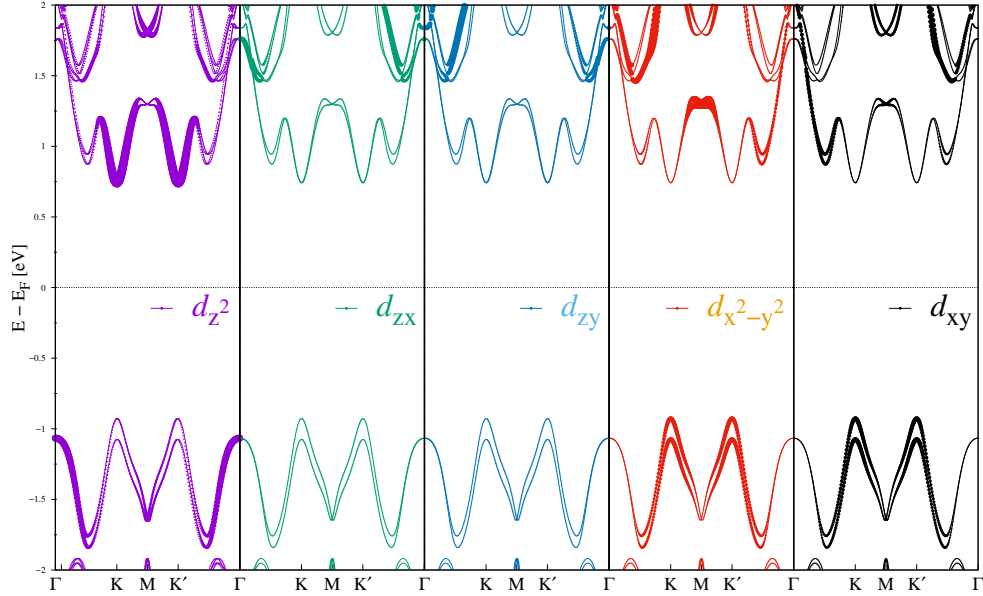
Figure 5.4: Orbital projected band structures for monolayer MoS_2 with SOC. The band structure is calculated on the k-path $\Gamma - K - K$'-Γ and the Fermi energy is set to zero. Symbol size is proportional to its population in corresponding state.

The phonon dispersion has been obtained with the supercell-based small-displacement method using a 2×2 supercell. The resulting phonon dispersion shown in Fig. 5.5 is in excellent agreement with recent calculations of the lattice dynamics in two-dimensional MoS_2. With three atoms in the unit cell, single-layer MoS_2 has nine phonon branches—three acoustic and six optical branches: three acoustic branches with the frequency of the out-of-plane flexural mode being quadratic in $\mathbf{q}$ for $\mathbf{q}{\to}0$, two optical branches and the almost dispersionless phonon at $\approx$50 meV which is the so-called homopolar mode characteristic for layered structures.
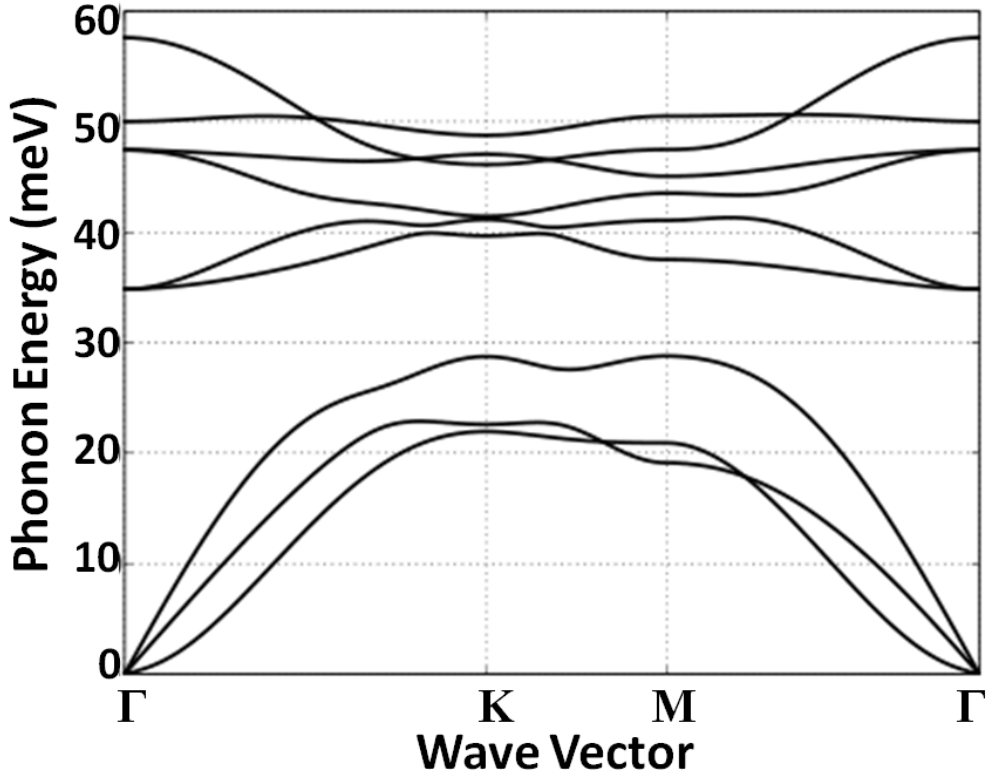
Figure 5.5: Phonon dispersion of single-layer MoS$_2$ calculated with the small displacement method using a 2×2 supercell. The frequencies of the two optical Raman active E$_{2g}$ and A$_{1g}$ modes at 48 meV and 50 meV, respectively, are in excellent agreement with recent experimental measurements.

In the long-wavelength limit, the frequency of the remaining longitudinal acoustic (LA) and transverse acoustic (TA) modes are given by the in-plane sound velocity c_λ:

$$\omega_{\boldsymbol{q}\lambda} = c_\lambda \boldsymbol{q} \tag{5.31}$$

where $\omega_{\boldsymbol{q}\lambda}$ is the frequency of λ mode phonon with wave vector of $\mathbf{q}$. The gap in the Fig. 5.5 completely separates the acoustic and optical branches even at the high symmetry points at the BZ boundary, where the acoustic and optical modes become similar. The two lowest optical branches belong to the non-polar optical modes. The two branches with a phonon energy of ≈48 meV at the Γ-point are the transverse optical (TO) and longitudinal (LO) optical modes, where the Mo and S atoms vibrate in counterphase. Last, the lattice vibration of homopolar mode corresponds to a change in the layer thickness and has the sulfur layers vibrating in counterphase in the direction normal to the layer plane while the Mo layer remains stationary. The change in the potential associated with this lattice vibration has previously been demonstrated to result in a large deformation potential in bulk MoS$_2$.

5.4 Intervalley Scattering between A-excitons at K and K' Valleys of MoS$_2$

Here, we put the inter-valley scattering between the two A-excitons in both valleys on a combined action of the inter-valley exchange coupling between the A-excitons and phonon-assisted intra-band scattering between direct and indirect excitons. Fig. 5.6 schematically illustrates the proposed mechanism: First, a direct A-exciton is excited in the K valley, as the initial state $|i\rangle$ in the mechanics. Second, the exciton $|i\rangle$ scattering with phonon (with frequency ω_e and momenta $\vec{Q}$) creates exciton $|n_a\rangle$ at non-vanishing center of mass momenta, by intra-band scattering. Third, the exciton $|n_a\rangle$ initializes the inter-valley exchange coupling to the unpumped K' valley, to form an exciton $|n_b\rangle$. Finally, the exciton $|n_b\rangle$ scatters to the direct A-exciton $|f\rangle$, under the assistant of phonon with frequency ω'_e and momenta $\vec{Q}$.

Figure 5.6: Schematic illustration of intervalley scattering between A-excitons, at (a) single particle picture and (b) exciton picture.

The two indirect A-excitons at K/K' valley coupled to each other as described by the Hamiltonian with the basis functions $(|n_a^K\rangle, |n_a^{K'}\rangle)$:

$$H_{\vec{Q}} = E_{n_a}\sigma_0 + J_Q\sigma_0 + J_Q[cos(2\phi)\sigma_x + sin(2\phi)\sigma_y], \tag{5.32}$$

where E_{n_a} is the energy of indirect A-exciton, σ_0 and $\sigma_{x/y}$ are the identity matrix and Pauli matrix, respectively; Q/ϕ is the magnitude/orientation angle of the center-of-mass momentum $\vec{Q}$; J_Q is the coupling constant. The intra/inter-valley exchange interaction is described by the second/third term. Therefore the energy of excitonic states under inter-valley exchange interaction is:

$$E_{\tilde{n}_a}^K = E_{n_a} + J_Q \tag{5.33}$$

$$E_{n_b} = E_{n_a} - J_Q, \tag{5.34}$$

and the corresponding states are:

$$|\tilde{n}_a^K\rangle = \frac{e^{-i\phi}}{\sqrt{2}}|n_a^K\rangle + \frac{e^{i\phi}}{\sqrt{2}}|n_a^{K'}\rangle \tag{5.35}$$

$$|n_b\rangle = -\frac{e^{-i\phi}}{\sqrt{2}}|n_a^K\rangle + \frac{e^{i\phi}}{\sqrt{2}}|n_a^{K'}\rangle \qquad (5.36)$$

Therefore the scattering rate of the exciton from $|i\rangle$ state with energy E_i to $|f\rangle$ state with energy E_f can be written as:

$$\frac{1}{\tau_{scat}} = \frac{2}{\hbar}\left|\frac{\langle f|H_{ex-ph}|n_b\rangle\langle n_b|H_{\vec{Q}}|n_a\rangle\langle n_a|H_{ex-ph}|i\rangle}{[E_{n_a} - J_Q - E_{n_b}](E_i - \hbar\omega_e - E_{n_a})}\right|^2$$
$$\times \frac{a}{(E_i - E_f)^2 + a^2}, \qquad (5.37)$$

where a is the parameter in the Lorentz transformation of delta function. And the elements in Eq. 5.37 are:

$$\langle f|H_{ex-ph}|n_b\rangle = \langle A^{K'}|H_{ex-ph}\left(-\frac{e^{-i\phi}}{\sqrt{2}}|n_a^K\rangle + \frac{e^{i\phi}}{\sqrt{2}}|n_a^{K'}\rangle\right)$$
$$= -\frac{e^{-i\phi}}{\sqrt{2}}\langle A^{K'}|H_{ex-ph}|n_a^K\rangle + \frac{e^{i\phi}}{\sqrt{2}}\langle A^{K'}|H_{ex-ph}|n_a^{K'}\rangle \qquad (5.38)$$
$$= e^{i\phi}D_o^e\left(\frac{\hbar}{4M\omega_{\vec{K}}}\right)^{1/2}\sum_{vcc'\vec{k}}\left[A_{vc\vec{k}}^{(A^{K'},0)*}A_{vc'\vec{k}}^{(n_a^{K'},\vec{Q})}\right],$$

where $\langle A^{K'}|H_{ex-ph}|n_a^K\rangle = 0$ in the second line, as the phonons only couple excitons with the same spin state.

$$\langle n_b|H_{\vec{Q}}|n_a\rangle = -\frac{e^{-i\phi}}{\sqrt{2}}\langle n_a^K|H_{\vec{Q}}|n_a^K\rangle + \frac{e^{i\phi}}{\sqrt{2}}\langle n_a^{K'}|H_{\vec{Q}}|n_a^K\rangle$$
$$= -\frac{e^{-i\phi}}{\sqrt{2}}E_{n_a} + \frac{e^{i\phi}}{\sqrt{2}}J_Q[cos(2\phi) - i(2\phi)], \qquad (5.39)$$

$$\langle n_a|H_{ex-ph}|i\rangle = \langle n_a^K|H_{ex-ph}|A^K\rangle$$
$$= \left(\frac{\hbar}{2M\omega_{\vec{Q}}}\right)^{1/2}D_0^e\sum_{vcc'\vec{k}}\left[A_{vc'\vec{k}}^{(n_a^K,\vec{Q})*}A_{vc\vec{k}}^{(A^K,0)}\right], \qquad (5.40)$$

5.5 Intervalley Scattering from B-exciton to A-excitons at Different Valleys of MoS$_2$, Path 1

Figure 5.7 schematically illustrates the proposed mechanism of inter-valley scattering between the B-exciton in K-valley and A-exciton in K'-valley, on a combined action of the inter-valley exchange coupling and phonon-assisted intra-band scattering between direct and indirect excitons: First, a direct B-exciton as the initial state $|i\rangle$, scattering with phonon (with frequency ω_e and momenta $\vec{Q}$), creates indirect exciton $|n_a\rangle$ by intra-band scattering. Second, the exciton $|n_a\rangle$ initializes the inter-valley exchange coupling to the unpumped K' valley, to form an indirect exciton $|n_b\rangle$. Third, the exciton $|n_b\rangle$ scatters to the direct dark B-exciton $|n_c\rangle$, under the assistant of

phonon with frequency ω'_e and momenta $\vec{Q}$. Finally, the dark B-exciton $|n_c\rangle$ relates to bright A-exciton $|f\rangle$, with emitting a photon with frequency ω_h.
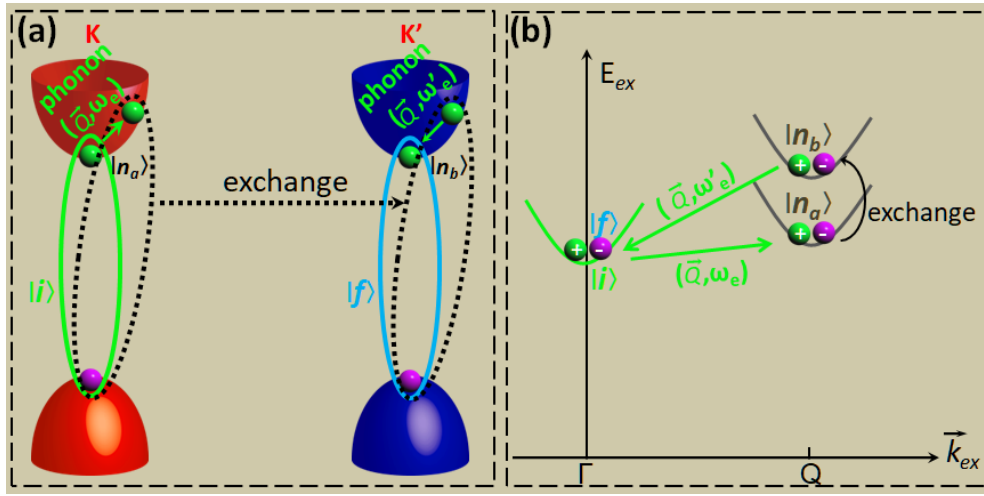

Figure 5.7: Schematic illustration of intervalley scattering from B-exciton to A-excitons, at (a) single particle picture and (b) exciton picture.

The two indirect A-excitons at K/K' valley coupled to each other as described by the Hamiltonian with the basis functions $(|n_a^K\rangle, |n_a^{K'}\rangle)$:

$$H_{\vec{Q}} = E_{n_a}\sigma_0 + J_Q\sigma_0 + J_Q[cos(2\phi)\sigma_x + sin(2\phi)\sigma_y],\qquad(5.41)$$

where E_{n_a} is the energy of indirect B-exciton, σ_0 and $\sigma_{x/y}$ are the identity matrix and Pauli matrix, respectively; Q/ϕ is the magnitude/orientation angle of the center-of-mass momentum $\vec{Q}$; J_Q is the coupling constant. The intra/inter-valley exchange interaction is described by the second/third term. Therefore the energy of excitonic states under inter-valley exchange interaction is:

$$E_{\tilde{n}_a}^K = E_{n_a} + J_Q\qquad(5.42)$$

$$E_{n_b} = E_{n_a} - J_Q,\qquad(5.43)$$

and the corresponding states are:

$$|\tilde{n}_a^K\rangle = \frac{e^{-i\phi}}{\sqrt{2}}|n_a^K\rangle + \frac{e^{i\phi}}{\sqrt{2}}|n_a^{K'}\rangle\qquad(5.44)$$

$$|n_b\rangle = -\frac{e^{-i\phi}}{\sqrt{2}}|n_a^K\rangle + \frac{e^{i\phi}}{\sqrt{2}}|n_a^{K'}\rangle\qquad(5.45)$$

According to the first-order perturbation theory, the intermediate state $|n_c\rangle$ is induced by the

exciton-phonon coupling H_{ex-ph} on direct dark B-exciton $|B_D^{K'}\rangle$:

$$
\begin{aligned}
|n_c\rangle =& |B_D^{K'}\rangle + \frac{\langle n_b|H_{ex-ph}|B_D^{K'}\rangle}{E_B^D - E^{n_b} + \hbar\omega'_e}|n_b\rangle \\
=& |B_D^{K'}\rangle + \frac{\left(-\frac{e^{-i\phi}}{\sqrt{2}}\langle n_a^K| + \frac{e^{i\phi}}{\sqrt{2}}\langle n_a^{K'}|\right) H_{ex-ph}|B_D^{K'}\rangle}{E_B^D - E^{n_b} + \hbar\omega'_e}\left(-\frac{e^{-i\phi}}{\sqrt{2}}|n_a^K\rangle + \frac{e^{i\phi}}{\sqrt{2}}|n_a^{K'}\rangle\right) \\
=& |B_D^{K'}\rangle + \frac{-\left(\frac{\hbar}{M\omega_{\vec{K}}}\right)^{1/2}\left\{\frac{e^{-i\phi}}{2}D_0^e\sum_{vcc'\vec{k}}\left[A_{vc'\vec{k}}^{(n_a^K,\vec{Q})*}A_{vc(\vec{k}+\vec{K})}^{(B_D^K,0)}\right] + \frac{e^{i\phi}}{2}D_0^h\sum_{vv'c\vec{k}}\left[A_{vc'\vec{k}}^{(n_a^{K'},\vec{Q})*}A_{vc\vec{k}}^{(B_D^K,0)}\right]\right\}}{E_B^D - E^{n_b} + \hbar\omega'_e} \\
& \times\left(-\frac{e^{-i\phi}}{\sqrt{2}}|n_a^K\rangle + \frac{e^{i\phi}}{\sqrt{2}}|n_a^{K'}\rangle\right)
\end{aligned}
\tag{5.46}
$$

where $E_D^{K'}$ is the energy of direct dark B-exciton $|B_D^{K'}\rangle$.

Therefore the scattering rate of the exciton from $|i\rangle$ state with energy E_i to $|f\rangle$ state with energy E_f can be written as:

$$
\begin{aligned}
\frac{1}{\tau_{scat}} =& \frac{2}{\hbar}\left|\frac{\langle f|H_{LM}|n_c\rangle\langle n_c|H_{ex-ph}|n_b\rangle\langle n_b|H_{\vec{Q}}|n_a\rangle\langle n_a|H_{ex-ph}|i\rangle}{(E_{n_b} - \hbar\omega'_e - (E_{n_c}))(E_{n_a} + J_Q - E_{n_b})(E_i + \hbar\omega_e - E_{n_a})}\right|^2 \\
& \times \frac{a}{(E_i + \hbar\omega_e + J_Q - \hbar\omega'_e - \hbar\omega_h - E_f)^2 + a^2},
\end{aligned}
\tag{5.47}
$$

where a is the parameter in the Lorentz transformation of delta function. And the elements in Eq. 5.47 are:

$$
\begin{aligned}
\langle n_a|H_{ex-ph}|i\rangle =& \langle n_a^K|H_{ex-ph}|A^K\rangle \\
=& \left(\frac{\hbar}{2M\omega_{\vec{Q}}}\right)^{1/2}D_0^e\sum_{vcc'\vec{k}}\left[A_{vc'\vec{k}}^{(n_a^K,\vec{Q})*}A_{vc\vec{k}}^{(A^K,0)}\right],
\end{aligned}
\tag{5.48}
$$

$$
\begin{aligned}
\langle n_b|H_{\vec{Q}}|n_a\rangle =& -\frac{e^{-i\phi}}{\sqrt{2}}\langle n_a^K|H_{\vec{Q}}|n_a^K\rangle + \frac{e^{i\phi}}{\sqrt{2}}\langle n_a^{K'}|H_{\vec{Q}}|n_a^K\rangle \\
=& -\frac{e^{-i\phi}}{\sqrt{2}}E_{n_a} + \frac{e^{i\phi}}{\sqrt{2}}J_Q[cos(2\phi) - i(2\phi)],
\end{aligned}
\tag{5.49}
$$

$$
\begin{aligned}
\langle n_c | H_{ex-ph} | n_b \rangle = & \langle B_D^{K'} | H_{ex-ph} \left(-\frac{e^{-i\phi}}{\sqrt{2}} | n_a^K \rangle + \frac{e^{i\phi}}{\sqrt{2}} | n_a^{K'} \rangle \right) \\
& - \frac{\left(\frac{\hbar}{M\omega_{\vec{K}}} \right)^{1/2} \left\{ \frac{e^{-i\phi}}{2} D_0^e \sum\limits_{vcc'\vec{k}} \left[A_{vc'\vec{k}}^{(n_a^K,\vec{Q})*} A_{vc(\vec{k}+\vec{K})}^{(B_D^K,0)} \right] + \frac{e^{i\phi}}{2} D_0^h \sum\limits_{vv'c\vec{k}} \left[A_{vc'\vec{k}}^{(n_a^{K'},\vec{Q})*} A_{vc\vec{k}}^{(B_D^K,0)} \right] \right\}}{E_B^D - E^{n_b} + \hbar\omega_e'} \\
& \times \left(-\frac{e^{-i\phi}}{\sqrt{2}} \langle n_a^K | + \frac{e^{i\phi}}{\sqrt{2}} \langle n_a^{K'} | \right) H_{ex-ph} \left(-\frac{e^{-i\phi}}{\sqrt{2}} | n_a^K \rangle + \frac{e^{i\phi}}{\sqrt{2}} | n_a^{K'} \rangle \right) \\
= & - e^{-i\phi} D_o^e \left(\frac{\hbar}{4M\omega_{\vec{K}}} \right)^{1/2} \sum\limits_{vcc'\vec{k}} \left[A_{vc(\vec{k}+\vec{K})}^{(B_D^{K'},0)*} A_{vc'\vec{k}}^{(n_a^K,\vec{Q})} \right] - e^{i\phi} D_o^h \left(\frac{\hbar}{4M\omega_{\vec{Q}}} \right)^{1/2} \\
& \times \sum\limits_{vv'c\vec{k}} \left[A_{vc\vec{k}}^{(B_D^{K'},0)*} A_{v'c\vec{k}}^{(n_a^{K'},\vec{Q})} \right],
\end{aligned}
$$

$$(5.50)$$

$$
\begin{aligned}
\langle f | H_{LM} | n_c \rangle = & \langle f | H_{LM} | B_D^{K'} \rangle - \frac{\left(\frac{\hbar}{M\omega_{\vec{K}}} \right)^{1/2} \left\{ \frac{e^{-i\phi}}{2} D_0^e \sum\limits_{vcc'\vec{k}} \left[A_{vc'\vec{k}}^{(n_a^K,\vec{Q})*} A_{vc(\vec{k}+\vec{K})}^{(B_D^K,0)} \right] + \frac{e^{i\phi}}{2} D_0^h \sum\limits_{vv'c\vec{k}} \left[A_{vc'\vec{k}}^{(n_a^{K'},\vec{Q})*} A_{vc\vec{k}}^{(B_D^K,0)} \right] \right\}}{E_B^D - E^{n_b} + \hbar\omega_e'} \\
& \times \left(-\frac{e^{-i\phi}}{\sqrt{2}} \langle f | H_{LM} | n_a^K \rangle + \frac{e^{i\phi}}{\sqrt{2}} \langle f | H_{LM} | n_a^{K'} \rangle \right) \\
= & - \frac{\left(\frac{\hbar}{M\omega_{\vec{K}}} \right)^{1/2} \left\{ \frac{e^{-i\phi}}{2} D_0^e \sum\limits_{vcc'\vec{k}} \left[A_{vc'\vec{k}}^{(n_a^K,\vec{Q})*} A_{vc(\vec{k}+\vec{K})}^{(B_D^K,0)} \right] + \frac{e^{i\phi}}{2} D_0^h \sum\limits_{vv'c\vec{k}} \left[A_{vc'\vec{k}}^{(n_a^{K'},\vec{Q})*} A_{vc\vec{k}}^{(B_D^K,0)} \right] \right\}}{E_B^D - E^{n_b} + \hbar\omega_e'} \\
& \times \frac{eA_0}{mc} \sum\limits_{vc\vec{k}} \sum\limits_{v'c'} A_{vc\vec{k}}^{(A^{K'},0)*} A_{v'c'\vec{k}}^{(n_a^K,\vec{Q})} \sum\limits_{i}^{N_b} \sum\limits_{i'}^{N_b} c_i^{(v)*}(\vec{k}) c_{i'}^{(v')}(\vec{k}) \sum\limits_{\vec{R}} (iL_a a + L_b b) e^{i\vec{k}\cdot\vec{R}} t_{ii'}(\vec{R})
\end{aligned}
$$

$$(5.51)$$

5.6 Intervalley Scattering from B-exciton to A-excitons at Different Valleys of MoS$_2$, Path 2

Figure 5.8 schematically illustrates the proposed mechanism of inter-valley scattering between the B-exciton in K-valley and A-exciton in K'-valley, on a combined action of phonon-assisted inter-valley and intra-valley scatterings:
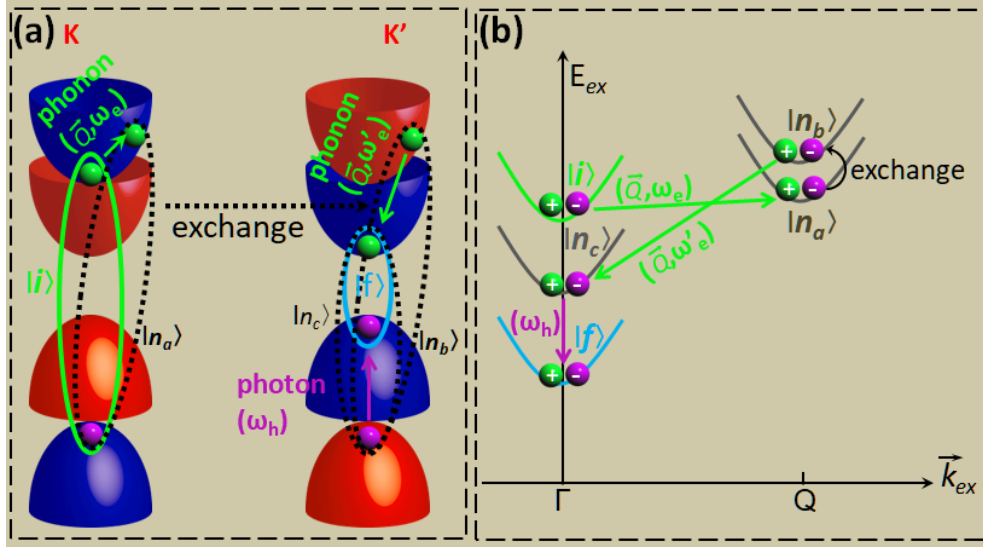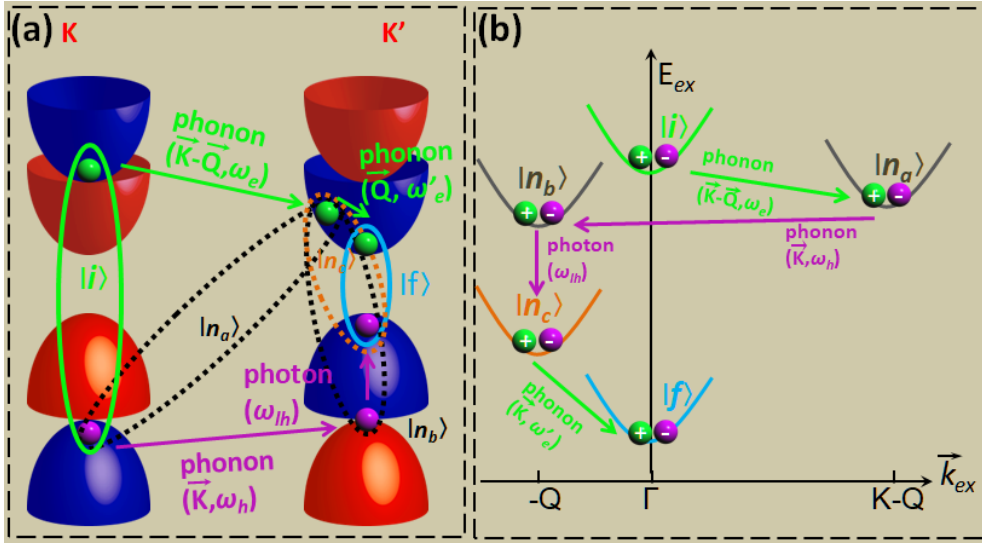
Figure 5.8: Schematic illustration of intervalley scattering between A-excitons, at (a) single particle picture and (b) exciton picture.

First, a direct bright B-exciton $|B_K^{B,0}\rangle$ scatters to a inter-valley exciton $|n_a\rangle$ through the electron-phonon coupling by a phonon with mementum $\vec{K}-\vec{Q}$ and frequency ω_e.

Second, the inter-valley exciton $|n_a\rangle$ scatters to a indirect exciton $|n_b\rangle$ through the electron-hole coupling by a phonon with mementum $\vec{K}$ and frequency ω_h. Due to the opposite spin-states of the two splitting valence bands, the state $|n_b\rangle$ is treated as a hybrid state by exchange effect acted on the two dark excitons $|B_K^{(D,-\vec{Q})}\rangle$ and $|B_{K'}^{(D,-\vec{Q})}\rangle$, as described by the Hamiltonian with the basis functions $(|B_K^{(D,-\vec{Q})}\rangle, |B_{K'}^{(D,-\vec{Q})}\rangle)$:

$$H_{\vec{Q}} = E_{B(D,-\vec{Q})}\sigma_0 + J_Q\sigma_0 + J_Q[cos(2\phi)\sigma_x + sin(2\phi)\sigma_y], \qquad (5.52)$$

where $E_{B(D,-\vec{Q})}$ is the energy of dark excitons $|B_K^{(D,-\vec{Q})}\rangle$, σ_0 and $\sigma_{x/y}$ are the identity matrix and Pauli matrix, respectively; $T_Q = \hbar^2 Q^2/2M$ is the kinetic energy of the center-of-mass motion with M being the total mass of the exciton; Q/ϕ is the magnitude/orientation angle of the center-of-mass momentum $\vec{Q}$; J_Q is the coupling constant. The intra/inter-valley exchange interaction is described by the second/third term. The energy and wavefunction of $|n_b\rangle$ are:

$$E_{n_b} = E_{B(D,-\vec{Q})} - J_Q \qquad (5.53)$$

and

$$|n_b\rangle = -\frac{e^{-i\phi}}{\sqrt{2}}|B_K^{(D,-\vec{Q})}\rangle + \frac{e^{i\phi}}{\sqrt{2}}|B_{K'}^{(D,-\vec{Q})}\rangle \qquad (5.54)$$

respectively.

Third, the dark exciton $|n_b\rangle$ transits to a dark exciton $|n_c\rangle$ through the photon-hole coupling by a photon with frequency ω_{lh}.

Forth, the indirect exciton $|n_c\rangle$ relaxs to the final bright A exciton $|f\rangle$ through the electron-phonon coupling by a phonon with mementum $\vec{Q}$ and frequency ω_e'.

Therefore the scattering rate of the exciton from $|i\rangle$ state with energy E_i to $|f\rangle$ state with energy E_f can be written as:

$$\frac{1}{\tau_{scat}} = \frac{2}{\hbar} \left| \frac{\langle f|H_{ex-ph}|n_c\rangle \langle n_c|H_{LM}|n_b\rangle \langle n_b|H_{ex-ph}|n_a\rangle \langle n_a|H_{ex-ph}|i\rangle}{(E_- E_{n_a} - \hbar\omega_e)(E_{n_a} - E_{n_b} - \hbar\omega_h)(E_{n_b} - E_c - \hbar\omega_{lh})} \right|^2$$
$$\times \frac{a}{(E_i - \hbar\omega_e - \hbar\omega_h - \hbar\omega_{lh} - \hbar\omega'_e - E_f)^2 + a^2}, \tag{5.55}$$

where a is the parameter in the Lorentz transformation of delta function. And the elements in Eq. 5.55 are:

$$\langle f|H_{ex-ph}|n_c\rangle = D_0^e \left(\frac{\hbar}{2M\omega_{\vec{Q}}} \right)^{1/2} \sum_{vcc'\vec{k}} \left[A_{vc'\vec{k}}^{(B_{K'},0)*} A_{vc\vec{k}}^{(n_c,0)} \right] \tag{5.56}$$

$$\langle n_c|H_{LM}|n_b\rangle = \langle n_c|H_{LM} \left(-\frac{e^{-i\phi}}{\sqrt{2}}|B_K^{(D,-\vec{Q})}\rangle + \frac{e^{i\phi}}{\sqrt{2}}|B_{K'}^{(D,-\vec{Q})}\rangle \right)$$
$$= \frac{e^{(1-i\phi)}A_0}{\sqrt{2}mc} \sum_{v'c'} A_{vc\vec{k}}^{(n_c,-\vec{Q})*} A_{v'c'\vec{k}}^{(B_K^D,-\vec{Q})} \sum_{i}^{N_b} \sum_{i'}^{N_b} c_i^{(v)*}(\vec{k})c_{i'}^{(v')}(\vec{k}) \sum_{\vec{R}} (iL_a a + L_b b) e^{i\vec{k}\cdot\vec{R}} t_{ii'}(\vec{R}) \tag{5.57}$$

$$\langle n_b|H_{ex-ph}|n_a\rangle = \left(-\frac{e^{-i\phi}}{\sqrt{2}}\langle B_K^{(D,-\vec{Q})}| + \frac{e^{i\phi}}{\sqrt{2}}\langle B_{K'}^{(D,-\vec{Q})}| \right) H_{ex-ph}|n_a\rangle$$
$$= \frac{e^{-i\phi}}{2} D_0^h \left(\frac{\hbar}{M\omega_{\vec{K}}} \right)^{1/2} \sum_{vv'c\vec{k}} \left[A_{v'c\vec{k}}^{(B_K^D,-\vec{Q})*} A_{vc\vec{k}}^{(n_a,0)} \right] \tag{5.58}$$

and

$$\langle n_a|H_{ex-ph}|i\rangle = D_0^e \left[\frac{\hbar}{2M\omega_{(\vec{K}-\vec{Q})}} \right]^{1/2} \sum_{vcc'\vec{k}} \left[A_{vc'\vec{k}}^{(n_a,\vec{K}-\vec{Q})*} A_{vc\vec{k}}^{(B_K,0)} \right] \tag{5.59}$$

5.7 Scattering Rate

To study the effect of temperature on the scattering rate, we introduce the photon number $n^{\vec{a}}$ and phonon number n_q^λ:

$$n_q^\lambda = \frac{1}{exp(\frac{\hbar\omega}{k_B T}) - 1}, \tag{5.60}$$

where ω is the frequency of phonon, k_B is the Boltzmann constant and T is the temperature. Afterwards, the states will be written in combination form of exciton state, photon number and phonon number $|X\rangle \otimes |n^{\vec{a}};n_{\pm q}^\lambda\rangle$, where the sign $\pm$ indicates the emission/absorption of phonon.

The evolution of scattering rate between A-excitons at different valleys of MoS_2 is shown in Fig. 5.9. It is found that the scattering rate is in range of 0.007-0.0085 ps^{-1}. When the initial energy arrival beyond the energy of the lowest A-exciton, the scattering process occurs between two valleys. Valley scattering processes may strongly influence exciton quantum dynamics, which are characterized by two critical parameters: the population relaxation and decoherence rates. During the total process, two situations must be satisfied, the conservation of energy and the conservation of angular momentum. The energy difference between the initial and final states is replenished

by the absorption/emission of phonon (photon will be involved during the scattering between A-exciton and B-exciton, as the energy difference between the initial and final states is much more the the energy range of phonons). The change of exciton's angular momentum is realized by the interaction with phonon ($\mathbf{Q} \neq 0$). When a carrier collides (electron, hole, exciton et al) with a phonon, both energy and momentum are conserved. Energy and momentum conservation impose constraints on the maximum wave vector change and, therefore, on which phonons may participate in scattering events. The exchange intervalley scattering makes two-valley systems less stable to the spin fluctuations but more stable to the valley fluctuations. It is reported that electron-hole (e-h) exchange interaction can cause the valley depolarization efficiently due to the Maialle-Silva-Sham (MSS) mechanism based on the kinetic spin Bloch equations (KSBEs) [200]. Both the long-range (L-R) and short-rang (S-R) parts of the exchange interactions can cause the inter- and intravalley bright exciton transitions. However, the intravalley bright exciton transition channel is nearly forbidden due to the large splitting of the valence bands and only the intervalley exchange interaction can cause the valley depolarization efficiently. This process can also be treated as the result of virtual recombination of a bright exciton in the K valley and generation in the K valley, or vice versa. Therefore the L-R exchange interaction can cause the fast intervalley exciton transition, which can be further improved by the comparison of scattering rates of the three processes.
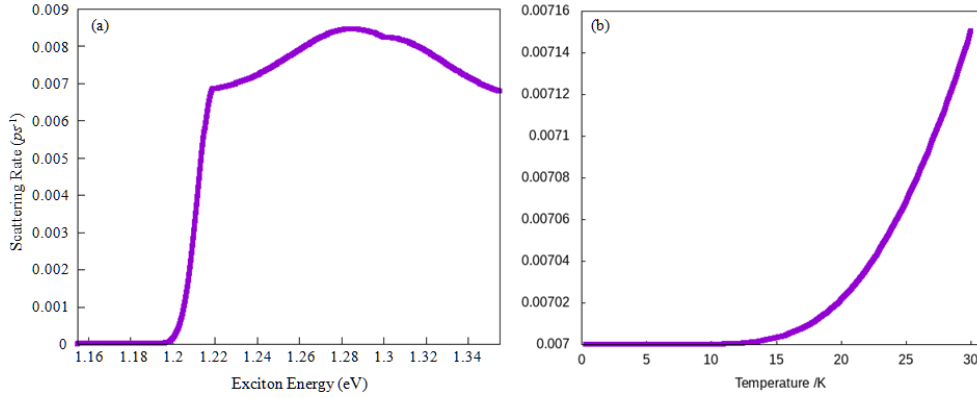
Figure 5.9: The evolution of scattering rate between A-excitons at different valleys of MoS$_2$, as function of (a) initial exciton energy and (b) temperature.

Figure 5.10 shows the comparison of scattering rate of the three processes, as function of the centre-of-mass momentum of the involved indirect exciton $\mathbf{Q}$. It is found that the rate of intervalley scattering by exchange is much faster than that by phonon. This result gives mutual confirmation for the fast emergence of the excitonic signal in the K valley with the A-exciton pumped in K' valley in the experiments [201]. However, for the involved indirect exciton with small center-of-mass momentum, the intervalley exciton transition is relatively slow, which leads to the existence of the residue valley polarization, which lasts for tens of picoseconds in the experiments.
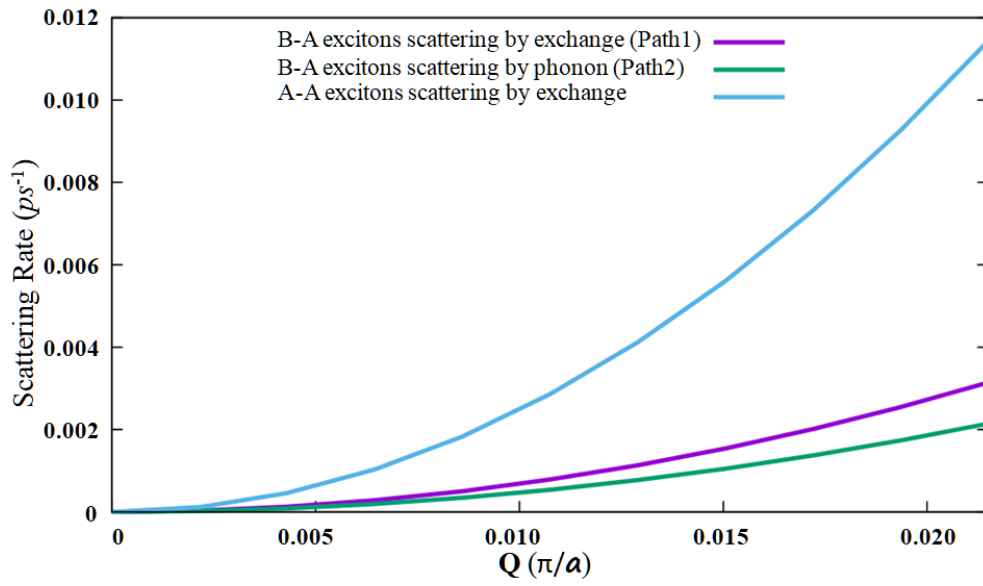
Figure 5.10: Comparison of scattering rate of the three processes, as function of the centre-of-mass momentum of the involved indirect exciton $\mathbf{Q}$

CONCLUSIONS

The topological, electrical and optical properties of 2D materials have been investigated by theory calculation, where borophene, TiBrI and MoS_2 are chosen as the investigated material samples.

To study the effects of topological structure on the electronic properties, we introduce nonsymmorphic symmetry to borophene sheet, by forming periodic defects in the monolayer lattice. By DFT calculaton, we obtain two kinds of nodal lines, some inside the Brillouin zone are accidental to the Rashba SOC; some along the Brillouin zone edge are protected by the nonsymmorphic symmetry and are robust to the Rashba SOC. This result show a very prospective method for fabricating quantum devices operated under electric field, which is also very simple: we just need to remove some atoms to form nonsymmorphic symmetry.

Then we use BSE to calculate the excitons in $TiBrI/CrI_3$ heterostructure. By DFT calculation, we found that the magnetic field from the ferromagnetic substrate CrI_3 has broken the time reversal symmetry, which results in the non-degeneracy between the two valleys. Therefore the valley polarity is formed that the emission light show different energy and intensity under different polarized lights. The relationship between valley polarity and stacking type of heterostructure is investivated by calculating the optical spectrum with exciton energy and wavefunctions. Compared with other methods to fabricate polarity devices, our strategy does not need extra magnetic field, which is very important for the design of chips.

As the scattering of carriers is another important tissue in the carrier dynamics of semiconductors, we investigate the inter-valley scattering of excitons in MoS_2 monolayer. It has been a very hard problem to calculate the scattering of hole, as the energy of phonon is much smaller than the energy splitting at valence bands caused by spin-orbit coupling. We design a physical process including absorption/emission of photon, to achieve the conservation of both energy and momento. The calculation results match well with the reported experimental results.

REFERENCES

[1] LEMME, M. C. Current status of graphene transistors. *Solid State Phenomena*, v. 156, p. 499–509, 2010.

[2] LIU, H. et al. Production of mono-to few-layer mos_2 nanosheets in isopropanol by a salt-assisted direct liquid-phase exfoliation method. *Journal of Colloid and Interface Science*, v. 515, p. 27–31, 2018.

[3] MAK, K. F. et al. Atomically thin mos_2: A new direct-gap semiconductor. *Physical Review Letters*, v. 105, p. 136805, 2010.

[4] LEE, C. et al. Anomalous lattice vibrations of single- and few-layer mos_2. *ACS Nano*, v. 4, p. 2695–2700, 2010.

[5] HONG, X. et al. Ultrafast charge transfer in atomically thin mos_2/ws_2 heterostructures. *Nature Nanotechnology*, v. 9, p. 682–686, 2014.

[6] RADISAVLJEVIC, B. et al. Single-layer mos_2 transistors. *Nature Nanotechnology*, v. 6, p. 147–150, 2011.

[7] BERNARDI, M.; PALUMMO, M.; GROSSMAN, J. C. Extraordinary sunlight absorption and one nanometer thick photovoltaics using two-dimensional monolayer materials. *Nano Letters*, v. 13, p. 3664–3670, 2013.

[8] CHOI, J.-H. et al. Linear scaling of the exciton binding energy versus the band gap of two-dimensional materials. *Phys. Rev. Lett.*, v. 115, p. 066403, 2015.

[9] DU, L. et al. Strongly enhanced exciton-phonon coupling in two-dimensional wse_2. *Phys. Rev. B*, v. 97, p. 235145, 2018.

[10] GUO, L. et al. Exchange-driven intravalley mixing of excitons in monolayer transition metal dichalcogenides. *Nat. Phys.*, v. 15, p. 228–232, 2019.

[11] LUCA, B. et al. Ultrahigh-mobility graphene devices from chemical vapor deposition on reusable copper. *Science Advances*, v. 1, p. e1500222, 2015.

[12] PONOMARENKO, L. A. et al. Effect of a high-κ environment on charge carrier mobility in graphene. *Physical Review Letters*, v. 102, p. 206603, 2009.

[13] ROBINSON, J. A. et al. Correlating raman spectral signatures with carrier mobility in epitaxial graphene: a guide to achieving high mobility on the wafer scale. *Nano Letters*, v. 9, p. 2873–2876, 2009.

[14] NOVOSELOV, K. S. et al. Room-temperature quantum hall effect in graphene. *Science*, v. 315, p. 1379–1379, 2007.

[15] JIANG, Z. et al. Quantum hall effect in graphene. *Solid State Communications*, v. 143, p. 14–19, 2007.

[16] CHEN, e. a. F. On the theory of quantum mechanics. *Chinese Physics B*, v. 25, p. 117106, 2016.

[17] SHUO-YING, e. a. Y. Symmetry demanded topological nodal-line materials. *Advances in Physics: X*, v. 3, p. 1414631, 2018.

[18] QIUNAN, e. a. X. Topological nodal line semimetals in the cap3 family of materials. *Physical Review B*, v. 95, p. 045136, 2017.

[19] A., e. a. P. S. Topological order and absence of band insulators at integer filling in non-symmorphic crystals. *Nature Physics*, v. 9, p. 299–303, 2013.

[20] NOBORU, N. A general survey of the theory of the bethe-salpeter equation. *Progress of Theoretical Physics Supplement*, v. 43, p. 1–81, 1969.

[21] J., e. a. V. Bethe-salpeter equation calculations of core excitation spectra. *Physical Review B*, v. 83, p. 115106, 2011.

[22] L., e. a. M. S. Heat capacity, thermal expansion coefficient, and gruneisen parameter of ch_4, co_2, and c_2h_6 hydrates and ice i_h via density functional theory and phonon calculations. *Crystal Growth Design*, v. 20, p. 5947–5955, 2020.

[23] DIRAC, P. A. M. On the theory of quantum mechanics. *Proceedings of the Royal Society of London. Series A, Containing Papers of a Mathematical and Physical Character*, v. 112, p. 423–437, 1926.

[24] DIRAC, P. A. M. The fundamental equations of quantum mechanics. *Proceedings of the Royal Society of London. Series A, Containing Papers of a Mathematical and Physical Character*, v. 109, p. 642–653, 1925.

[25] DIRAC, P. A. M. Quantum mechanics of many-electron systems. *Proceedings of the Royal Society of London. Series A, Containing Papers of a Mathematical and Physical Character*, v. 123, p. 714–733, 1929.

[26] LENNARD, J.; JOHN, E. Perturbation problems in quantum mechanics. *Proceedings of the Royal Society of London. Series A, Containing Papers of a Mathematical and Physical Character*, v. 129, p. 598–615, 1930.

[27] GURNEY, R. W.; EDWARD, U. C. Quantum mechanics and radioactive disintegration. *Physical Review*, v. 33, p. 127, 1929.

[28] WANG, S. On the asymmetrical top in quantum mechanics. *Physical Review*, v. 34, p. 243, 1929.

[29] ZABUSKY, N. J. Solitons and bound states of the time-independent schrödinger equation. *Physical Review*, v. 168, p. 124, 1968.

[30] SHIMSHOVITZ, A.; J., T. D. Phase-space approach to solving the time-independent schrödinger equation. *Physical Review Letters*, v. 109, p. 070402, 2012.

[31] WANG, Z.; SHAO, H. A new kind of discretization scheme for solving a two-dimensional time-independent schrödinger equation. *Computer Physics Communications*, v. 180, p. 842–849, 2009.

[32] LIU, X. et al. Numerical solution of one-dimensional time-independent schrödinger equation by using symplectic schemes. *International Journal of Quantum Chemistry*, v. 79, p. 343–349, 2000.

[33] LEHTOVAARA, L.; TOIVANEN, J.; ELORANTA, J. Solution of time-independent schrödinger equation by the imaginary time propagation method. *Journal of Computational Physics*, v. 221, p. 148–157, 2007.

[34] LIU, X.; SU, L.; DING, P. Symplectic algorithm for use in computing the time-independent schrödinger equation. *International Journal of Quantum Chemistry*, v. 87, p. 1–11, 2002.

[35] HARTREE, D. R. The wave mechanics of an atom with a non-coulomb central field. part ii. some results and discussion. *In Mathematical Proceedings of the Cambridge Philosophical Society*, v. 24, p. 111–132, 1928.

[36] HARTREE, D. R. The wave mechanics of an atom with a non-coulomb central field. part iii. term values and intensities in series in optical spectra. *In Mathematical Proceedings of the Cambridge Philosophical Society*, v. 24, p. 426–437, 1928.

[37] HARTREE, D. R. The wave mechanics of an atom with a non-coulomb central field. part i. theory and methods. *In Mathematical Proceedings of the Cambridge Philosophical Society*, v. 24, p. 89–110, 1928.

[38] SLATER, J. C. The self consistent field and the structure of atoms. *Physical Review*, v. 32, p. 339, 1928.

[39] LYKOS, P.; PRATT, G. W. Discussion on the hartree-fock approximation. *Reviews of Modern Physics*, v. 35, p. 496, 1963.

[40] SLATER, J. C. A simplification of the hartree-fock method. *Physical Review*, v. 81, p. 385, 1951.

[41] BAERENDS, E. J.; ELLIS, D. E.; ROS, P. J. C. P. Self-consistent molecular hartree—fock—slater calculations i. the computational procedure. *Chemical Physics*, v. 2, p. 41–51, 1973.

[42] FISCHER, C. F. General hartree-fock program. *Computer physics communications*, v. 43, p. 355–365, 1987.

[43] LIEB, E. H.; SIMON, B. The hartree-fock theory for coulomb systems. *Communications in Mathematical Physics*, v. 53, p. 185–194, 1977.

[44] SHAVITT, I. The method of configuration interaction. In: *In Methods of electronic structure theory*. Boston, MA: Springer, 1977. p. 189–275.

[45] LANGHOFF, S. R.; DAVIDSON, E. R. Configuration interaction calculations on the nitrogen molecule. *International Journal of Quantum Chemistry*, v. 8, p. 61–72, 1974.

[46] FANO, U. Effects of configuration interaction on intensities and phase shifts. *Physical Review*, v. 124, p. 1866, 1961.

[47] SCHLEGEL, H. Møller-plesset perturbation theory with spin projection. *The Journal of Physical Chemistry*, v. 92, p. 3075–3078, 1988.

[48] CHRISTIANSEN, O. Møller–plesset perturbation theory for vibrational wave functions. *The Journal of Physical Chemistry*, v. 119, p. 5773–5781, 2003.

[49] PULAY, P.; SAEBø, S. Orbital-invariant formulation and second-order gradient evaluation in møller-plesset perturbation theory. *Theoretica chimica acta*, v. 69, p. 357–368, 1986.

[50] DEWAR, M. et al. Development and use of quantum mechanical molecular models. 76. am1: a new general purpose quantum mechanical molecular model. *Journal of the American Chemical Society*, v. 107, p. 3902–3909, 1985.

[51] JAKALIAN, A.; JACK, D. B.; BAYLY, C. I. Fast, efficient generation of high-quality atomic charges. am1-bcc model: Ii. parameterization and validation. *Journal of computational chemistry*, v. 23, p. 1623–1641, 2002.

[52] GALVAO, D. S. et al. A parametric method 3 (pm3) study of trans-stilbene. *The Journal of chemical physics*, v. 98, p. 3016–3021, 1993.

[53] KOLASKAR, A. S.; TONGAONKAR, P. C. A semi-empirical method for prediction of antigenic determinants on protein antigens. *FEBS letters*, v. 276, p. 172–174, 1990.

[54] MANCUSO, J.; MCEACHERN, R. J. Applications of the pm3 semi-empirical method to the study of triethylenediamine. *Journal of Molecular Graphics and Modelling*, v. 15, p. 82–90, 1997.

[55] VAUTHERIN, D.; BRINK, D. T. Hartree-fock calculations with skyrme's interaction. i. spherical nuclei. *Physical Review C*, v. 5, p. 626, 1972.

[56] VENER, M. V. et al. Intermolecular hydrogen bond energies in crystals evaluated using electron density properties: Dft computations with periodic boundary conditions. *Journal of Computational Chemistry*, v. 33, p. 2303–2309, 2012.

[57] SCHWINGER, J. Thomas-fermi model: The second correction. In: *A Quantum Legacy: Seminal Papers of Julian Schwinger*. [S.l.: s.n.], 1981. p. 770–778.

[58] MYERS, W. D.; SWIATECKI, W. J. Nuclear properties according to the thomas-fermi model. *Nuclear Physics A*, v. 601, p. 141–167, 1996.

[59] SCHWINGER, J. Thomas-fermi model: The leading correction. *Physical Review A*, v. 22, p. 1827, 1980.

[60] LATTER, R. Atomic energy levels for the thomas-fermi and thomas-fermi-dirac potential. *Physical Review*, v. 99, p. 510, 1955.

[61] TELLER, E. On the stability of molecules in the thomas-fermi theory. *Reviews of Modern Physics*, v. 34, p. 627, 1962.

[62] CHAN, G. K.-L.; COHEN, A. J.; HANDY, N. C. Thomas–fermi–dirac–von weizsäcker models in finite systems. *The Journal of Chemical Physics*, v. 114, p. 631–638, 2001.

[63] BANERJEE, B.; CONSTANTINESCU, D. H.; REHAK, P. Thomas-fermi and thomas-fermi-dirac calculations for atoms in a very strong magnetic field. *Physical Review D*, v. 10, p. 2384, 1974.

[64] GILBERT, T. L. Hohenberg-kohn theorem for nonlocal external potentials. *Physical Review B*, v. 12, p. 2111, 1975.

[65] GöRLING, A. Density-functional theory beyond the hohenberg-kohn theorem. *Physical Review A*, v. 59, p. 3359, 1999.

[66] EPSTEIN, S. T.; ROSENTHAL, C. M. The hohenberg–kohn theorem. *The Journal of Chemical Physics*, v. 64, p. 247–249, 1976.

[67] ENGLISCH, H.; ENGLISCH, R. Hohenberg-kohn theorem and non-v-representable densities. *Physica A: Statistical Mechanics and its Applications*, v. 121, p. 253–268, 1983.

[68] YABANA, K.; BERTSCH, G. F. Time-dependent local-density approximation in real time. *Physical Review B*, v. 54, p. 4484, 1996.

[69] NEGELE, J. W. Structure of finite nuclei in the local-density approximation. *Physical review C*, v. 1, p. 1260, 1970.

[70] LANGRETH, D. C.; MEHL, M. J. Beyond the local-density approximation in calculations of ground-state electronic properties. *Physical review B*, v. 28, p. 1809, 1983.

[71] STAMPFL, C.; WALLE, C. G. V. de. Density-functional calculations for iii-v nitrides using the local-density approximation and the generalized gradient approximation. *Physical review B*, v. 59, p. 5521, 1999.

[72] PERDEW, J. P.; BURKE, K.; ERNZERHOF, M. Generalized gradient approximation made simple. *Physical Review Letters*, v. 77, p. 3865, 1996.

[73] WU, Z.; COHEN, R. E. More accurate generalized gradient approximation for solids. *Physical Review B*, v. 73, p. 235116, 2006.

[74] KOHN WALTER, A. D. B.; 100, n. . . .-. Robert G. Parr. "Density functional theory of electronic structure." The Journal of P. C. Assessment of dispersion corrections in dft calculations on large biological systems. *Molecular Physics*, v. 110, p. 3061–3076, 2012.

[75] VON, L. et al. Optimization of effective atom centered potentials for london dispersion forces in density functional theory. *Physical Review Letters*, v. 93, p. 153004, 2004.

[76] PERDEW, J.; BURKE, K.; ERNZERHOF, M. Generalized gradient approximation made simple. *Phys. Rev. Lett.*, v. 77, p. 3865, 1996.

[77] WANG, Z. et al. Diffusion of alkali metals in the first stage graphite intercalation compounds by vdw-dft calculations. *RSC Advances*, v. 5, p. 15985–15992, 2015.

[78] COMETTO, F. P. et al. Electrochemical, high-resolution photoemission spectroscopy and vdw-dft study of the thermal stability of benzenethiol and benzeneselenol monolayers on au (111). *Langmuir*, v. 28, p. 13624–13635, 2012.

[79] PRAYOGO, G. I. et al. Importance of van der waals interactions in hydrogen adsorption on a silicon-carbide nanotube revisited with vdw-dft and quantum monte carlo. *ACS Omega*, v. 6, p. 24630–24636, 2021.

[80] WEI, X. et al. A dft study of the adsorption of o_2 and h_2o on al (111) surfaces. *RSC Advances*, v. 6, p. 56303–56312, 2016.

[81] LIAO, M.-S.; HUANG, M.-J.; WATTS, J. D. Assessment of dispersion corrections in dft calculations on large biological systems. *Molecular Physics*, v. 110, p. 3061–3076, 2012.

[82] LANGRETH, D. C. et al. Van der waals density functional theory with applications. *International Journal of Quantum Chemistry*, v. 101, p. 599–610, 2005.

[83] GEIM, A. K. Graphene: status and prospects. *Science*, v. 324, p. 1530–1534, 2009.

[84] SEABRA, A. B. et al. Nanotoxicity of graphene and graphene oxide. *Chemical research in toxicology*, v. 27, p. 159–168, 2014.

[85] GRIGORENKO, A. N.; POLINI, M.; NOVOSELOV, K. S. Graphene plasmonics. *Nature photonics*, v. 6, p. 749–758, 2012.

[86] VOGT, P. et al. Silicene: compelling experimental evidence for graphenelike two-dimensional silicon. *Physical Review Letters*, v. 108, p. 155501, 2012.

[87] D´AVILA, M. et al. Germanene: a novel two-dimensional germanium allotrope akin to graphene and silicene. *New Journal of Physics*, v. 16, p. 095002, 2014.

[88] ZHU, F. et al. Epitaxial growth of two-dimensional stanene. *Nature Materials*, v. 14, p. 1020–1025, 2015.

[89] LI, L. et al. Black phosphorus field-effect transistors. *Nature Nanotechnology*, v. 9, p. 372–377, 2014.

[90] JI, J. et al. Two-dimensional antimonene single crystals grown by van der waals epitaxy. *Nature Communication*, v. 7, p. 13352, 2016.

[91] CONG, e. a. W. Boron quantum dots all-optical modulator based on efficient photothermal effect. *Opto-Electronic Advances*, v. 4, p. 200032, 2021.

[92] YUNXIA, e. a. L. Stable and metallic borophene nanoribbons from first-principles calculations. *Journal of Materials Chemistry C*, v. 4, p. 6380–6385, 2016.

[93] IHSAN, B. New quasi-planar surfaces of bare boron. *Surface Science*, v. 370, p. 355–363, 1997.

[94] IHSAN, B. New convex and spherical structures of bare boron clusters. *Journal of Solid State Chemistry*, v. 133, p. 182–189, 1997.

[95] BOUSTANI, I.; QUANDT, A. Nanotubules of bare boron clusters: Ab initio and density functional study. *Europhysics Letters*, v. 39, p. 527–532, 1997.

[96] AL, A. J. M. et. Borophene as a prototype for synthetic 2d materials development. *Nat. Nanotechnol.*, v. 13, p. 444–450, 2018.

[97] AL, A. J. M. et. Synthesis of borophenes: Anisotropic, two-dimensional boron polymorphs. *Science*, v. 350, p. 1513, 2015.

[98] AL, Y. L. et. Probing the synthesis of two-dimensional boron by first-principles computations. *Angew. Chem. Int. Ed.*, v. 52, p. 3156–3159, 2013.

[99] AL, H. L. et. From boron cluster to two-dimensional boron sheet on cu(111) surface: Growth mechanism and hole formation. *Sci. Rep.*, v. 3, p. 3238, 2013.

[100] AL, W. L. et. Experimental realization of honeycomb borophene. *Sci. Bull.*, v. 63, p. 282–286, 2018.

[101] HAN, M. Y. et al. Energy band-gap engineering of graphene nanoribbons. *Physical Review Letters*, v. 98, p. 206805, 2007.

[102] RANI, P.; JINDAL, V. K. Designing band gap of graphene by b and n dopant atoms. *RSC Advances*, v. 3, p. 802–812, 2013.

[103] ZHANG, Y. et al. Direct observation of a widely tunable bandgap in bilayer graphene. *Nature*, v. 459, p. 820–823, 2009.

[104] ZHANG, X. et al. A facile and universal top-down method for preparation of monodisperse transition-metal dichalcogenide nanodots. *Angewandte Chemie International Edition*, v. 54, p. 5425–5428, 2015.

[105] YIM, C. et al. Electrical devices from top-down structured platinum diselenide films. *Npj 2D Materials and Applications*, v. 2, p. 1–7, 2018.

[106] BROWN, K. A. et al. Top-down proteomics of endogenous membrane proteins enabled by cloud point enrichment and multidimensional liquid chromatography–mass spectrometry. *Analytical Chemistry*, v. 92, p. 15726–15735, 2020.

[107] COOGAN Áine; GUN'KO, Y. K. Solution-based "bottom-up" synthesis of group vi transition metal dichalcogenides and their applications. *Materials Advances*, v. 2, p. 146–164, 2021.

[108] CHIU, M. et al. Metal-guided selective growth of 2d materials: demonstration of a bottom-up cmos inverter. *Advanced Materials*, v. 31, p. 1900861, 2019.

[109] WANG, S. et al. Bottom-up synthesis of ws$_2$ nanosheets with synchronous surface modification for imaging guided tumor regression. *Acta Biomaterialia*, v. 58, p. 442–454, 2017.

[110] LIN, Z. et al. Thermal expansion coefficient of few-layer mos2 studied by temperature-dependent raman spectroscopy. *Scientific Reports*, v. 11, p. 1–9, 2021.

[111] PU, J. et al. Highly flexible mos$_2$ thin-film transistors with ion gel dielectrics. *Nano Letters*, v. 8, p. 4013–4017, 2012.

[112] ZHANG, Y. et al. Ambipolar mos$_2$ thin flake transistors. *Nano Letters*, v. 12, p. 1136–1140, 2012.

[113] YIN, Z. et al. Single-layer mos$_2$ phototransistors. *ACS Nano*, v. 6, p. 74–80, 2012.

[114] ORIOL et al. Ultrasensitive photodetectors based on monolayer mos$_2$. *Nature Nanotechnology*, v. 8, p. 497–501, 2013.

[115] ZENG, H. et al. Valley polarization in mos$_2$ monolayers by optical pumping. *Nature Nanotechnology*, v. 7, p. 490–493, 2012.

[116] LEE, C.-H. et al. Atomically thin $p-n$ junctions with van der waals heterointerfaces. *Nature Nanotechnology*, v. 9, p. 676–681, 2014.

[117] BAUGHER, B. W. et al. Electrically tunable pn diodes in a monolayer dichalcogenide. *Nature Nanotechnology*, v. 9, p. 262–267, 2014.

[118] BURKOV, A. Topological semimetals. *Nature Materials*, v. 15, p. 1145–1148, 2016.

[119] BURKOV, A.; HOOK, M. D.; BALENTS, L. Topological nodal semimetals. *Physical Review B*, v. 84, p. 2235126, 2011.

[120] LIU, Z. K. et al. Discovery of a three-dimensional topological dirac semimetal, na$_3$bi. *Science*, v. 84, p. 864–867, 2014.

[121] XU, S.-Y. et al. Discovery of a weyl fermion semimetal and topological fermi arcs. *Science*, v. 349, p. 613–617, 2015.

[122] HU, J. et al. Evidence of topological nodal-line fermions in zrsise and zrsite. *Physical Review Letters*, v. 117, p. 016602, 2016.

[123] BZDUSEK, T. et al. Nodal-chain metals. *Nature*, v. 518, p. 75–78, 2016.

[124] FENG, X. et al. Discovery of a weyl fermion semimetal and topological fermi arcs. *Physical Review Materials*, v. 2, p. 014202, 2018.

[125] MOOK, A.; HENK, J.; MERTIG, I. Magnon nodal-line semimetals and drumhead surface states in anisotropic pyrochlore ferromagnets. *Physical Review B*, v. 95, p. 014418, 2017.

[126] KOPNIN, N. B.; HEIKKILä, T. T.; VOLOVIK, G. E. High-temperature surface superconductivity in topological flat-band systems. *Physical Review B*, v. 83, p. 220503(R), 2011.

[127] RHIM, J.-W.; KIM, Y. B. Landau level quantization and almost flat modes in three-dimensional semimetals with nodal ring spectra. *Physical Review B*, v. 92, p. 045126, 2015.

[128] HUH, Y.; MOON, E.-G.; KIM, Y. B. Long-range coulomb interaction in nodal-ring semimetals. *Physical Review B*, v. 93, p. 035138, 2016.

[129] NEUMANN, J. von; WIGNER, E. P. Über das Verhalten von Eigenwerten bei adiabatischen Prozessen. *Phys. Zeit.*, v. 30, p. 467–470, 1920.

[130] SACHDEV, S. (Ed.). *Quantum phase transitions*. Cambridge: Cambridge University Press, 2001.

[131] MURAKAMI, S. Phase transition between the quantum spin Hall and insulator phases in 3D: Emergence of a topological gapless phase. *New J. Phys.*, v. 9, p. 356, 2007.

[132] BURKOV, A. A. Topological semimetals. *Nat. Mater.*, v. 15, p. 1145–1148, 2016.

[133] MICHEL, L.; ZAK, J. Connectivity of energy bands in crystals. *Phys. Rev. B*, v. 59, p. 5998, 1999.

[134] ZHAO, Y.; SCHNYDER, A. P.; WANG, Z. Unified theory of PT and CP invariant topological metals and nodal superconductors. *Phys. Rev. Lett.*, v. 116, p. 156402, 2016.

[135] SCHNYDER, A. P. 2018. Accidental and symmetry-enforced band crossings in topological semimetals, Topological Matter School 2018.

[136] YOUNG, S. M.; KANE, C. L. Dirac semimetals in two dimensions. *Phys. Rev. Lett.*, v. 115, p. 126803, 2015.

[137] WAN, R. et al. Topological semimetal and Fermi-arc surface states in the electronic structure of pyrochlore iridates. *Phys. Rev. B*, v. 83, p. 205101, 2011.

[138] BURKOV, A. A.; KIM, Y. B. $\mathbb{Z}_2$ and chiral anomaliesin topological Dirac semimetals. *Phys. Rev. Lett*, v. 86, p. 115113, 2016.

[139] ZUTIĆ, I. et al. Proximitized materials. *Mater. Today*, v. 22, p. 85–107, 2019.

[140] XIA, F. et al. Black phosphorus and its isoelectronic materials. *Nat. Rev. Phys.*, v. 1, p. 306–317, 2019.

[141] LU, J.-L. et al. Two-dimensional node-line semimetals in a honeycomb-Kagome lattice. *Chin. Phys. Lett.*, v. 34, p. 057302, 2017.

[142] GAO, B. et al. Density functional theory calculation on two-dimensional MoS_2/BiOX (X= Cl, Br, I) van der waals heterostructures for photocatalytic action. *Appl. Surf. Sci.*, v. 492, p. 157–165., 2019.

[143] ZHANG, J. et al. Topological band crossings in hexagonal materials. *Phys. Rev. Mater.*, v. 2, p. 074201, 2018.

[144] PARK, H. et al. Visible light-induced stable HER performance using duality of ultrafine Pt NPs in a *Z*-scheme *pn* junction Fe_2O_3@Pt@FeS catalyst. *Appl. Surf. Sci.*, v. 541, p. 148347, 2021.

[145] WIEDER, B. J. et al. Topological materials discovery from crystal symmetry. *Nat. Rev. Mater.*, v. 7, p. 196–216, 2022.

[146] LIU, F. et al. Robust topological nodal-line semimetals from periodic vacancies in two-dimensional materials. *J. Phys. Chem. Lett.*, v. 12, p. 5710, 2021.

[147] GIANNOZZI, P. et al. Quantum espresso: A modular and open-source software project for quantum simulations of materials. *J. Phys. Cond. Matt.*, v. 21, p. 395502, 2009.

[148] MOSTOFI, A. A. et al. An updated version of Wannier90: A tool for obtaining Maximally-Localised Wannier Functions. *Comp. Phys. Comm.*, v. 185, p. 2309–2310, 2014.

[149] FENG, B. et al. Experimental realization of two-dimensional boron sheets. *Nature Chemistry*, v. 8, p. 563–568, 2016.

[150] WANG, Z. et al. Higher-order topology, monopole nodal lines, and the origin of large fermi arcs in transition metal dichalcogenides xte_2 (x=mo, w). *Phys. Rev. Lett.*, v. 123, n. 10, p. 186401, 2019.

[151] TANG, H.; ISMAIL-BEIGI, S. Novel precursors for boron nanotubes: The competition of two-center and three-center bonding in boron sheets. *Phys. Rev. Lett.*, v. 99, n. 5, p. 115501, 2007.

[152] WANG, Y. et al. Borophene with large holes. *J. Phys. Chem. Lett.*, v. 11, n. 15, p. 6235–6241, 2020.

[153] MANNIX, A. J. et al. Synthesis of borophenes: Anisotropic, two-dimensional boron polymorphs. *Science*, v. 350, n. 6267, p. 1513–1516, 2015.

[154] FENG, B. et al. Experimental realization of two-dimensional boron sheets. *Nat. Chem.*, v. 8, n. 3, p. 563–568, 2016.

[155] RANJAN, P. et al. Freestanding borophene and its hybrids. *Adv. Mat.*, v. 31, n. 27, p. 1900353, 2019.

[156] TSAI, H.-S. et al. Fabrication of multilayer borophene on insulator structure. *Small*, v. 12, n. 38, p. 5251–5255, 2016.

[157] KOU, L. et al. Effect of confinement on the exciton and biexciton dynamics in perovskite 2d-nanosheets and 3d-nanocrystals. *J. Phys. Chem. Lett.*, v. 11, n. 15, p. 6344–6352, 2020.

[158] PENEV, E. S. et al. Polymorphism of two-dimensional boron. *Nano Lett.*, v. 12, n. 5, p. 2441–2445, 2012.

[159] ZHAO, Y. X.; SCHNYDER, A. P. Nonsymmorphic symmetry-required band crossings in topological semimetals. *Phys. Rev. B*, v. 94, n. 11, p. 195109, 2016.

[160] CHIU, C.-K.; SCHNYDER, A. P. Classification of reflection-symmetry-protected topological semimetals and nodal superconductors. *Phys. Rev. B*, v. 90, n. 11, p. 205136, 2014.

[161] ZUTIĆ, I. et al. Proximitized materials. *Mater. Today*, v. 22, n. 2, p. 85–107, 2019.

[162] FORNIERI, A. et al. Evidence of topological superconductivity in planar josephson junctions. *Nature*, v. 569, n. 4, p. 89–92, 2019.

[163] REN, H. et al. Topological superconductivity in a phase-controlled josephson junction. *Nature*, v. 569, n. 4, p. 93–98, 2019.

[164] DARTIAILH, M. C. et al. Phase signature of topological transition in josephson junctions. *Phys. Rev. Lett.*, v. 126, n. 1, p. 036802, 2021.

[165] AGUADO, R.; KOUWENHOVEN, L. P. Majorana qubits for topological quantum computing. *Phys. Today*, v. 73, n. 6, p. 44–50, 2020.

[166] YU, Z.-M. et al. Quadratic and cubic nodal lines stabilized by crystalline symmetry. *Phys. Rev. B*, v. 99, n. 3, p. 121106(R), 2019.

[167] YANG, B.-J. et al. Topological semimetals protected by off-centered symmetries in nonsymmorphic crystals. *Phys. Rev. B*, v. 95, p. 075135, 2017.

[168] MALARD, M. et al. Movable but not removable band degeneracies in a symmorphic crystal. *Phys. Rev. B*, v. 98, p. 165127, 2018.

[169] FRENKEL, J. On the transfer of light into heat in solids i. *Phys. Rev.*, v. 37, p. 17–44, 1931.

[170] JIANG, Z. et al. Scaling universality between band gap and exciton binding energy of two-dimensional semiconductors. *Phys. Rev. Lett.*, v. 118, p. 266401, 2017.

[171] LIU, Z.-R.; WU, J.; DUAN, W. Electronic-structure theory of crystalline insulators under a homogeneous electric field. *Phys. Rev. B*, v. 69, p. 085117, 2004.

[172] OLSEN, T. et al. Simple screened hydrogen model of excitons in two-dimensional materials. *Phys. Rev. Lett.*, v. 116, p. 056401, 2016.

[173] LATINI, S.; OLSEN, T.; THYGESEN, K. Excitons in van der wals heterostructures: The important role of dielectric screening. *Phys. Rev. B*, v. 92, p. 1–13, 2015.

[174] RASMUSSEN, F.; THYGESEN, K. Computational 2d materials database: Electronic structure of transition-metal dichalcogenides and oxides. *J. Phys. Chem. C*, v. 23, p. 13169–13183, 2015.

[175] PASQUAL, R. et al. Valley-polarized exciton dynamics in a 2d semiconductor heterostructure. *Science*, v. 351, p. 688–691, 2016.

[176] CUTKOSKY, R. Solutions of a bethe-salpeter equation. *Physical Review*, v. 96, p. 1135, 1954.

[177] MARINI, A. et al. Yambo: an *ab initio* tool for excited state calculations. *Computer Physics Communications*, v. 180, p. 1392–1403, 2009.

[178] WU, F.; QU, F.; MACDONALD, A. H. Exciton band structure of monolayer mos_2. *Phys. Rev. B*, v. 91, p. 075310, 2015.

[179] MERZBACHER, E. *Many-particle physics, 3rd ed.* Springer: [s.n.], 2010. 27 p.

[180] PALUMMO, M.; BERNARDI, M.; GROSSMAN, J. C. Exciton radiative lifetimes in two-dimensional transition metal dichalcogenides. *Nano Lett.*, v. 15, p. 2794–2800, 2015.

[181] RADISAVLJEVIC, B. et al. Single-layer mos_2 transistors. *Nat. Nanotech.*, v. 6, p. 147–150, 2011.

[182] HE, J.; HUMMER, K.; FRANCHINI, C. Stacking effects on the electronic and optical properties of bilayer transition metal dichalcogenides mos_2, $mose_2$, ws_2, and wse_2. *Phys. Rev. B*, v. 89, p. 075409, 2014.

[183] FEIERABEND, M. et al. Proposal for dark exciton based chemical sensors. *Nat. Comm.*, v. 8, p. 1–6, 2017.

[184] BONILLA, M. et al. Strong room-temperature ferromagnetism in vse_2 monolayers on van der waals substrates. *Nature Nanotechnology*, v. 13, p. 289–293, 2018.

[185] LIN, Z.; ZHIGILEI, L. V.; CELLI, V. Electron-phonon coupling and electron heat capacity of metals under conditions of strong electron-phonon nonequilibrium. *Phys. Rev. B*, v. 77, p. 075133, 2008.

[186] ZHOU, H. et al. A flexible in-plane p–n heterojunction nano-generator with phonon-enhanced photothermoelectric effect to harvest solar energy. *J. Mater. Chem. A*, v. 9, p. 14958–14968, 2021.

[187] FROHLICH, H. On the theory of dielectric breakdown in solids. *Proc. H. Soc. A*, v. 188, p. 521–532, 1947.

[188] CALLEN, H. Electric breakdown in ionic crystals. *Phys. Rev.*, v. 76, p. 1394, 1949.

[189] EHRENREICH, H. Electron scattering in insb. *J. Phys. Chem. Solids*, v. 2, p. 131–149, 1957.

[190] MERZBACHER, E. *Quantum mechanics, 3rd ed.* Wiley: [s.n.], 1998. 98 p.

[191] CHEN, H. Y.; SANGALLI, D.; BERNARDI, M. Exciton-phonon interaction and relaxation times from first principles. *Phys. Rev. Let.*, v. 125, p. 107401, 2020.

[192] LIU, F.; MIN, P.; LI, J. *ab* initio calculation of ideal strength and phonon instability of graphene under tension. *Phys. Rev. B*, v. 76, p. 064120, 2007.

[193] FERRY, D. K. *Semiconductor ransport.* Taylor and Francis, New York: [s.n.], 2000. 33 p.

[194] JIN, Z. et al. Intrinsic transport properties of electrons and holes in monolayer transition-metal dichalcogenides. *Phys. Rev. B*, v. 90, p. 045422, 2014.

[195] SILVA, M. Z. de A. E.; SHAM, E. A. Exciton spin dynamics in quantum wells. *Phys. Rev. B*, v. 47, p. 15776, 1993.

[196] VINATTIERI, A. Exciton dynamics in gaas quantum wells under resonant excitation. *Phys. Rev. B*, v. 50, p. 10868, 1994.

[197] ZHU, H. et al. Observation of chiral phonons. *Science*, v. 359, p. 579, 2018.

[198] LO, P. et al. Full-zone valley polarization landscape of finite-momentum exciton in transition metal dichalcogenide monolayers. *Phys. Rev. Res.*, v. 3, p. 043198, 2021.

[199] YU, H. et al. Inverted valley polarization in optically excited transition metal dichalcogenides. *Nat. Commun.*, v. 5, p. 3876, 2014.

[200] WU, M.; JIANG, J.; WENG, M. Spin dynamics in semiconductors. *Phys. Rep.*, v. 493, p. 61, 2010.

[201] LAGARDE, D. et al. Carrier and polarization dynamics in monolayer mos$_2$. *Phys. Rev. Lett.*, v. 112, p. 047401, 2014.

APPENDIXES

I. GLIDE-PLANE SYMMETRY

Let $|k_x, k_y\rangle_\alpha$ ($\alpha = 1, 2, 3, 4$) be the eigenstate of the Bloch Hamiltonian $\mathcal{H}(k_x, k_y)$ with eigenenergy $E_\alpha(k_x, k_y)$, i.e.

$$\mathcal{H}(k_x, k_y)|k_x, k_y\rangle_\alpha = E_\alpha(k_x, k_y)|k_x, k_y\rangle_\alpha. \tag{A-1.1}$$

Combining Eq. 3.24 and Eq. A-1.1, we get:

$$\mathcal{H}(k_x, k_y)\ \mathcal{G}(k_x, k_y)|k_x, -k_y\rangle_{\alpha'} = E_{\alpha'}(k_x, -k_y)\ \mathcal{G}(k_x, k_y)|k_x, -k_y\rangle_{\alpha'}, \tag{A-1.2}$$

which means that $\mathcal{G}(k_x, k_y)|k_x, -k_y\rangle_{\alpha'}$ is an eigenstate of $\mathcal{H}(k_x, k_y)$ with eigenenergy $E_{\alpha'}(k_x, -k_y)$. It follows that $\mathcal{G}(k_x, k_y)|k_x, -k_y\rangle_{\alpha'}$ equals an eigenstate $|k_x, k_y\rangle_\alpha$ up to a phase, i.e.,

$$\mathcal{G}(k_x, k_y)|k_x, -k_y\rangle_{\alpha'} = e^{i\theta_{\alpha',\alpha}(k_x,k_y)}|k_x, k_y\rangle_\alpha. \tag{A-1.3}$$

It also follows that $E_{\alpha'}(k_x, -k_y) = E_\alpha(k_x, k_y)$.

On the lines $k_y = \bar{k}_y = 0, \pm\pi$, $\mathcal{H}(k_x, -\bar{k}_y) = \mathcal{H}(k_x, \bar{k}_y)$ (where $\mathcal{H}(k_x, \mp\pi) = \mathcal{H}(k_x, \pm\pi)$ follows from the 2π-periodicity of the BZ). On these lines, Eq. (1) yields $[\mathcal{G}(k_x, \bar{k}_y), \mathcal{H}(k_x, \bar{k}_y)] = 0$, and hence $\mathcal{G}(k_x, \bar{k}_y)$ and $\mathcal{H}(k_x, \bar{k}_y)$ share a set of eigenstates. Indeed, substituting k_y by $\bar{k}_y$ in Eq. (A-1.2) (and using that $\mathcal{H}(k_x, \bar{k}_y) = \mathcal{H}(k_x, -\bar{k}_y)$), we conclude that $\mathcal{G}(k_x, \bar{k}_y)|k_x, \bar{k}_y\rangle_{\alpha'}$ is an eigenstate of $\mathcal{H}(k_x, \bar{k}_y)$ with eigenenergy $E_{\alpha'}(k_x, \bar{k}_y)$. Since the eigenenergies are, in general, non-degenerate (i.e., $E_\alpha(k_x, k_y) \neq E_{\alpha'}(k_x, k_y)$ for $\alpha \neq \alpha'$), it follows that $\mathcal{G}(k_x, \bar{k}_y)|k_x, \bar{k}_y\rangle_{\alpha'}$ equals $|k_x, \bar{k}_y\rangle_{\alpha'}$ up to a phase, i.e.,

$$\mathcal{G}(k_x, \bar{k}_y)|k_x, \bar{k}_y\rangle_{\alpha'} = e^{i\theta_{\alpha'}(k_x)}|k_x, \bar{k}_y\rangle_{\alpha'}. \tag{A-1.4}$$

The matrix $\mathcal{G}(k_x, k_y)$ can be obtained by extracting how the glide plane G transforms the second-quantized operator $c^j_{m_x, m_y}$ acting on the j-th site of the unit cell located at (m_x, m_y). Using Figure 2(a), it is easy to see that G acts on the operator of the unit cell at $(-1, -1)$ as

$$G\, c^1_{-1,-1} = c^2_{-1,0} \qquad\qquad G\, c^2_{-1,-1} = c^1_{0,0}$$
$$G\, c^3_{-1,-1} = c^4_{-1,1} \qquad\qquad G\, c^4_{-1,-1} = c^3_{0,1}$$

For an unit cell at $(-m_x, -m_y)$, G act as

$$G\, c^1_{-m_x,-m_y} = c^2_{-m_x,m_y-1} \qquad G\, c^2_{-m_x,-m_y} = c^1_{-m_x+1,m_y-1}$$
$$G\, c^3_{-m_x,-m_y} = c^4_{-m_x,m_y} \qquad\quad G\, c^4_{-m_x,-m_y} = c^3_{-m_x+1,m_y}.$$

Applying the Fourier transform of $c^j_{m_x, m_y}$, i.e.

$$c^j_{m_x, m_y} = \sum_{k_x, k_y} c^j_{k_x, k_y} e^{i(k_x m_x + k_y m_y)}, \tag{A-1.5}$$

we obtain these relations in momentum space as

$$G\, c^1_{k_x,k_y} = e^{ik_y} c^2_{k_x,-k_y} \qquad\qquad G\, c^2_{k_x,k_y} = e^{i(k_x+k_y)} c^1_{k_x,-k_y}$$
$$G\, c^3_{k_x,k_y} = c^4_{k_x,-k_y} \qquad\qquad\qquad G\, c^4_{k_x,k_y} = e^{ik_x} c^3_{k_x,-k_y}.$$

The above transformations can be carried out by applying the operator $\mathcal{G}(k_x, k_y) \Updownarrow_{k_y}$ to the spinor $c_{k_x,k_y} = [c^1_{k_x,k_y} \quad c^2_{k_x,k_y} \quad c^3_{k_x,k_y} \quad c^4_{k_x,k_y}]^T$, where $\Updownarrow_{k_y}$ flips k_y and $\mathcal{G}(k_x, k_y)$ is the 4×4 matrix

$$\mathcal{G}(k_x, k_y) = \begin{bmatrix} e^{ik_y} g(k_x) & 0 \\ 0 & g(k_x) \end{bmatrix}, \qquad g(k_x) = \begin{bmatrix} 0 & 1 \\ e^{ik_x} & 0 \end{bmatrix}. \tag{A-1.6}$$

The eigenvalues of $\mathcal{G}(k_x, \bar{k}_y)$ are found by solving the characteristic equation

$$\begin{aligned} \det[\mathcal{G}(k_x, \bar{k}_y) - \xi \mathbb{1}] &= \det \begin{bmatrix} \pm g(k_x) - \xi \mathbb{1} & 0 \\ 0 & g(k_x) - \xi \mathbb{1} \end{bmatrix} \\ &= \det[\pm g(k_x) - \xi \mathbb{1}] \det[g(k_x) - \xi \mathbb{1}] \\ &= (\xi^2 - e^{ik_x})^2 = 0. \end{aligned} \tag{A-1.7}$$

The two-fold degenerate eigenvalues of $\mathcal{G}(k_x, \bar{k}_y)$ are thus

$$\xi_{1,3} = e^{ik_x/2}, \ \xi_{2,4} = -e^{ik_x/2}. \tag{A-1.8}$$

By enforcing Eq. 3.24, with $\mathcal{G}(k_x, k_y)$ given by Eq.(A-1.6), the entries $\varepsilon_{n,m}(k_x, k_y)$ of $\mathcal{H}(k_x, k_y)$ get constrained by the relations:

$$\varepsilon_{n+1,n+1} = \varepsilon_{n,n}, \ n = 1, 3; \tag{A-1.9}$$

$$\varepsilon^*_{n,n+1}(k_x, k_y) = e^{ik_x} \varepsilon_{n,n+1}(k_x, -k_y), \ n = 1, 3; \tag{A-1.10}$$

$$\varepsilon_{2,3}(k_x, k_y) = e^{i(k_x+k_y)} \varepsilon_{1,4}(k_x, -k_y); \tag{A-1.11}$$

$$\varepsilon_{2,4}(k_x, k_y) = e^{ik_y} \varepsilon_{1,3}(k_x, -k_y). \tag{A-1.12}$$

For the tight-binding model whose entries are given by Eq. (2) (with the specified conditions for the parameters given below Eq. (2)), Eqs. (A-1.9)-(A-1.12) yield

$$\varepsilon_{n+1,n+1} = \varepsilon_{n,n} = 2\mu_n, \ n = 1, 3; \tag{A-1.13}$$

$$\varepsilon_{n,n+1}(k_x, k_y) = 2i\text{Im}(t_{n+1,n}) + t^*_{n+1,n}(1 + e^{-ik_x}), \ n = 1, 3; \tag{A-1.14}$$

$$\varepsilon_{1,3}(k_x, k_y) = t^*_{3,1} + t_{1,3}(1 + e^{ik_y}); \tag{A-1.15}$$

$$\varepsilon_{1,4}(k_x, k_y) = t_{1,4} + t^*_{4,1}(1 + e^{-ik_x}); \tag{A-1.16}$$

$$\varepsilon_{2,3}(k_x, k_y) = e^{i(k_x+k_y)}[t_{1,4} + t^*_{4,1}(1 + e^{-ik_x})]; \tag{A-1.17}$$

$$\varepsilon_{2,4}(k_x, k_y) = e^{ik_y}[t^*_{3,1} + t_{1,3}(1 + e^{-ik_y})]; \tag{A-1.18}$$

and $\varepsilon_{m,n}(k_x, k_y) = \varepsilon^*_{n,m}(k_x, k_y)$.

II.   INVERSION-POINT SYMMETRY

A similar procedure to the one outlined in I for G yields the operator $\mathcal{I}(k_y) \Updownarrow_{k_x,k_y}$ describing the inversion-point transformation I, with

$$\mathcal{I}(k_y) = \begin{bmatrix} e^{ik_y}\sigma_x & 0 \\ 0 & \sigma_x \end{bmatrix}, \qquad \sigma_x = \begin{bmatrix} 0 & 1 \\ 1 & 0 \end{bmatrix}. \tag{A-2.1}$$

The constraints imposed by Eq. 3.26, with $\mathcal{I}(k_y)$ given by Eq.(A-2.1), on the entries $\varepsilon_{n,m}(k_x, k_y)$ of $\mathcal{H}(k_x, k_y)$ are

$$\varepsilon^*_{n,n+1}(k_x, k_y) = \varepsilon_{n,n+1}(-k_x, -k_y), \, n = 1, 3; \tag{A-2.2}$$

$$\varepsilon_{2,3}(k_x, k_y) = e^{ik_y}\,\varepsilon_{1,4}(-k_x, -k_y); \tag{A-2.3}$$

$$\varepsilon_{2,4}(k_x, k_y) = e^{ik_y}\,\varepsilon_{1,3}(-k_x, -k_y). \tag{A-2.4}$$

Applying Eqs. (A-2.2)-(A-2.4) to the tight-binding model with entries given by Eq.3.25 (with the specified conditions for the parameters given below Eq. 3.25) leads to

$$\varepsilon_{n,n+1}(k_x, k_y) = t_{n,n+1} + t_{n+1,n}(1 + e^{-ik_x}), \, n = 1, 3; \tag{A-2.5}$$

$$\varepsilon_{1,3}(k_x, k_y) = t^*_{3,1} + t_{1,3}(1 + e^{ik_y}); \tag{A-2.6}$$

$$\varepsilon_{1,4}(k_x, k_y) = t_{1,4} + t^*_{4,1}(1 + e^{-ik_x}); \tag{A-2.7}$$

$$\varepsilon_{2,3}(k_x, k_y) = e^{ik_y}\,[t_{1,4} + t^*_{4,1}(1 + e^{ik_x})]; \tag{A-2.8}$$

$$\varepsilon_{2,4}(k_x, k_y) = e^{ik_y}\,[t^*_{3,1} + t_{1,3}(1 + e^{-ik_y})], \tag{A-2.9}$$

with $t_{n,n+1}$ and $t_{n+1,n} \in \Re$, $n = 1, 3$, and $\varepsilon_{m,n}(k_x, k_y) = \varepsilon^*_{n,m}(k_x, k_y)$.

Pairwise combining Eqs. (A-1.14)-(A-1.18) and Eqs. (A-2.5)-(A-2.9) yields the off-diagonal entries of the glide-plane and inversion-point invariant tight-binding model:

$$\varepsilon_{n,n+1}(k_x, k_y) = t_{n+1,n}(1 + e^{-ik_x}); \tag{A-2.10}$$

$$\varepsilon_{1,3}(k_x, k_y) = t^*_{3,1} + t_{1,3}(1 + e^{ik_y}); \tag{A-2.11}$$

$$\varepsilon_{1,4}(k_x, k_y) = t^*_{4,1}(1 + e^{-ik_x}); \tag{A-2.12}$$

$$\varepsilon_{2,3}(k_x, k_y) = e^{ik_y}\,[t^*_{4,1}(1 + e^{ik_x})]; \tag{A-2.13}$$

$$\varepsilon_{2,4}(k_x, k_y) = e^{ik_y}\,[t^*_{3,1} + t_{1,3}(1 + e^{-ik_y})], \tag{A-2.14}$$

with $t_{n+1,n} \in \Re$, $n = 1, 3$. The diagonal entries are given by Eq. (A-1.13).

III. BAND-UNFOLDING TECHNIQUE

The band structure of pristine crystals can be obtained by DFT or TB calculation using the crystal unit cell. However, the crystals usually contain disorder, impurities or vacancies. For these materials, lower translation symmetry requires a supercell (SC) instead of unit cell to be adopted in calculations. In our specific problem, the SC approach allows us to study structures in which defects are periodically distributed through the hexagonal lattice. When the Brillouin zone (BZ) becomes small as the SC gets large, the bands crowed in the small BZ. It makes the data analysis difficult. To overcome this difficulty, we developed an unfolding method to improve the visualization, based on the eigenstates calculated for the SC.

Let us firstly determine the BZs of two descriptions in the supercell (SC) and the effective primitive-cell (PC), of the same crystal. Between the crystal momentum k_n at the n-th PC subspace and K at SC, the SC reciprocal lattice vectors G_n can satisfy this equation

$$k_n = K + G_n \tag{A-3.1}$$

following which all the PC subspaces are crowed into the SC BZ.

Now we focus on the eigenstates $\psi_{p,n}(k)$ of the PC and their relationship to eigenstates $\Psi_p(K)$ of SC, with the same energy E_p. The eigensstate $\Psi_p(K_p)$ are constructed based on $\psi_{p,n}(K + G_n)$ as followed

$$\Psi_p(K) = \sum_{n=1}^{N_c} a_{p,n} \psi_{p,n}(K + G_n) \tag{A-3.2}$$

where M_c is the number of PCs per SC, and $a_{p,n}$ are coefficients. As the energy E_p of SC only only coincides with some of those of PC, many of $a_{p,n}$ are zeros. Then the eigenstates of PC and SC are constructed as followed

$$\psi_{p,n}(K + G_n) = \frac{1}{\sqrt{N_s N_c}} \sum_{m=1}^{N_s} \sum_{\alpha,\mu}^{N_o} \sum_{l=1}^{N_c} e^{iK \cdot R_m} b_p^{(\alpha,\mu)}(K + G_n) e^{i(K+G_n) \cdot \rho_l} \times \mid \alpha, \mu; R_m + \rho_l \rangle, \tag{A-3.3}$$

$$\Psi_p(K) = \frac{1}{\sqrt{N_s}} \sum_{m=1}^{N_s} \sum_{\alpha,\mu}^{N_o} \sum_{l=1}^{N_c} e^{iK \cdot R_m} \beta_{l,p}^{(\alpha,\mu)}(K) \mid \alpha, \mu; R_m + \rho_l \rangle, \tag{A-3.4}$$

where N_s and N_o stand for the total number of SCs in the solid and the total number of (orbital, atom) pairs in PC, respectively; $b_p^{\alpha,\mu}(K + G_n)$ and $\beta_{l,p}^{\alpha,\mu}(K_p)$ are coefficients; α denotes the s, p_x, p_y, p_z orbitals and τ represents the atom within one PC; R_m and ρ_l are the positions of the m-th SC and the l-th PC, respectively, with $\mid \alpha, \mu; R_m + \rho_l \rangle$ being the basis function.

Substituting Eqs. A-3.3 and A-3.4 into Eq. A-3.2, we can get

$$e^{-iK_p \cdot \rho_l} \beta_{l,p}^{\alpha,\mu}(K_p) = \frac{1}{\sqrt{N_c}} \sum_n^{N_c} a_{p,n} b_{l,p}^{\alpha,\mu}(K_p + G_n) e^{iK_p \cdot G_n}. \tag{A-3.5}$$

Combining the N_c equations for each band, the above relation can be written in matrix form as

$$B_p \alpha, \mu(K) = \hat{O} A_p^{\alpha,\mu}(K), \tag{A-3.6}$$

where the two vectors are

$$
B_p^{\alpha,\mu}(K) =
\begin{bmatrix}
e^{-iK_p \cdot \rho_1} \beta_{1,p}^{\alpha,\mu}(K_p) \\
\vdots \\
e^{-iK_p \cdot \rho_{N_c}} \beta_{N-c,p}^{\alpha,\mu}(K_p),
\end{bmatrix}
\tag{A-3.7}
$$

$$
A_p^{\alpha,\mu}(K) =
\begin{bmatrix}
a_{p,n(1)} b_p^{(\alpha,\mu)}(K + G_{n(1)}) \\
\vdots \\
a_{p,n(N_c)} b_p^{(\alpha,\mu)}(K + G_{n(N_c)}),
\end{bmatrix}
\tag{A-3.8}
$$

and the unitary matrix $\hat{O}$ is

$$
\hat{O} =
\begin{bmatrix}
e^{i\rho_1 \cdot G_1} & \cdots & e^{i\rho_1 \cdot G_{N_c}} \\
\vdots & \ddots & \vdots \\
e^{i\rho_{N_c} \cdot G_1} & \cdots & e^{i\rho_{N_c} \cdot G_{N_c}}.
\end{bmatrix}
\tag{A-3.9}
$$

Using the normalized Bloch states, we get the probability that the SC state $\Psi_p(K)$ projects onto the PC states $\psi_{p,n}(K + G_n)$, $P_{p,n}$:

$$
P_{p,n} = |\langle \Psi_p(K) \mid \psi_{p,n}(K + G_n) \rangle|^2 = \sum_{\alpha,\mu}^{N_o} \sum_{n}^{N_c} |a_{p,n} b_{l,p}^{\alpha,\mu}(K_p + G_n)|^2.
\tag{A-3.10}
$$

By solving the above equations for each orbital in the PC the complicated band structure of the SC can be unfolded into the effective band structure of the SC.

$$
B_p^{\alpha,\mu}(K) =
\begin{bmatrix}
e^{-iK_p \cdot \rho_1} \beta_{1,p}^{\alpha,\mu}(K_p) \\
\vdots \\
e^{-iK_p \cdot \rho_{N_c}} \beta_{N-c,p}^{\alpha,\mu}(K_p),
\end{bmatrix}
$$